RESPONSE OF NEUTRAL ATMOSPHERE AND IONOSPHERE TO VARIOUS GEOPHYSICAL CONDITIONS

Ph.D. THESIS

by

Gaurav Bharti

DEPARTMENT OF PHYSICS
INDIAN INSTITUTE OF TECHNOLOGY ROORKEE
ROORKEE - 247 667 (INDIA)
NOVEMBER, 2018

RESPONSE OF NEUTRAL ATMOSPHERE AND IONOSPHERE TO VARIOUS GEOPHYSICAL CONDITIONS

A THESIS

Submitted in partial fulfilment of the
requirements for the award of the degree

of

DOCTOR OF PHILOSOPHY

in

PHYSICS

by

Gaurav Bharti

DEPARTMENT OF PHYSICS
INDIAN INSTITUTE OF TECHNOLOGY ROORKEE
ROORKEE - 247 667 (INDIA)
NOVEMBER, 2018

INDIAN INSTITUTE OF TECHNOLOGY ROORKEE ROORKEE

CANDIDATE'S DECLARATION

I hereby certify that the work which is being presented in this thesis entitled, **"RESPONSE OF NEUTRAL ATMOSPHERE AND IONOSPHERE TO VARIOUS GEOPHYSICAL CODITIONS"** in partial fulfilment of the requirements for the award of the Degree of Doctor of Philosophy and submitted in the Department of Physics of the Indian Institute of Technology Roorkee, Roorkee is an authentic record of my own work carried out during a period from July, 2013 to November, 2018 under the supervision of Dr. M. V. Sunil Krishna, Assistant Professor, Department of Physics, Indian Institute of Technology Roorkee, Roorkee.

The matter presented in this thesis has not been submitted by me for the award of any other degree of this or any other Institute.

(GAURAV BHARTI)

This is to certify that the above statement made by the candidate is correct to the best of my knowledge.

(M. V. Sunil Krishna)
Supervisor

The Ph.D. Viva-Voce Examination of Gaurav Bharti, Research Scholar, has been held on 7thMarch 2019.

Chairman, SRC External Examiner

This is to certify that the student has made all the corrections in the thesis.

Signature of Supervisor Head of the Department

Date:

ABSTRACT

The atmosphere is the most important part that makes the Earth livable. Extensive studies have revealed various important features about the different layers of Earth's atmosphere. For example, Troposphere has been studied due to the presence of biosphere, while the stratosphere has always been of interest due to Ozone, water vapor and various active hydrodynamic processes [1–3]. The ionosphere has been studied due to the presence of significant number of free ions and electrons which can influence the radio wave propagation, communication and navigation [4–7]. A part of the atmosphere that extends from 80-200 km is known as Mesosphere-Lower-Thermosphere-Ionosphere (MLTI) and sometime referred to as MLT region. The dynamics, chemical composition, and structure of this region are significantly influenced by atmospheric waves, such as, planetary waves, tides and gravity waves as well as solar radiation [8–12]. This region is very less explored due to lack of direct observations, because it is too high for the in-situ measurements from the aircraft or balloons. Rocket or ground-based measurements on a global basis are not practically possible and they do not provide the complete set of measurements required for the characterization of MLT region. Consequently, the structure, dynamics, and the chemistry of this region are not completely understood.

A number of studies have been performed to understand the MLT region by us-

ing the ground-based observations, rocket flights, and satellite measurements [13–16]. Till date, there has not been a focused investigation of this region which has measured solar inputs, temperatures, winds, constituent's abundances, and key radiative emissions by the different atmospheric species. The thermal structure of the MLT region is determined by various mechanisms through which the region gains and losses energy. An important source of energy into the MLT region is the solar UV radiation that drives the chemistry and dynamics of the MLT region. In this region solar energy is converted to heat by the exothermic reactions and airglow that reduces the solar heating efficiency. The excess energy provided by the solar radiation into the MLT region is rapidly lost into space by thermal radiation in the infrared spectrum [17]. In particular, the 15 μm IR bands of carbon dioxide are important below 130 km altitude, while nitric oxide (NO) infra-red emission at 5.3 μm is important between 100-250 km altitudes [18]. It is well known that the infrared radiative emission by NO is the single largest cooling process in the lower thermosphere and mesosphere, which regulates this region's thermal structure [19–22]. In addition to the above atomic oxygen also plays a crucial role to enhance the cooling rate through collisional excitation of many species, by radiative emission and also by exothermic chemical reactions [23,24]. There are some other minor species such as Ozone and water vapor etc., which are also responsible for the cooling of the atmosphere at different altitudes. There has been a great progress in the last several years to understand the relative importance of different processes that are responsible for the radiative cooling; however, there is still lack of direct measurements of the abundances of radiating species that can help to quantify the energy budget of the MLT region. Recently, NASA has launched the TIMED (Thermosphere-Ionosphere-Mesosphere Energetic and Dynamics) satellite mission that carried the SABER (Sounding of the Atmosphere using Broadband Emission Radiometer) instrument to quantify the energy budget. The dynamics and the energy budget of the MLT region can be better understood by using the TIMED mission. The main objective to study energy budget of the MLT region is that, it significantly influences the climate and the thermal structure of the atmosphere during the space weather events. In addition to the phenomenon of radiative cooling as discussed above, the MLT region is also known to be a source of neutral metallic atoms (Na, Fe, Mg, Ca, K, and Si) and ions (Fe^+, Mg^+, Ca^+) [25,26]. These metal species are mainly deposited in this region due to the ablation of meteors [27]. The meteors that enter into the atmosphere at high speed, causes sputtering and flash heating due to collision with air molecules followed by rapid evaporation of metal atoms [28]. This process forms the metallic layers between the altitudes 80 to 105 km, which can be observed by the ground-based LIDAR technique, satellite based optical spectroscopy, and rocket measurements. Among the various meteoric metal species found in the atmosphere, Sodium is extensively studied due to its larger scattering cross-section which makes it a good tracer for knowing the thermal and dynamical state of the MLT region [29–31]. These metals also act as an excellent tracer for the atmospheric wave motions [32–34]. Thus, it is very important to understand the chemical and physical processes that control the distribution of metal layers in atmosphere, the resulting airglow, and how the layer can be affected by the space weather events. Till date, there are few model-based studies are reported in literature to understand the metallic layers, in the present study we have used the Na airglow model that provides the altitudinally resolved volume emission rate (VER) of airglow intensity.

Quite a few atmospheric constituents undergo characteristic spectral transitions by absorbing the solar radiation. The atmospheric emissions resulting from these transitions constitute airglow. The airglow emissions are very faint in nature and airglow over polar regions of Earth is generally known as aurora. According to the time of observations airglow emissions are classified into three categories namely, dayglow, nightglow, and twilightglow [35–37]. The dayglow and nightglow emissions are observed during the daytime and nighttime, respectively. While the twilightglow is observed when the Sun is below the horizon. The dayglow emission is the most challenging part for the ground-based observation due to high solar radiation background. Airglow emission could be very useful to remotely sense the state, structure and the dynamics of atmosphere. Severe space weather events such as geomagnetic storms can have a profound influence on the neutral and ionized atmosphere [24, 38–42] and using airglow emissions we have tried to address how the equatorial anomaly in electron density and temperature are affected during extreme space weather events.

This thesis is organized into five chapters. The content of each chapter is discussed below.

Chapter 1 is an introductory chapter containing a discussion on the classification of the Earth's atmosphere depending on the vertical temperature trend, neutral density and electron density. This chapter also briefly describes the effect of Sun and the various solar parameters in exciting atmospheric constituents and the process responsible for the occurrence of space weather phenomena such as geomagnetic storms and solar proton events.

Chapter 2 deals with the understanding of fluctuations induced in Nitric Oxide (NO) radiative flux during intense geomagnetic storms. The intense double storm during 7-12 November 2004 is considered for the present study during which O/N_2 ratio and radiative flux exiting the thermosphere at 5.3 μm as observed by GUVI and SABER instruments respectively, onboard the NASA's TIMED satellite are analyzed. This reveals that the NO radiative flux is anti-correlated to the O/N_2 ratio on a global scale. The maximum depletion in O/N_2 and enhancement in NO radiative flux is found during the main phase of the storm [24]. It has also been found that the both O/N_2 and NO flux propagate towards the equator during the main phase of the storm. The possible reason for the enhancement of radiative flux during the storm period is established using global models. The nature of the correlation between radiative flux and neutral atmospheric parameters is established using NRLMSISE-00 over a mid-latitude location. In order to understand how the storm influences the NO abundance, a model has been developed using the measured values of radiative flux. This model indicated a 3-15 times increase in the abundance of NO during the main phase of a storm to be able to account for the observed change in radiative flux [24]. This study reveals that the collisional excitation of NO with atomic oxygen as the most dominant process contributing to the cooling of thermosphere during intense geomagnetic storms.

Chapter 3 describes the latitudinal and longitudinal variation of peak emission of NO VER, and corresponding [O] over the Asian sector during two intense geomagnetic storms. The peak emission of NO VER and corresponding atomic oxygen number density ([O]) have been obtained from the TIMED/SABER instrument and the NRLMSISE-00 model, respectively. The results suggest that during the geomagnetic storms the neutral and ion densities are modulated significantly. In order to quantify how the peak emission of NO VER is influenced over the Asian sector, we have analyzed the peak emission of NO VER and correlated it with the [O]. It has been found that near equatorial region the peak emission of NO VER is minimum, while towards the mid latitude the cooling becomes more prominent during the geomagnetic storm, and maximum peak emission of NO VER is found at the higher latitude region. On the other hand, the variation of [O] shows an opposite trend as found in the case of peak emission of NO VER at the higher latitudes during the geomagnetic storms. Consequently, the peak emission of NO VER and corresponding [O] can be seen as negatively correlated at the higher latitudes, while at the mid-low latitudes both, peak emission of NO VER and corresponding [O] are positively correlated. The observed Dst index also shows the positive correlation with [O] at the higher latitudes, while negative correlation at mid-low latitudes.

Chapter 4 describes the effect of space weather events (SWE) on sodium airglow emission. The comprehensive model to calculate the vertical VER profile of sodium airglow emission has been used in the present study. This model has been validated with the rocket measurements, MULTIFOT campaign, the LIDAR, and the photometer observations reported in the literature [25, 29]. This model incorporates the neutral chemistry, the ion chemistry, and the photochemistry along with the latest reaction rate coefficients. Extreme space weather events are identified during which sodium airglow emission is modeled. The neutral sodium density and temperature have been obtained from the LIDAR facility at Utah State University. The neutral and ion densities, temperatures required for the model have been derived from NRLMSISE-00 and IRI-2, respectively. Ozone plays a very important role in the excitation mechanism of Na airglow. The columnar profiles of Ozone derived from SABER measurements are used in the model. During the SWE the modeled VER emission rate of Na airglow shows significant variation. It mainly depends on the abundance of Na and O_3. The Na and O_3 densities show maximum depletion during the main phase of the SWE. Consequently, the VER of Na airglow also shows depletion during the main phase of the SWE. In addition to the above, the nightly averaged Na density is also found to be depleted during the space weather events suggesting a strong correlation with the storm index. The earlier studies have reported conflicting results about the variation of Na abundance during geomagnetically disturbed conditions [43–46]. We have tried to provide a comprehensive understanding of the fluctuations in abundance and airglow intensity by combining satellite and ground-based observations with a physics based model.

Chapter 5 describes the influence of severe geomagnetic storms on the equatorial ionization anomaly (EIA) and equatorial temperature anomaly (ETA) using the atomic oxygen airglow emissions at 557.7 nm (greenline) and 732.0 nm during the ascending phase of the solar cycle 24. The EIA and ETA are very well known equatorial phenomenon, the objective is to study how they will be influenced by the strong geomagnetic activity [24]. Any variation in the strength of EIA and ETA can be observed in atmospheric parameters such as electron density, temperature etc. At the same time, the airglow emissions are also very sensitive to these parameters. Hence, by studying the latitudinal variation in airglow emission intensity, it is possible to establish a connection between parameters related to airglow, EIA and ETA. This study is primarily based on photochemical modeling of the two airglow emissions with the necessary input obtained from global models, theoretical studies and experimental observations. It is found that the modeled VER rate of 557.7 nm shows a positive correlation with the Dst index at 150 km and negative correlation at 200 and 250 km altitudes. The latitudinal variation of greenline emission looks similar

to that of electron density with crests on either side of the equator. This is due to the sensitivity of greenline emission chemistry to electron density and temperature. Interestingly the 732.0 nm emission although very sensitive to the electron density shows a trend opposite to that of EIA. Day-to-day latitudinal variation of greenline emissions at 150 km altitude is negatively correlated to the ETA, while at 200 and 220 km it is found to be positively correlated. In the case of 732.0 nm emission, day-to-day latitudinal variation shows a positive correlation with the ETA at the considered altitudes.

List of Publications

Articles in Journals

1. Gaurav Bharti, M. V. Sunil Krishna, T. Bag and P. Jain, Storm time variation of radiative cooling by nitric oxide as observed by TIMED-SABER and GUVI, *J. Geophys. Res: Space Physics.,* **123**, *1500–1514 2018.*

2. Gaurav Bharti, T. Bag, M. V. Sunil Krishna, Effect of geomagnetic storm conditions on the equatorial ionization anomaly and equatorial temperature anomaly, *J. Atmos. Sol-Terr. Phys.,* **168**, *8-20, 2018.*

3. Gaurav Bharti, V. Singh and M. V. Sunil Krishna, Radiative cooling due to NO at 5.3 μm emission as observed by TIMED/SABER over Asian sector, *revision submitted, J. Adv. Space Res., 2018.*

4. Gaurav Bharti, M. V. Sunil Krishna, Effect of space weather events on sodium airglow emission, *under review, J. Geophys. Res: Space Physics., 2018.*

Papers in Conferences/Symposia:

1. The greenline dayglow emission under geomagnetic storm conditions.
   T. Bag, Gaurav Bharti, and M. V. Sunil Krishna
   National Space Science Symposium-2014
   Dibrugarh University, Dibrugarh, Assam
   January 29-February 1, 2014.

2. SABER-TIMED observation of infrared cooling over Asian sector.
   Gaurav Bharti, M. V. Sunil Krishna
   National Space Science Symposium-2016
   Space Physics Laboratory, Vikram Sarabhai Space centre, India
   9-12 February, 2016.

3. Storm time variation of radiative cooling of thermosphere by nitric oxide emission.
   M. V. Sunil Krishna, Tikemani Bag, and Gaurav Bharti.
   41st COSPAR Scientific Assembly
   Istanbul, Turkey (2016).

4. Radiative cooling of Nitric Oxide emission observed by TIMED-SABER over Asian sector during severe geomagnetic storms.
   Gaurav Bharti, M. V. Sunil Krishna
   JpGU-AGU Joint Meeting
   Makuhari Messe, Chiba, Japan
   20-25 May, 2017.

5. The effect of space weather on sodium airglow emission.
   Gaurav Bharti, M. V. Sunil Krishna.
   14th Solar-Terrestrial Physics Symposium
   York University, Toronto, Canada.
   9-13 July, 2018.

6. Influence of solar proton event on the infrared radiative cooling by Nitric Oxide.
   M. V. Sunil Krishna, Gaurav Bharti
   14th Solar-Terrestrial Physics Symposium
   York University, Toronto, Canada
   9-13 July, 2018.

7. Effect of Geomagnetic storm conditions on the equatorial ionization anomaly and equatorial temperature anomaly.
   Gaurav Bharti, M. V. Sunil Krishna
   42th COSPAR Scientific Assembly
   Pasadena California, USA
   14-22 July, 2018.

8. Variation of radiative cooling and nitric oxide abundance during intense geomagnetic storms as observed by TIMED/SABER and GUVI.
   M. V. Sunil Krishna, Gaurav Bharti
   42nd COSPAR Scientific Assembly
   Pasadena California, USA
   14-22 July, 2018.

Workshops/Conferences/Symposia Attended:

1. 18th National Space Science Symposium
   Dibrugarh University, Dibrugarh, Assam (India)
   January 29-February 1, 2014.

2. Summer School on Basics of Atmospheric Sciences
   S. V. University, Tirupati (India)
   June 4-28, 2014.

3. 19th National Space Science Symposium
   Space Physics Laboratory (SPL)
   Vikram Sarabhai Space centre (VSSC),
   Thiruvananthapuram, Kerala (India)
   February 9-12, 2016.

4. JpGU-AGU Joint Meeting
   Makuhari Messe, Chiba, Japan
   20-25 May, 2017.

5. 42nd COSPAR Scientific Assembly
   Pasadena California, USA
   14-22 July, 2018.

ACKNOWLEDGEMENTS

I wish to express my heartfelt gratitude and deep respect to my supervisor ***Dr. M. V. Sunil Krishna***, Assistant Professor, Department of Physics, Indian Institute of Technology Roorkee, for his invaluable guidance, unlimited continuous support, constructive criticism, thought provoking discussions and painstaking efforts throughout the course of work and made this thesis possible. He has been a constant source of encouragement and inspiration to me. He is true epitome of goodness and company and assurance at the time of crisis would be remembered lifelong. He, not only groomed me as a researcher, but also imparted wisdom that transformed me in to a confident human being. His insight, quest for perfection, and passion for science has always inspired me. I am very thankful to him for his support in academic as well as non-academic affairs.

I take the opportunity to thank to *Prof. Vir Singh*, and *Dr. Sumanta Sarkhel* Department of Physics, Indian Institute of Technology Roorkee, for the valuable discussions related to my research work. I take the opportunity to thank to *Dr. K. L. Yadav*, Professor and Head and *Dr. Rajesh Srivastava*, Professor and former Head, Department of Physics, Indian Institute of Technology Roorkee for providing the basic infrastructural facilities for carrying out this research work. I thank the members of my student research committee; *Prof. G. D. Verma* (Chairman), *Dr. A. K. Gour-*

ishetty (Internal member) Department of Physics, and *Dr. A. S. Maurya* (External member) Department of Earth Sciences, for their valuable questions/comments and remarks on earlier presentations of this work. I would like to thank all the faculty members of Department of Physics, Indian Institute of Technology Roorkee. I also thank, Mr. Kishan Lal, Mr. Arvind Kapil, and all other employees of both technical and non-technical divisions of the department for their cooperation and helpful attitude extended to me during the tenure of my research work.

The inspiration, support, cooperation and patience which I have received from my friends are beyond the scope of any acknowledgement, yet I would like to express thanks to my seniors, juniors and friends *Neha Kanaujia, Yogesh, Avijit Dewasi, Avijeet Ray, Dushant Kumar, Prabhat Kumar, Prabhakar Srivastav, T. Bag, Asit Sahoo, Vikas, Karunav, Jatin, Narendra patel, Swati Garg, Shubhchintak, Thiru, Sant, Maneesha, Mahima, Gagan, Priti, Renu, Dr. Swati Modi, Pramod, Subarna Mondal,Alok and others* for their company and for the quality time that I spent with them. I would like to express my heartfelt thanks to my fiance *Neha* who was always there during my hard time.

Vocabulary fails me to put proper words expressing my sentiments for my parents and my family members for their unconditional support, love and encouragement.

I gratefully acknowledge the financial support provided by *Ministry of Human Resource and Development (MHRD)*, New Delhi, India in the form of junior and senior research fellowships during the period of research. I acknowledge *T. Yuan* and SABER team for providing me data.

Date:............ (Gaurav Bharti)

Dedicated to My Parents

Jugendra Singh and Preeti Bharti

CONTENTS

LIST OF FIGURES

LIST OF TABLES

CHAPTER 1

GENERAL INTRODUCTION

1.1 Introduction

The Earth's atmosphere is an important part that makes the Earth livable. It protects us from the harmful solar radiation and regulates heat, provided by the Sun. To understand the different processes occurring in the atmosphere, extensive studies had been performed on different regions of it. For example, Troposphere has been studied because of its immense importance to the biosphere, while the Stratosphere has always been of interest due to the presence of water vapor, Ozone, and a number of active hydrodynamic processes. The ionosphere has been studied due to the presence of a significant number of free ions and electrons which can influence the radio wave propagation, communication, and navigation. The thermosphere is the source region for the ionosphere. The region of Earth atmosphere that extends from 80-250 km is known as Mesosphere-Lower Thermosphere-Ionosphere (MLTI) sometimes referred to as MLT region. This region is the least explored as compared to other regions such as troposphere and stratosphere. This is due to the difficulties in making direct observations and measurement of various parameters representing this region. As a consequence, many interactive processes between the ionized (ionosphere) and the neutral constituents of the MLTI region are not very well understood. This region is highly dynamic in nature due to the selective absorption of solar radiation by the atmospheric constituents. An important source of energy into the MLTI region is the solar ultraviolet (UV) radiation. This region also acts as a gateway between the space and Earth's atmosphere. It has been noticed in the recent years that many processes in this region are strongly correlated to each other and they are also coupled with the processes in other atmospheric regions. Recently, National Aeronautics and Space Administration (NASA) launched the Thermosphere-Ionosphere-Mesosphere Energetics and Dynamics (TIMED) satellite to conduct the investigation of MLTI region between altitudes 80-250 km. This satellite mission has provided a wealth of information about various processes and dynamics that are active in the MLTI region. The key objectives of this thesis are to study the aeronomical aspects of Na airglow emission and infrared emission in the MLTI region by the means of coordinated modeling and satellite data analysis. We have presented the compilation of details and important results from our study of few important atomic oxygen airglow emissions, Sodium (Na) airglow emission, and thermospheric infrared radiative emission by Nitric Oxide (NO).

1.2 The Earth's atmosphere

The atmosphere is a layer of gases that surround the planet and is retained by the Earth's gravity. The Earth is the only planet in the solar system which has an atmosphere suitable for the existence of life. The gases surrounded by the Earth contains the air that we breathe but it also protects us from the harmful radiation emanating from the Sun. The Earth's atmosphere absorbs almost all harmful solar radiation which is dangerous to sustain the life. In addition to the above, the atmosphere also controls the temperature on Earth's surface making the Earth habitable.

1.2.1 Structure of neutral atmosphere

The Earth atmosphere mostly consists of N_2, O_2, O and a small amount of other trace gases. The atmosphere is mainly described by three parameters namely, pressure, density, and temperature. The atmospheric pressure and density decrease with increasing altitude while temperature shows an unusual variation with the altitude. The Earth atmosphere can be divided into four regions based on the altitudinal temperature variation, the troposphere, the stratosphere, the mesosphere, and the thermosphere. Figure 1.2 shows the structure of the atmosphere.

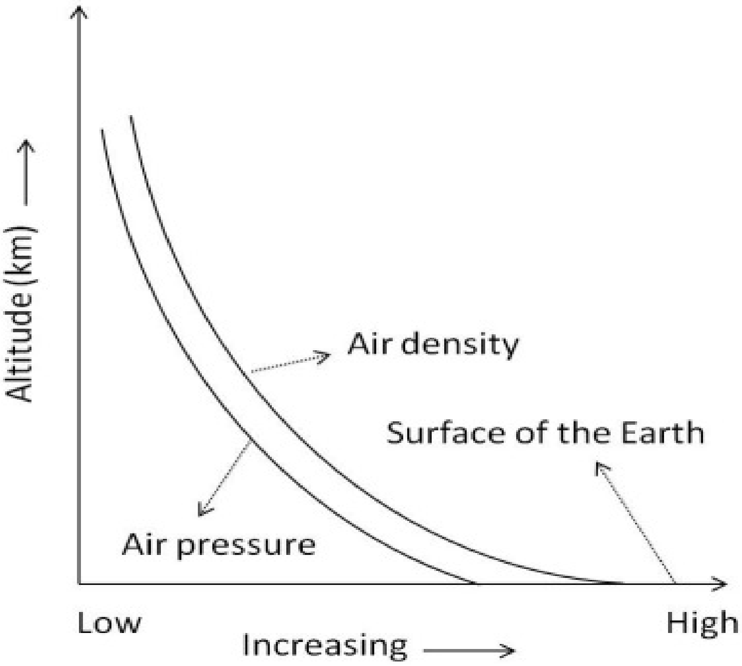

Figure 1.1: Schematic digram of variation of pressure and density with altitude [47].

1.2.1.1 Troposphere

This is the lowest part of the atmosphere where we live. The height of the troposphere is not the same all over the globe. At the polar region, it varies from 8-10 km, while at the equator 16-18 km, above the sea level. This region is the most important part for the existence of life because; it contains about 70-80 percentage of atmospheric

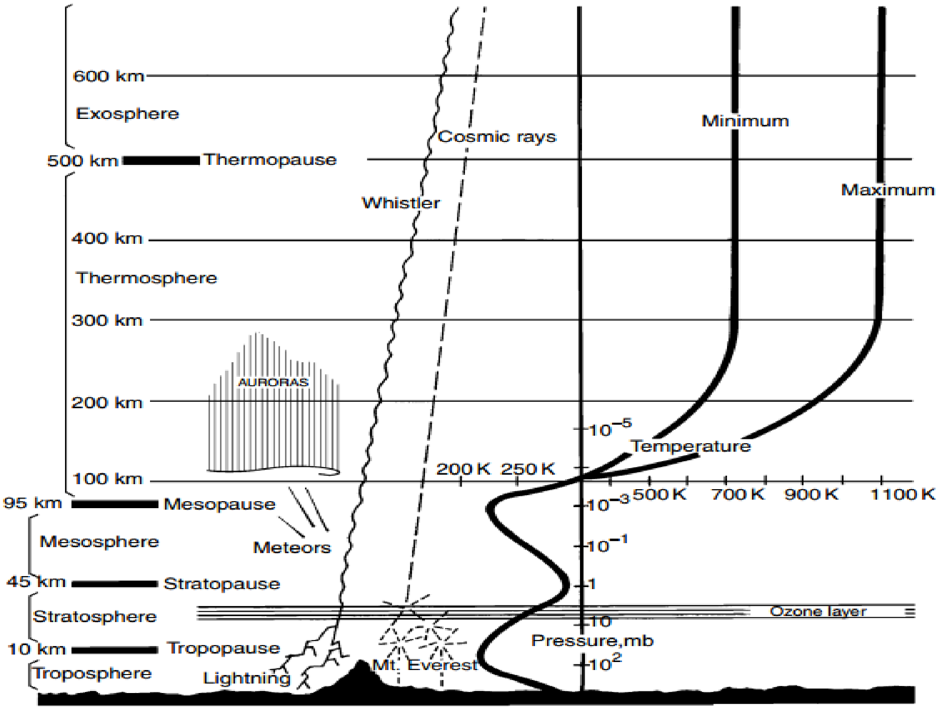

Figure 1.2: Schematic digram for the variation of temperature in Earth's atmosphere [48].

mass and nearly 99 percentage of water vapor and clouds. Therefore, all the weather phenomena occur in this region. The main atmospheric constituents of this region are the N_2, O_2 with a proportion 4:1 with a small quantity of greenhouse gases like CO_2, CH_2, and chlorofluorocarbon (CFC) etc.

1.2.1.2 Stratosphere

The stratosphere is the layer just above the troposphere and contains about 20 percent of the atmospheric mass. The boundary between troposphere and stratosphere is known as the tropopause. Stratosphere contains about 90 percentage of the atmospheric Ozone. The stratospheric Ozone protects us from skin cancer and other health damages, by absorbing dangerous UV radiation. As we move towards the higher altitudes the temperature starts to increase. The increase in temperature with height occurs because of absorption of ultraviolet (UV) radiation by Ozone. The temperatures of the stratosphere are highest in summer, and lowest in winter.

The dynamical and chemical processes in this region are significantly influenced by the large volcanic eruptions.

1.2.1.3 Mesosphere

The mesosphere is the third highest layer of Earth's atmosphere, occupying the region above the stratosphere and below the thermosphere. It extends from 45 km to about 95 km and shows a negative lapse rate. This is the coldest region of the atmosphere. The important dynamic features in this region are strong zonal (East-West) winds, planetary waves, internal atmospheric gravity waves (commonly known as "gravity waves"), and atmospheric tides. During the summer solstice, the mesospheric temperature is less compared to the winter solstice. This non-uniform distribution in temperature is due to the gravity wave breaking which deposits energy and momentum in the mesosphere [53, 54]. Therefore, it reverses the mean zonal wind, which creates summer pole-winter flow of the meridional wind warming the winter mesosphere and summer mesosphere. The mesospheric temperature decreases with increasing the altitude, due to decreasing absorption of solar radiation by the rarefied atmosphere and increasing cooling by the CO_2 infrared radiative emission. In addition, the meteoroids and comets are also ablated in this region and they deposit a huge amount of metallic species, which can significantly influence the dynamics.

1.2.1.4 Thermosphere

The thermosphere extends from about 95 to 500 km. Within this region, UV radiation causes the photoionization of atoms and photodissociation of molecules creating ions. Thermospheric temperature increases with height due to the absorption of energetic solar radiation which depends on solar activity. The X-ray and extreme ultraviolet (XUV) are completely absorbed in this region. In addition to the above, Joule heating and particle heating enhance the thermospheric heating during the solar prominences. The excess heat in this region is rapidly lost into space by the Nitric Oxide (NO) and CO_2 infrared radiative emissions.

The whole atmosphere can also be classified into homosphere and heterosphere, depending on the eddy diffusion and turbulence mixing. The homosphere exists below the turbopause (around 100 km), that is well mixed and uniform; while the heterosphere exists above the turbopause where atmospheric gases are distributed corresponding to their molecular weight, heavier gases remain in the lower altitudes while lighter ones move towards the higher altitudes.

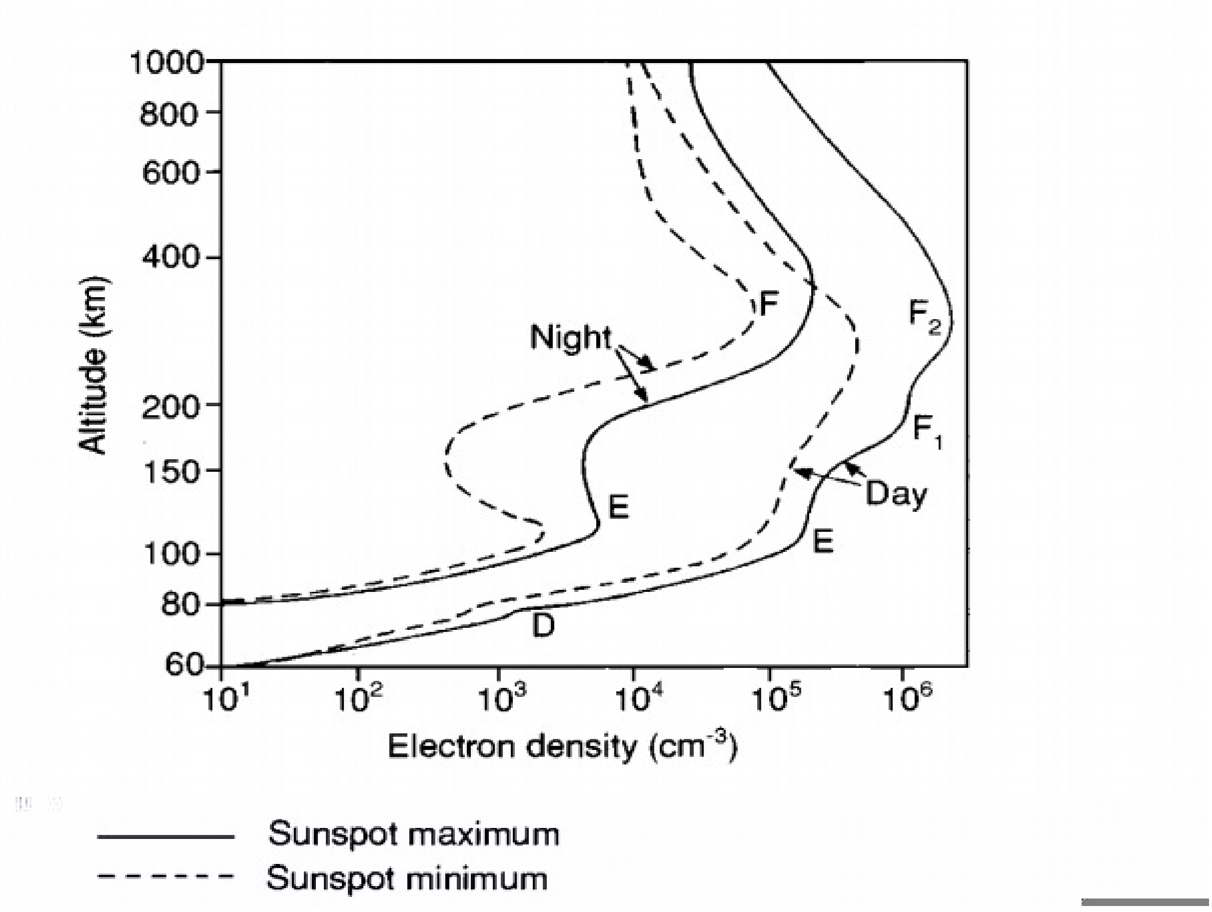

Figure 1.3: Typical profile of ionosphere based on the electron density [49].

1.2.2 Ionosphere

The existence of ionosphere was clearly established in 1901 when Guglielmo Marconi successfully transmitted radio signals across the Atlantic. The ionosphere is the ionized portion of the atmosphere that extended from 60 km to 1000 km altitude range. The X-ray, UV, EUV, and energetic particles are responsible for the ionization of this region. Due to the presence of charged particles, this region plays a crucial role for the navigation, communication, and propagation of radio waves [55–62]. The variation of electron density in this region is not uniform. This region can be classified into the three regions, namely, D-layer, E-layer, and F-layer, as shown in Figure 1.3. These regions contain, both positive and negative charged particles, and maintain an overall charge neutrality.

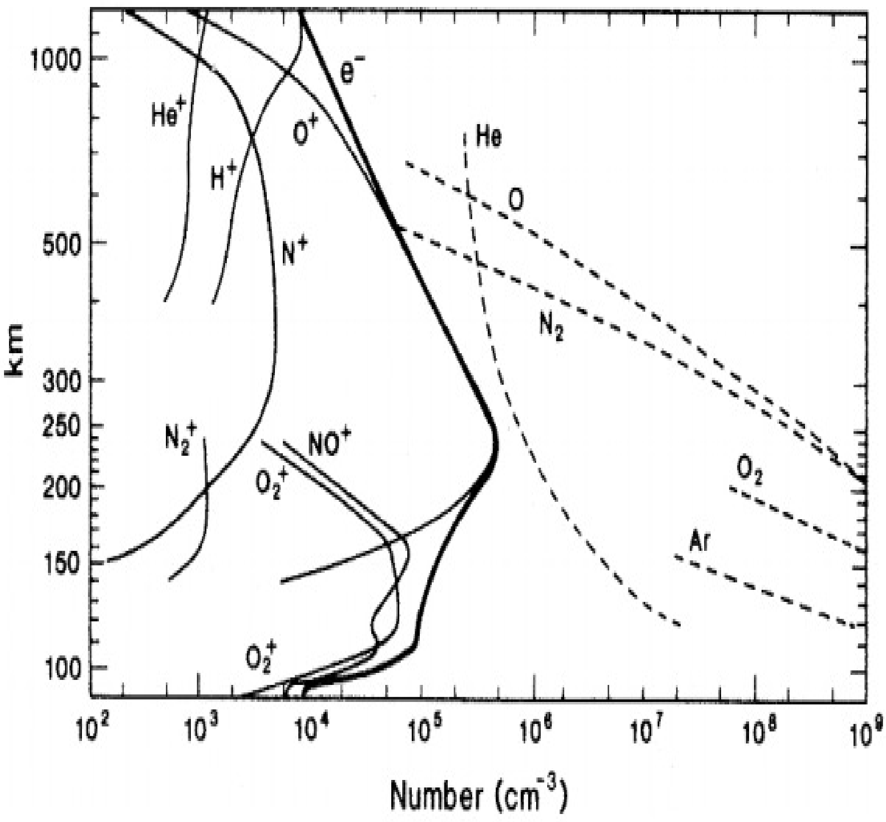

Figure 1.4: Dayside Ionospheric plasma density and neutral density profiles during solar minimum [50].

During night time the electron density in E- and F- regions decreases by a factor of ~ 100 [63]. Figure 1.4 shows the ions and neutral density profiles of a few major species in the ionosphere. It is well known that the D-region is the lowest region of the ionosphere which is extended from 60 km to 90 km. In this region molecular ions (O_2^+ and NO^+) are dominant while neutral species such as NO, H, and N are present in small concentration [64]. In addition to the above, higher solar activity can generate the hard X-ray (wavelength less than 1 nm) that can also ionize the N_2 and O_2 molecules in the D-region. The average electron density is about 10^3 cm^{-3} in the daytime during minimum solar activity. The recombination rate in this region is very high; therefore, neutral species are more compared to ions. Just above D-region there is the E-region in the middle of the ionosphere, which is extended from 100-150 km. The major ions in this region are NO^+, O_2^+, and N_2^+. The ionization of NO^+, O_2^+, and N_2^+ in this region are due to Lyman-α, Lyman-β, and charge exchange reaction, respectively. The total ion densities in this region are the order of 10^5 cm^{-3}, while neutral densities greater than 10^{11} cm^{-3}. Therefore, the E-region plasma is weakly ionized, and collisions between charged particle are not important. The ionization in this region is rapidly lost during the sunset, due to the absence of the primary source, unlike D-region. A significant amount of meteoric metals such as Na^+, Fe^+, Mg^+, Al^+, and Ca^+ also exists in this region due to meteoric ablation. Just above the E-region there exists the F-region. This region also known as the Appleton-Barnett layer, extending from 150-800 km above the Earth surface. This layer contains maximum electron density at noon time 10^6 cm^{-3}, which is roughly a factor of 10 greater than that in the E-region [65]. In this region the atomic species (O^+ and O) dominate, due to their long lifetime. In the daytime the F-region is divided into F_1 and F_2 layers due to influence of molecular ions. However, during night-time, F_1 layer disappears completely. The space above F-region is called protonosphere. This region is dominated by the lighter atomic ions such as H^+ and He^+.

1.3 The Sun and its variability

1.3.1 The Sun

Sun is a main sequence G2V star at the center of solar system, with an average mass 1.99×10^{30} kg, radius 6.96×10^5 km, and luminosity 3.9×10^{26} watts and consists of about 99.86 percent of the entire mass of solar system. The structure of Sun has been classified into four regions depending on the mode of energy transport. These regions are namely, the core, the radiative zone, the convective zone, and the solar atmosphere. The core is the central part of the Sun. The density slowly decreases as we move away from the core. Radiative zone is a layer just above the dense core. In this zone the temperature drops from approximately 7 million to 2 million Kelvin with increasing distance from the core. This temperature gradient is less than the value of adiabatic lapse rate and the matter in this region is present in a completely ionized state. Consequently, the energy transfer through this region is only due by radiation, but not from convection process. The convection and radiative zone are separated by the thin boundary called as tachocline. Convection zone lies just above the radiative zone. The bottom of convection zone is heated by the radiation emanating out form the radiative zone. The temperature at the bottom (around 200,000° C) is very large compared to top of convection zone (around 5700° C). This difference in the temperature results in a physical phenomenon known as convection. Therefore, the mode of transport of energy in this region is by convection. The region above the convective zone is known as the solar atmosphere. The solar atmosphere can again be classified into three regions, namely, photosphere, chromosphere, and corona, depending on the density and temperature variation. The lowest layer of the atmosphere is known as the photosphere, extended up to around 500 km from the surface. Photosphere absorbs almost all energy from the convection and act as black body radiator at a temperature of 5800 K, and about 99 percent radiation is emitted from this region. The particle density in this region is of the order of 10^{14} cm^{-3}. The temperature of the photosphere decreases towards the higher altitude. The maximum temperature of the photosphere at the bottom is around 6600 K, while at the is top 4200 K. The temperature above the photosphere increase sharply. The region above the photosphere is known as chromosphere which is around 3000 km thick, with a density of 10^{23} cm^{-3}. The temperature in this region increases rapidly, and reaches nearly 10^4 K at the top of the chromosphere. This region is the source of ultraviolet radiation and hydrogen-α lines. Just above the chromosphere, there exists the transition region extended up to around 3000 km. In this region temperature rise sharply up to 10^6 K. This region links the chromosphere and the corona. The corona is the outer most part of the solar atmosphere which extends into the interplanetary space. The expanding corona into the outer space is called the solar wind. The corona is the source region for geomagnetic storms and solar energetic particles (SEPs) which severely modulate the Earth's atmosphere and ionosphere.

1.3.2 The solar radiation

Sun is the ultimate source of the energy, which continuously emits the radiation into space in the form of electromagnetic radiation. The complete range of electromagnetic radiation is known as the solar spectrum. The solar spectrum consists of number of the dark lines called Fraunhofer lines, which provide information about the presence of different species in the solar atmosphere. The solar radiation influences the Earth's atmosphere depending on the altitude of its absorption. According to the wavelength, the solar spectrum can be classified into different categories, as seen in Table 1.1.

Table 1.1: Classification of Solar spectrum

Solar spectrum	Wavelength
Cosmic and Gamma rays	<0.1 nm
X-rays	0.1 - 10 nm
Ultraviolet	10 -400 nm
Visible	400 -700 nm
Infrared(IR) and Thermal	700 -10^6 nm
Radio waves	$> 10^6$ nm

1.3.3 The F10.7 solar index

The solar flux is a basic parameter to measure solar radiation, which is very important in aeronomy. It is defined as the amount of solar photons incident over a unit area per unit time, for a particular wavelength. Figure 1.5 shows the variation of solar irradiance with wavelength. This figure shows the contribution of the visible and infrared radiation is approximately half of the solar spectrum and maximum fluctuation is found in the UV and EUV radiation. The solar radiation of wavelength less than 120 nm mainly originate from the chromosphere, transition zone, and corona. The radiation between wavelength 120-200 nm is emitted from the lower part of the chromosphere and photosphere, and wavelength greater than 200 nm is emitted from the photosphere [66]. There are a number of solar indices which can quantify the solar flux. Amongst them, F10.7 is the main solar index which is widely used to monitor solar flux, due to the transparency of longer wavelength in the Earth's atmosphere and it also represents the noise level produced in the Sun at 10.7 cm wavelength [67].

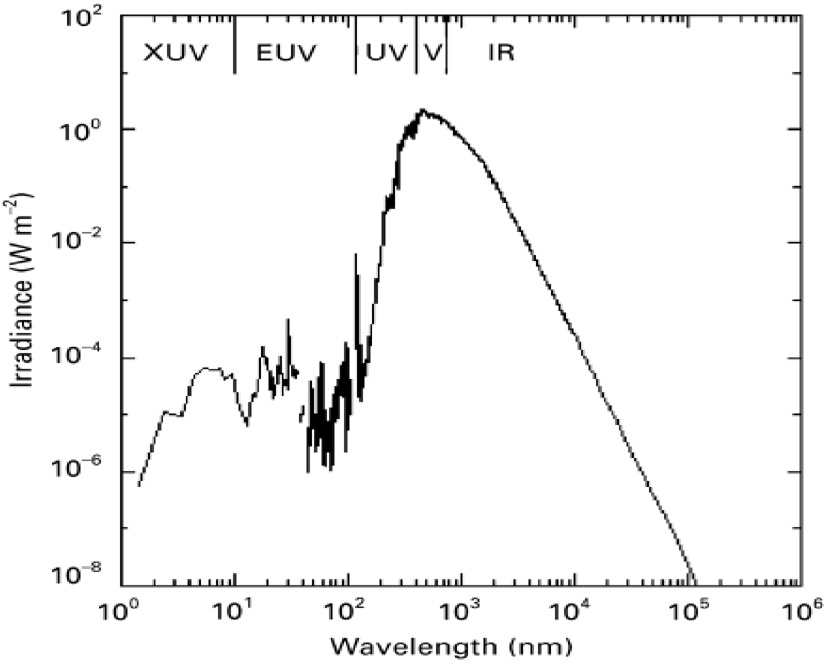

Figure 1.5: Spectrum of solar Irradiance from X-ray to Infrared [51].

The F10.7 cm wavelength originates from the chromosphere and corona of the solar atmosphere which is also the main source of the space weather phenomena. Therefore, it's an excellent tracer for solar activity. The F10.7 flux is measured in term of solar flux unit (sfu). One sfu is equal to 10^{-22} W $\cdot$m^{-2} $\cdot$Hz^{-1}. Continuous

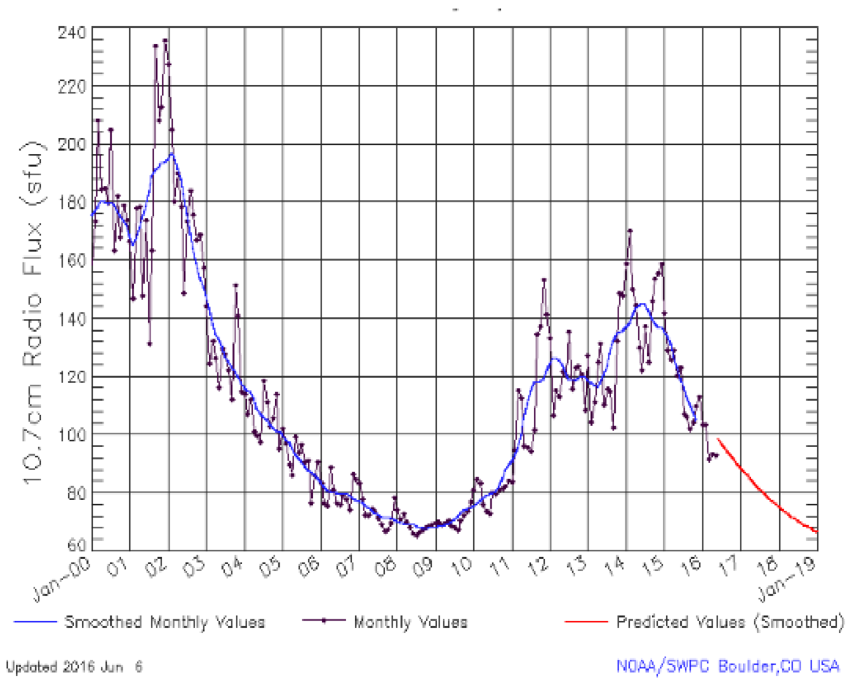

Figure 1.6: Progression of F10.7 solar flux over the period January 2000-January 2019. Courtesy: $http://www.swpc.noaa.gov/products/solar-cycle-progression$.

measurement of F10.7 were first done at Ottawa by A. E. Covington [68].

The variation in solar flux F10.7 cm is shown in Figure 1.6 from January 2000 to January 2019. The variation in the UV radiation also shows an excellent correlation with the solar flux F10.7 cm because, both are originated from the chromosphere and corona [69, 70]. The solar flux F10.7 shows a close relationship with the 11-year solar cycle and 27 days solar rotation [68, 71]. The F10.7 solar flux is currently used as the proxy to study the UV radiation, which affects the structure, chemistry, and the

Table 1.2: Solar spectrum variability over solar minimum to solar maximum

Solar spectrum	Wavelength (nm)	Variability
Infrared & Visible	>400	Extremely small
Near UV	300-400	small
Middle UV	200-300	1-2%
Far UV	100-200	10-12%
EUV & X-rays	<100	Extremely High
Lyman-α	121.6	High

dynamics of the Earth's atmosphere [72].

1.3.4 Measurements of the Solar Ultraviolet (UV) flux

The solar spectrum is highly variable for the UV and EUV flux over the period of solar maximum to minimum. The UV and EUV radiance primarily influences the dynamics and the chemistry of the atmosphere by heating and ionization. These radiations also deposit a huge amount of energy into the polar region. Therefore, the temperature and the wind pattern are also modulated. The UV and EUV radiations significantly influence the abundance of atomic oxygen and molecular nitrogen in the MLT region. These effects that are induced by EUV and UV will be a matter of discussion in this thesis.

The measurement of UV and XUV radiation is difficult at the Earth's surface due to atmospheric absorption. Therefore, it is measured above the Earth's atmosphere, which is only possible by using the rocket and satellite-based methods. The direct measurements of solar EUV irradiance carried by instruments onboard satellites and rockets are available continuously only from last three solar cycles. For the first time observation of UV spectrum below wavelength 340 nm was reported by Baum et al. [73] in 1946, with the help of a spectrograph onboard the V-2 rocket. Subsequently, several satellite, rocket, and theoretical studies were performed to measure the solar UV flux [74–77]. The first of such effort was made by the NASA in 1962 with the Orbiting Solar Observatory (OSO) program. The main objective of the OSO mission was to study the solar flux during the solar cycle 20. During OSO program from 1962-1975, eight satellites were launched. The first satellite (OSO-1) of this program was launched on 7^{th} March 1962 at an altitude of 600 km. Therefore, fist continuous solar flux was observed by OSO-1 satellite [78, 79]. OSO-1 satellite measured the first solar flux from 17 nm to 37 nm [78, 80]. A number of satellites were launched such as Atmospheric-Explorer (AE) and Nimbus, to explore more about the variation in the solar flux. The Atmospheric-Explorer mission (AE-C, AE-D, and AE-E) was launched in between 1973-1975 to measure the EUV solar flux during the ascending phase of solar cycle 21. This mission consisted the extreme ultraviolet spectrometers which measure EUV flux between 14-185 nm range during the 21 solar cycle [51,81,82]. To measure the middle UV radiation Nimbus-3 and Nimbus-4 satellites were launched with carrying photometers [83]. In addition to the above, rocket measurement were also performed to study the solar flux between wavelength 30 nm to 100 nm in 1988 [84]. Recently, several space missions have been launched to measure the solar flux. A joint mission of European Space Agency (ESA) and NASA, launched the Solar and Heliosphere Observatory (SOHO) on 2 December, 1996 to measure the solar flux. Initially, SOHO mission was planned for two years however, it is continuously monitoring the Sun after 20 years in space. The main objective of this mission is to study the internal structure of the Sun and its outer atmosphere, as well as the origin of the solar winds and coronal mass ejections [85].

Recently, NASA launched another satellite on 7 December 2001, named as Thermosphere Ionosphere Mesosphere Energetics and Dynamics (TIMED), to study the Mesosphere and Lower Thermosphere (MLT) region of the Earth's atmosphere. TIMED satellite consisted of four instruments namely, GUVI (Global Ultraviolet Imager), SABER (Sounding of the Atmosphere using Broadband Emission Radiometry), TIDI (TIMED Doppler Interferometer), and SEE (Solar Extreme Ultraviolet Experiment). The SEE instrument measures the solar soft X-rays, extreme-ultraviolet and far-ultraviolet radiation that is deposited into the MLT region [86,87]. Beside the above mention missions, a large number of satellites are being used to study the solar flux. The name of some satellite missions are EURECA, GOME, NOAA, GOES, UARS, Hinode (Solar-B), EOS/TSIM, SME, SORCE, and STEREO.

1.3.5 Models of solar UV radiation

The solar flux is initially absorbed in the Earth's atmosphere and influences the structure and the dynamics. The solar radiation was not completely measured till 1990s. To study the complete solar flux, several empirical models and reference spectra were developed and many satellite and rocket based observations were made. The AE satellites (AE-C, AE-D, AE-E) which consisted spectrometers measured the solar flux from 24 nm to 185 nm. The AE-C satellite observation and rocket measurements reported the solar flux between 24 nm to 194 nm wavelength as F74113 reference spectra [82, 88]. To make more reliable solar flux Tobiska & Barth. [89] developed the EUV flux model based on the reference spectra SC#REF. This model is most widely used to reproduce solar flux because it utilizes the solar flux from the rockets, AE-E satellites, and Solar Mesosphere Explorer along with the irradiance from Woods et al. [84]. However, during the solar minimum period, solar EUV flux model is incapable to reproduce the photoelectron flux. To overcome this drawback Richards et al. [90] developed a EUV flux model for the aeronomic calculation (EUVAC) on the basis of reference spectra F74113. The results of this model show a good agreement with the observations made by Dynamics Explorer satellites, rocket, and Atmospheric Explorer-E. However, none of the above models provide the full-disk spectrum in a self-consistent manner.

Tobiska et al. [91] developed an empirical model known as SOLAR2000, to account for the full-disk solar spectrum between 1 nm to 10,00,000 nm. The main objective of this model is to deem the spectral and temporal variability of Sun over the entire spectral range. In this model a new solar flux unit E10.7 is implemented. The E10.7 proxy is defined as the actual amount of energy (EUV) reaching at the 1 AU (Astronomical Unit). This model is well tested for aeronomic calculations [47, 92–94]. In the present thesis, we have used SOLAR2000 model to obtain the solar flux for various cases.

1.4 Solar-Terrestrial interactions

The solar-terrestrial interaction is normally considered as the effect of the expanding solar corona, the solar wind, together with the embedded remnant of the solar magnetic field, the interplanetary magnetic field (IMF) on the Earth's atmosphere.

The Sun continuously emits large amounts of radiation and high plasma consisting of energetic charge particles. The stream of highly energetic charged particles is known as the solar wind. Hence we can say that Earth is coupled with Sun by the means of energy in the form of electromagnetic radiation and energy of solar energetic particles. The solar radiation is absorbed in the Earth's atmosphere at various altitudes. The absorption of solar radiation depends on the presence of neutral species and the wavelength of the radiation. The Earth's atmospheric chemistry and dynamics are significantly influenced by the absorption of the solar radiance. The upper atmosphere blocks out almost all X-rays and UV radiation before it reaches to the Earth's surface. The altitudinal profile of the percentage attenuation and absorption of radiation is shown in Table 1.4. The UV radiation absorption in the Earth's atmosphere is shown in the Figure 1.7. Above 80 km altitude from the Earth's surface, the ionization and dissociation of the atmosphere is due to wavelength less than 800 nm. The Lyman-α line (121.6 nm) can penetrate up to mesosphere and can influence the chemistry by ionizing the Nitric Oxide (NO) and causing photodissociation of O_2 molecules. Therefore, the NO molecules get excited by absorbing the UV radiation in the MLT region.

Although Nitric Oxide [NO] is a minor constituent, it is one of the dominant contributors to the cooling of atmosphere in the MLT region. There are two absorption regions for the molecular oxygen. One extends from 125 nm to 175 nm wavelength region. The other exists in the wavelength region of about 175 nm to 200 nm. This continuum is called as the Schumann-Runge continuum. The Schumann-Runge continuum in the region of 125 nm to 175 nm results is responsible for the dissociation O_2 in the MLT region. The Schumann-Runge continuum between 175 nm and 200 nm is important for the electronic and vibrational excitation of molecular oxygen in stratosphere-mesosphere region. The radiation of wavelength between 200 nm and 350 nm is absorbed by the Ozone present in the lower atmosphere below 50 km. The wavelength higher than 700 nm is absorbed by the greenhouse gases such as carbon dioxide (CO_2), and the water vapor (H_2O).

Table 1.3: Percentage of the absorption of solar radiation in Earth's atmosphere.

Wavelength(λ) (nm)	Solar energy (By Fraction)	Altitude (km)	Primary Absorption mechanism	Absorption (%)
$\lambda < 100$	3 parts a million	90-200	Ionization of atmospheric species	100
100-200	100 parts a million	50-100	Photoionization, photodissociation of O_2 molecules	100
200-300	1.75 %	25-60	Photodissociation of ozone	$>$ 95 %
300-700	$\sim$ 48 %	-	Ozone	Very small
$>$ 700	$\sim$ 50 %	0-10	Absorption by water vapor and greenhouse gases	0-15 %
Lyman-α (121.6)	A few parts per million	60-90	Ionization of NO, photodissociation of O_2	100

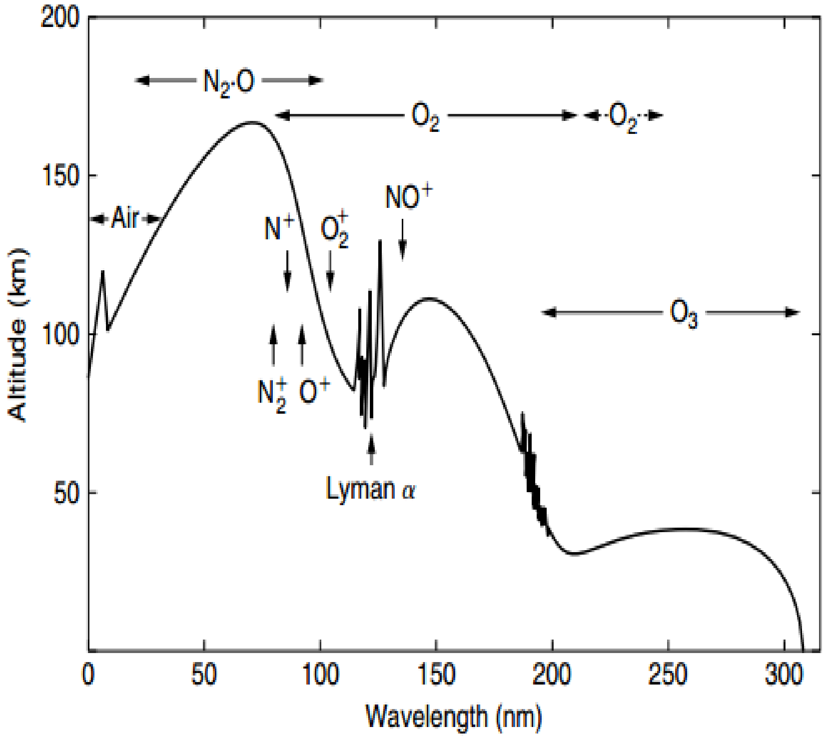

Figure 1.7: Absorption of solar UV flux by the atmospheric species [52].

1.5 Geomagnetic storm

Sun continuously emits ionized plasma clouds that consist a large amount of hot plasma. During the active cycle of Sun, it emits larger solar flares and high-speed solar winds. When solar disturbances reach in the vicinity of Earth, they create fluctuations in the Earth's magnetic field, known as geomagnetic storms. The geomagnetic storm can affect the Earth-orbiting satellite (especially those in high geosynchronous orbits), astronauts, electric power, navigation, communication, and human life [95, 96]. The storm also affects the surface of Earth by the means of geomagnetically induced currents (GIC). During the geomagnetic storm conditions, the high frequency radio waves and sudden increase in the drag force on the low-latitude satellites were also found [96, 97]. The magnetosphere is the buffer layer between the hot solar wind plasma and Earth's atmosphere.

The Earth magnetosphere plays a vital role to shield the atmosphere. When the charged particles interact with the magnetosphere, they are trapped into the inner region of the magnetosphere and undergo azimuthal drift due to the curvature and gradient effects of Earth's magnetic field. The motion of charged particles produces the toroidal ring current which is opposite for electrons and ions [98]. These particles undergo three types of motions, drift motion, gyration around the guiding center, and bounce motion between magnetic mirror points. The intensity of ring current in the magnetosphere is sharply enhanced due to the injection of large amount of energetic charged particles. The ring current produces a secondary magnetic field in a direction opposite to the Earth's magnetic field. As a result, we can see a decrease in the Earth's surface magnetic field. Hence, in simple terms we can say that the severity of geomagnetic storm will be proportional to the density of plasma that is injected into the ring current. It has been found that the solar wind accelerated by the CME are primary responsible to initiate the geomagnetic storm. The important parameter to decide the occurrence of geomagnetic storm is the interplanetary magnetic field (IMF) brought along with solar wind must be southward pointing, and the strength of the IMF must be $\geq$10 nT and duration must be $\geq$ 3 hours. On the dayside, solar wind squeezes the magnetosphere and elongates it along the anti-sunward side. The geomagnetic activity is defined and quantified by the disturbance storm time (Dst) index [98, 99]. The geomagnetic storm can be divided into three different phases, initial (commencement/sudden storm commencement/Onset) phase, the main phase, and the recovery phase. The initial phase indicates the solar energetic particles entering into magnetosphere due to magnetosphere-solar wind interaction [98]. Therefore, the injection of more charged particles increases the ring current and subsequently, sharp depletion is observed in the horizontal component of Earth's magnetic field. In the recovery phase, the horizontal component of Earth magnetic field returns to its pre on-set value due to the recombination of charged particles leading to the decay of the ring current. Consequently, the magnetic field of Earth returns back to the pre-onset-value. This period of returning back to pre-onset is called as the recovery phase. Figure 1.8 represents the typical variation of Earth magnetic field during storm period.

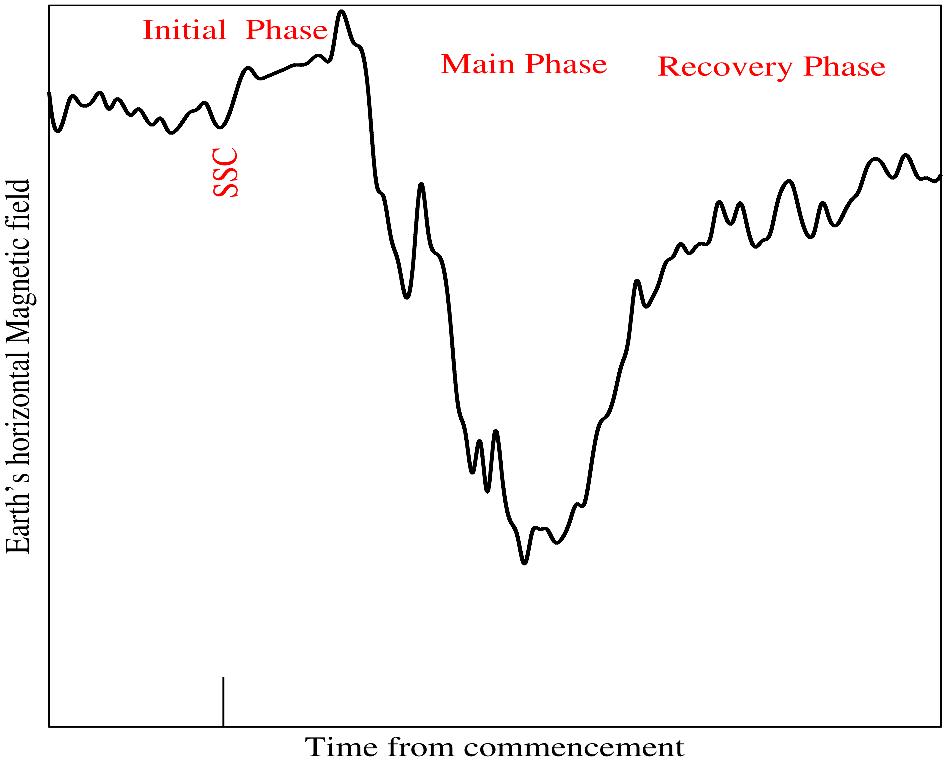

Figure 1.8: Schematic diagram of the variation of Earth's horizontal magnetic field during geomagnetic storm period.

1.6 Optical Emissions

The inbound energy in the form of particles and electromagnetic radiation excites the atmospheric species and upon subsequent de-excitation may result in the emission of optical wavelengths. This optical phenomenon is a very important tracer enabling us to remotely sense the state and structure of the atmosphere. The most important optical phenomena that are observed in the upper atmosphere are the aurora and airglow. The aurora also referred to as the polar lights, northern lights or southern lights. Both these optical phenomena differ on the basis of excitation process [100]. The aurora is mainly produced due to the interaction of highly energetic charged particles (solar wind) with the Earth's atmospheric species. The highly energetic charged particles are deflected towards the polar region due to the interaction of the Earth magnetic field. These charged particles excite the atmospheric species and subsequent de-excitation results in the production of radiation (emission). This emission is known as the aurora or polar light [101]. The aurora is generally observed between 95-150 km altitudes in the polar region with high luminosity. The aurora can be a very useful tool to understand the atmosphere of other planets such as Mars, Venus, and Jupiter. The aurora is not a part of the present study so the detail description is not presented here.

The atmospheric species such as O, O_2, and N_2 etc. get excited by absorption of solar radiation of suitable wavelengths. These excited species upon subsequent de-excitation emit a photon at their characteristic wavelength. This emission of energy in the form of radiation is known as the airglow. Yntema et al. [102] reported the first experimental evidence of airglow emissions. Later on, many experimental techniques and theoretical models have been developed to study the airglow emissions. The first spectroscopic signature of airglow was interfered from the atomic oxygen greenline emission (557.7 nm) in aurora. Subsequently, a number of studies have been reported to examine the airglow emission. Airglow serves as a very important tool to understand the dynamics, chemistry, and the structure of the upper atmosphere [34, 103–117]. The effect of gravity waves and tides can be observed in the airglow, which is useful to study the diurnal and seasonal variation of Earth atmosphere [35, 37, 107, 118–122]. In addition to the above, airglow also provides the wealth of information about the global wind patterns [33, 35, 103, 113, 123]. The airglow is also used as a tracer for the noctilucent clouds [124].

The airglow emission is classified into three categories based on time of observation i.e., twilight airglow, night airglow, and the day airglow. The twilight airglow (twilightglow) is observed during the early morning or early evening when the Sun is below the horizon but visible from a higher altitude. This emission is weak and widespread, while the night airglow (nightglow) is observed when the entire atmosphere is dark after sunlit. The atomic oxygen greenline and redline airglow have been continuously observed in the twilightglow and nightglow [125,126]. The airglow occurring during the daytime is the most challenging emission to observe due to presence of direct and scattered sunlight. The observed intensity of nightglow emission is small compared to dayglow emission due to chemiluminescence process [101,127]. The dayglow emission mostly results from the atmospheric species such as H, N, O, O^+, and OH, N_2 and O_2 molecules. Table 1.4 lists some of the airglow emitting species and their characteristic wavelengths observed in the Earth's atmosphere.

Table 1.4: Atmospheric species and their corresponding airglow emissions.

Atmospheric species	Wavelength of Airglow Emissions (nm)
N_2	427.8
$N_2(C^3\Pi)$	337.1
NO(1-0)	215.0
$N(^2D)$	519.8-520.1
OI	**557.7**, 630.0, 636.4, 297.2
O^+	247.0, 732.0, 733.0
O_2	864.0
O_2(1-0) band	864.5
O_2(0-0) band	762.0
OH	632.9, 766.0
Na	**589.3**
Mg	279.6, 280.3
MgI	285.2
Ca^+	393.3-396.8
Fe	386.0

It is well known that meteoric ablation is responsible for the accumulation of metallic species such as Mg, Ca, Na, K, and Fe in the Earth atmosphere [26,27,128–130]. Among these species, metallic sodium layer found in mesospheric altitudes has been adequately studied due to its large scattering cross section. The neutral sodium is used as a tracer for chemical, thermal and dynamical states of the atmosphere in its altitude region. In addition to the above it is also used as a tracer for the tides, waves and thermal structure in the MLT region [31,32,123,131,132]. Recently, sodium airglow emission has also been used to study the noctilucent clouds [124]. In this thesis, we have studied the effect of space weather events on sodium airglow emission by using coordinated observation and modeling techniques.

1.7 Aim and objectives of the thesis

The Earth's atmosphere is dynamically coupled with the Sun and its energy. There are many different manifestations of this coupling on the neutral atmospheric and ionospheric phenomenon. The present thesis tries to understand a few important aspects such as airglow, radiative emissions, metallic airglow, equatorial ionization, and temperature anomaly and their variation during intense magnetically disturbed conditions.

The thermospheric heat budget is mainly maintained by the infrared radiative emissions by Nitric Oxide. This emission acts to radiate the excess heat during space weather events to space in order to maintain the temperature structure and thus is generally referred to as natural thermostat. We have performed a study based on satellite data and physics-based model to understand the cause and type of fluctuations induced in the heat radiated during severe space weather events and its possible connection with the neutral densities. This study has revealed several important aspects about the correlation of O/N_2 ratio with the NO radiative flux and hemispheric distribution of heat budget. A physics-based model has been successfully implemented to invert satellite measured flux to understand the response of neutral NO abundance during space weather events. This study reveals that the collisional excitation of NO with atomic oxygen is the most dominant process for the total cooling rate. In order to understand the cooling rate and its longitudinal and latitudinal variation, we have studied the satellite-based peak of NO VER over the Asian sector and correlated it with the climatological model based neutral abundances. This study had revealed a few very important aspects about the difference in equatorial and polar thermospheric heat budget. Mesosphere is a very important part of the Earth's atmosphere because of the large availability of metallic species such as sodium (Na). Understanding of Na layer provides a very useful tool for the study of atmospheric waves and dynamics. With the help of a physics-based model and Lidar measured Na densities, we have tried to understand the effect of extreme space weather events on the Na abundance and the resulting airglow. This study aims to correlate the well-established effects of space weather on Ozone using the Na airglow.

The equatorial phenomenon such as equatorial ionization anomaly and equatorial temperature anomaly are proven to be very sensitive to the space weather events. With the help of photochemical models for the atomic oxygen airglow emissions, we have tried to understand how space weather influences the parameters related to EIA and ETA and to provide a comprehensive understanding on the relation between neutral species and ionosphere for accounting the observed change in airglow intensity.

CHAPTER 2

STORM TIME VARIATION OF THERMOSPHERIC RADIATIVE COOLING

2.1 Introduction

Nitric oxide (NO) is an important trace species in the Earth's atmosphere. Although highly variable, it plays a valuable role in the MLT region due to its low ionization energy [133, 134]. Due to the lowest ionization potential among the major neutral constituents, NO acts as the terminal ion in charge exchange reactions and in certain important ion-molecule and ion-atom reactions [133]. The nitric oxide molecule, due to the above mentioned reasons, mainly responsible for ionization in D-region. Due to the presence of the IR-active vibrational modes NO plays a very important role

---

The results presented in this chapter have been reported in a research publication: Gaurav Bharti, M. V. Sunil Krishna, T. Bag, and Puneet Jain, Storm time variation of radiative cooling by nitric oxide as observed by TIMED/SABER and GUVI, J. Geophys. Res.: Space Phys., 123, 2, 1500-1514, 2018.

in establishing the lower thermospheric temperatures. The variation of NO density depends on latitude, longitude and season [135–138]. Auroral and geomagnetic activity influences the NO density in higher latitudes, whereas the compressional heating, molecular diffusion, and meridional transport from higher latitudes contribute to the variation in low latitudes [19, 137, 139]. In addition to the above, during geomagnetic storm conditions Joule heating and particle heating also contribute to the increase in nitric oxide density in polar latitudes [140, 141]. This heating results in the upwelling of nitrogen-rich/oxygen-poor air from lower to higher altitude. The meridional wind brings the polar oxygen-poor/nitrogen-rich air to mid latitudes even to low latitudes during severe geomagnetic storms resulting in the depletion of O/N_2 ratio in the high latitudes [23, 112, 139]. The variation in O/N_2 ratio also decides the nature of the storm by influencing the electron density [23]. It is due to the fact that the plasma in the F_2 layer peak is produced due to the photo-ionization and lost due to the ion-molecule exchange reaction if steady-state approximation is assumed. As a result, the atomic oxygen ion, and hence the electron density is related to O/N_2 ratio [23, 142]. During a geomagnetic storm, larger amounts of energy and particles are deposited in Earth's atmosphere altering its structure, composition, and dynamics. The storm energy is rapidly lost from atmosphere and heat balance occurs via infrared emissions [17, 22, 143–145]. The NO infrared emission at 5.3 μm is a dominating heat balance process in the atmosphere [146].

The NO emission results due to the vibrational-rotational band transition ($\Delta\nu$=1, Δ j=0, ±1).

$$\mathrm{NO}(X^2\Pi, \nu = 1) \rightarrow \mathrm{NO}(\mathrm{X}^2\Pi, \nu = 0) + h\nu(5.3\ \mu m) \tag{2.1}$$

The dominant source for the production of this emission is the collisional vibrational excitation of nitric oxide by the impact of atomic oxygen [146–148].

$$\mathrm{NO}(\nu = 0) + \mathrm{O} \xrightarrow{\alpha_1} \mathrm{NO}^*(\nu = 1) + \mathrm{O} \tag{2.2}$$

This vibrational transition (reaction 2.2) acts as an important cooling process in the altitude range of 110-300 km [149]. The cooling process is due to the conversion of kinetic energy into radiative energy which is subsequently released into the space and lower atmosphere [17,18]. The inelastic collision process (reaction 2.2) has a rate coefficient of 2.8×10^{-11} exp(-2700/T) cm^3 s^{-1} [150–152]. This temperature dependent rate coefficient is responsible for the difference in the peak altitude of NO(ν=0) density and NO cooling rate (CR) at 5.3 μm. The maximum enhancement in the NO density is found at about 105 km whereas the maximum emission rate is found in the altitude of 120-130 km [148, 149, 153, 154]. The impact of N_2 and O_2 also results in the excitation of NO [148, 150, 151, 153]. However, these excitation processes are not efficient in populating the vibrational levels [17, 149]. On the other hand, collision of O_2 with N(^{2}D,^{4}S) acts as a dominant source for the production of NO during auroral and geomagnetic activity periods [133, 149, 155].

$$\mathrm{N(^2D,^4S)} + \mathrm{O_2} \xrightarrow{\alpha_2} \mathrm{NO}(\nu) + \mathrm{O} \tag{2.3}$$

This reaction plays a very important role in allowing thermosphere to rapidly recover from the perturbation caused by geomagnetic storms.

The NO emission at 5.3 μm acts as natural thermostat in thermosphere by which heat and energy are efficiently lost to space and lower atmosphere [17, 156]. The radiative cooling accounts for the dissipation of nearly 80% of Joule heating and energy input during storm period [134, 157]. Consequently, the NO radiative flux acts as a potential candidate to understand thermospheric modulation due to space weather events. In this study, we report the variations of NO infrared radiative flux (W/m^2) exiting thermosphere and O/N_2 ratio during the super-storm events of November 7-12, 2004 in the northern hemisphere for thermospheric altitudes between 100 km and 250 km altitude as observed by TIMED-SABER and GUVI.

The NO emission rate is mostly influenced by the geomagnetic storm conditions. The variation of NO emission rate during geomagnetically active and quiet period is shown in Figure 2.1. The black curve in Figure 2.1 shows the SABER retrieved NO cooling rate (W/m^3) profile on a geomagnetically quiet day (November 6, 2004) at 03:03 UT for orbit 15774 over a mid geographic location (55°N, 180°E). The average Dst index for the quiet day was 6 nT. The red curve in Figure 2.1 shows the NO cooling rate profile during a disturbed day (November 10, 2004) for orbit 15834. Figure 2.1 shows that the radiative emission rate during a storm period in the lower thermosphere is larger by a few orders of magnitude over the quiet period.

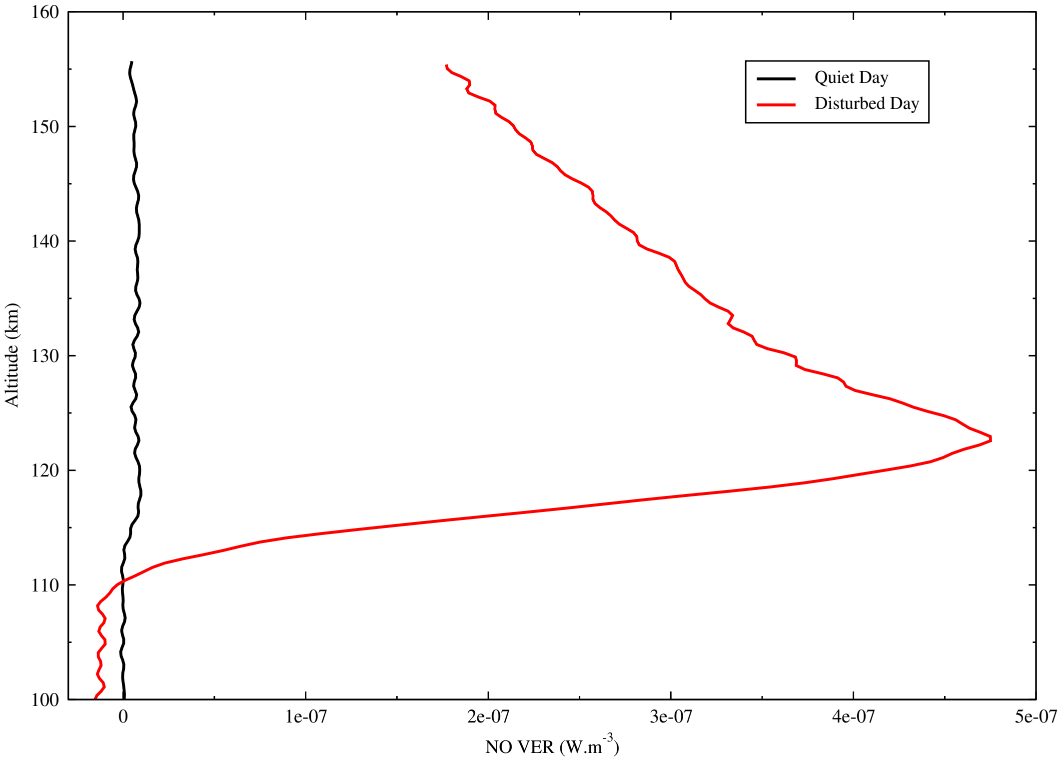

Figure 2.1: Volume Emission Rate profile observed by SABER on a quiet day, 6 November, 2004 for event 33, orbit number 15774 (a) and on a disturbed day, 10 November, 2004 for event 15 orbit number 15834 (b) over location (55.4°N, 180°E, Geographic) at 03:03 UT.

2.2 Methodology

The TIMED mission aims to study the basic structure and energy balance of the mesospheric and lower thermospheric altitude region [158]. NASA's TIMED satellite was launched on 7 December, 2001 into a 74 degree inclined orbit to understand the structure, chemistry, energetics as well the dynamics of the atmosphere [159]. It has four instruments on board: SABER (Sounding of Atmosphere by broadband emission of radiation), TIDI (TIMED Doppler Interferometer), GUVI (Global Ultraviolet Imager) and SEE (Solar Extreme Ultraviolet Experiment).

SABER is an infrared emission limb sounder. It covers Earth asymmetrically during any 60 days due to its anti-sun view [156,159]. It has 10 channels for observation of IR emissions ranging from 1.27 μm to 16.9 μm. SABER scans from 400 km to the surface of Earth and back upto 400 km measuring radiance (W$\cdot$ cm$^{-2}\cdot$ sr^{-1}) continuously with a vertical resolution of 2 km. These channels include the primary emissions from CO_2 and NO which are the most effective coolants in the atmosphere [158].

During the geomagnetic storm period reported here, the SABER was in a north viewing mode and covering latitudes between 83°N to 52°S. The Abel inversion technique is applied to SABER measured radiance profile to calculate the cooling rate [18,156,160]. The NO cooling rate (W/m^3) at 5.3 μm, from altitude ranges 100 to 250 km, are integrated to get radiative flux (W/m^2) exiting the thermosphere. To increase the availability of radiative flux at a given latitude and longitude, the data has been averaged to 10° latitude and 20° longitude bins.

The thermospheric O/N_2 data were obtained from TIMED GUVI, a spectrograph imager that measures Earth's far ultraviolet emissions to study atmospheric composition and auroral particle input [161,162]. These UV emissions include hydrogen's Lyman-α line, atomic oxygen lines (130.4, 135.6 nm), and N_2 Lyman-Birge-Hopfield (LBH) bands [158]. GUVI has a rotating mirror that scans Earth's limb and disc. The cross-track scanning provides FUV airglow every 15 seconds [112,161,162]. The images cover projected area of 2500 km$\times$100 km at 150 km altitude [112]. It works in both spectrographic mode and image mode. The Spectrographic mode is used to investigate the operation of instrument and consistency of the measured airglow in image mode. The O/N_2 ratio is derived using the intensity ratio of oxygen 135.6 nm and N_2 LBH emissions. The O/N_2 ratio is referenced to a N_2 column density of 10^{17} cm^{-2}. The fixing of N_2 column density to 10^{17} cm^{-2} minimizes the uncertainties of

O/N_2 ratio [112, 162]. We have used the thermospheric O/N_2 (referenced from an altitude 135 km (Level 3)) data for this study [23]. The O/N_2 data has been binned to 10° in latitudes and 20° in longitudes (similar to the NO cooling rate).

2.3 Model for Nitric Oxide abundance

The present study is aimed to understand the effect of severe geomagnetic storms on the NO radiative emission. As discussed earlier, the radiative emission intensity depends on the NO abundance. It would be very interesting to know how the NO abundance is modulated during the storm to produce the observed variation in the radiative flux. In order to establish a connection between observed variation in radiative flux and fluctuations in neutral densities we have developed a simple model in which the volume emission rate of NO is used to calculate the NO abundance. The nitric oxide radiative emission intensity mainly depends on three factors which are atomic oxygen, temperature and NO abundance. During the storm conditions, the decrease in [O] acts to reduce the NO cooling rate. It has been reported in earlier studies that oxygen atoms transfer energy between ν=0 and $\nu = 1$ vibrational levels to an order 10^3-10^5 times more efficiently than other neutral species [163]. The objective of this model is to approximately find the order to which the NO abundance must change to account for the observed change in NO radiative flux. Since no direct measurements of NO abundance are available during the storm period, this methodology can give us an idea about the severity of fluctuations induced in [NO] during the storm.

In addition to reactions (2.2 & 2.3), other minor sources for populating NO ($\nu = 1$) state are

(i) Resonant absorption of solar and terrestrial radiation at altitudes 80-110 km.

$$\mathrm{NO}(\nu = 0) + h\nu(5.3\mu m) \rightarrow \mathrm{NO}(\nu = 1) \tag{2.4}$$

The excitation rate due to solar radiation is given by $S = g_{S5.3}{\cdot}exp(-\tau{\cdot}Chp(\chi))$ (s^{-1}). Where Chp(χ) refers to Chapman function dependent on the solar zenith angle (χ). The fluorescence coefficient are measured to be 1.0×10^{-4} ($g_{S5.3}$) and 1.4×10^{-4} ($g_{T5.3}$) photon/sec per NO molecule for the solar and terrestrial radiation respectively [164].
(ii) Collision of NO molecules with electrons

$$\mathrm{NO}(\nu = 0) + \mathrm{e} \xrightarrow{\alpha_3} \mathrm{NO}(\nu = 1) + \mathrm{e} \tag{2.5}$$

The NO($\nu = 1$) thus produced from reactions (2.2, 2.3, 2.4, and 2.5) can also get deactivated by the following processes.
1. Collisional deactivation by third body

$$\mathrm{NO}(\nu = 1) + \mathrm{M} \xrightarrow{\beta_1} \mathrm{NO}(\nu = 0) \tag{2.6}$$

2. Ion-exchange reaction

$$\mathrm{NO} + \mathrm{O}_2^+ \xrightarrow{\beta_2} \mathrm{NO}^+ + \mathrm{O}_2 \tag{2.7}$$

The collisions of NO($\nu = 1$) molecules with other species have lower rate and hence have not been considered for the present calculation. In view of the above reactions, the cooling rate (C.R) due to 5.3 μm emission rate is given as

$$\mathrm{C.R.} = \frac{[\mathrm{NO}]\left\{\alpha_1 \cdot [\mathrm{O}] + \alpha_2 \cdot [\mathrm{N}] + \alpha_3 \cdot [\mathrm{e}] + \mathrm{S} + g_{T5.3}\right\}}{\left\{1 + \frac{\beta_1\cdot([\mathrm{O}]+[\mathrm{O_2}]+[\mathrm{N_2}])+\beta_2\cdot[\mathrm{O}_2^+]}{A_{5.3}}\right\}} \tag{2.8}$$

The values of reaction rate coefficients are summarized in Table 2.1. By using the vertically resolved profile of NO cooling rate in reaction 2.8, we can calculate the NO abundance. SABER observes emissions from the vibration-rotation bands of NO. As a diatomic molecule, NO has its fundamental mode of vibration (ν=1 to ν=0) centred at 5.3 μm. The SABER instrument is also sensitive to emissions from the 2-1 and 3-2 bands of NO [17]. Generally during the quiet nighttime conditions, the fundamental band of NO is the most dominant one. During the day and storm time, the higher lying bands may become slightly important. The SABER observations are suitably adjusted to indicate the total infrared emissions expected from ν=3,2,1 [156]. The neutral and ionospheric composition data used in this calculation have been obtained from NRLMSISE-00 [165] and IRI-12 [166] models.

Table 2.1: Reaction rate coefficients of Nitric Oxide radiative emission

S No.	Reaction rate coefficient	value	Reference
1	α_1	$4.2\times10^{-11}\cdot\exp(-2700/T)$	[150]
2	α_2	$1.1\times10^{-14}\cdot T\cdot\exp(-3150.T^{-1})$	[167]
3	α_3	$1.8\times10^{-10}\cdot(\frac{T_e}{1000})^{0.5}\cdot\exp\left(\frac{-2680}{T_e}\right)$	[167]
4	β_1	3.5×10^{-11}	[168]
5	β_2	4.4×10^{-10}	[164]
6	$A_{5.3}$	13.38	[164]
7	$g_{S5.3}$	1.0×10^{-4}	[164]
8	$g_{T5.3}$	1.4×10^{-4}	[164]

2.4 Results and Discussion

In the beginning of November 2004 two sunspot groups passed over the visible solar disk. These sunspot events resulted in solar flares and eruptive activity. Consequently, a geomagnetic storm occurred during 7-12 November, 2004 [169, 170]. The Dst index before the commencement of the storm indicated a quiet period. It was one of the strongest storms observed during space era. The interesting feature about this event is that two successive storms occurred during this period with the main phase of second storm developing on the background of first storm. Also, the storm has the unusually long lasting onset and main phases [169, 171].

The values of the Dst index and IMF B_z have been obtained from Space Physics Interactive Data Resource (SPIDR) and world data centre (WDC) for Geomagnetism, Kyoto, Japan. Figure 2.2(a & b) show the observed variation of B_z and Dst index

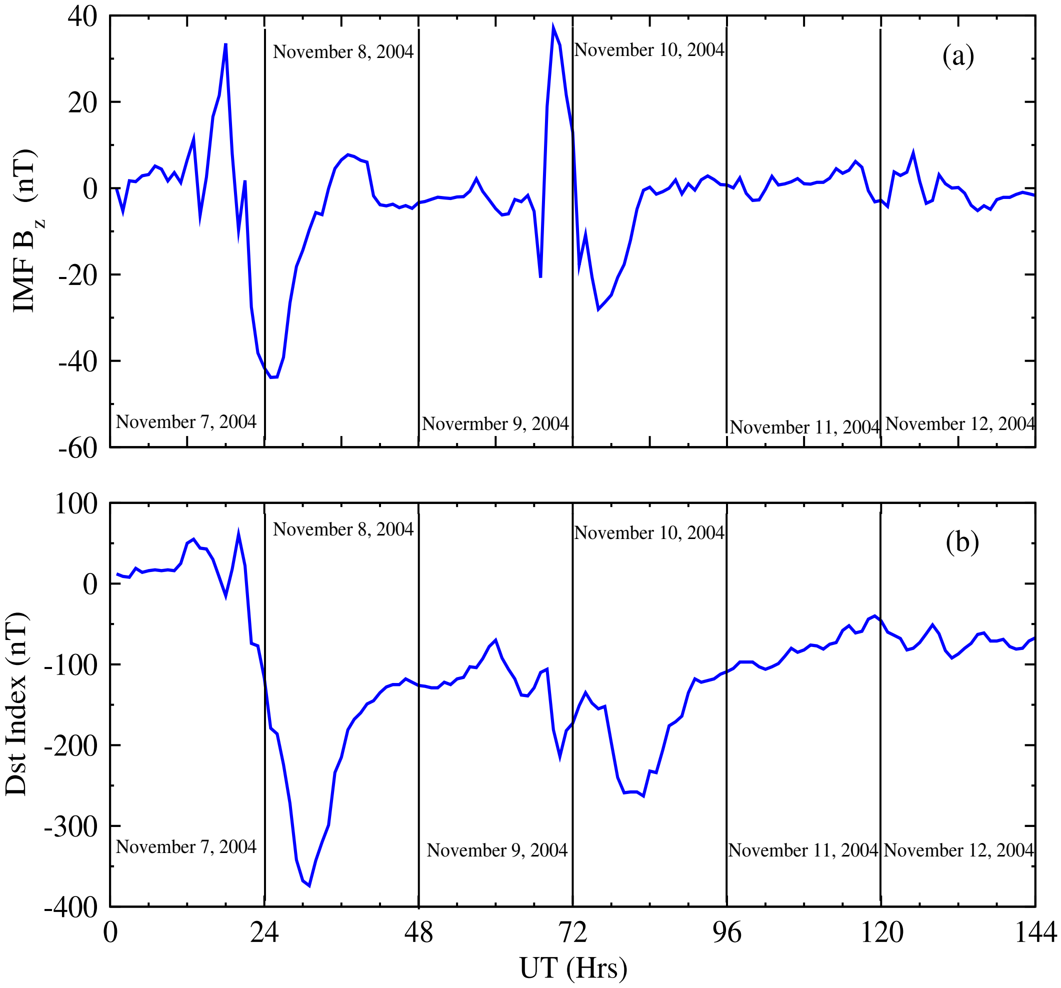

Figure 2.2: IMF B$_z$ (a) and Dst index (b) variation during the geomagnetic storm of 7-12 November, 2004.

respectively. It can be seen from this figure that the IMF B$_z$ turned southward at 21 UT on 7 November followed by a minimum Dst (-374 nT) occurring at 6 UT on 8 November (Storm1). As the storm starts to recede another super-storm (Storm2) occurs superimposing on the recovery phase of the first storm. The second storm occurs with a minimum Dst value of -265 nT on 10 November. The combined effect of this double storm was to modulate the state and structure of the atmosphere, which was peculiar and clearly different from a normal geomagnetic storm.

During a storm event the Joule heating and the particle heating change the atmospheric composition significantly in the high latitudes [23, 112, 135, 136, 142, 172]. The upwelling of equatorward neutral wind enriches higher latitudes with N_2 and depletes atomic oxygen density. The O/N_2 depleted air then moves towards the mid-low latitudes because of equatorward meridional wind [23, 172, 173].

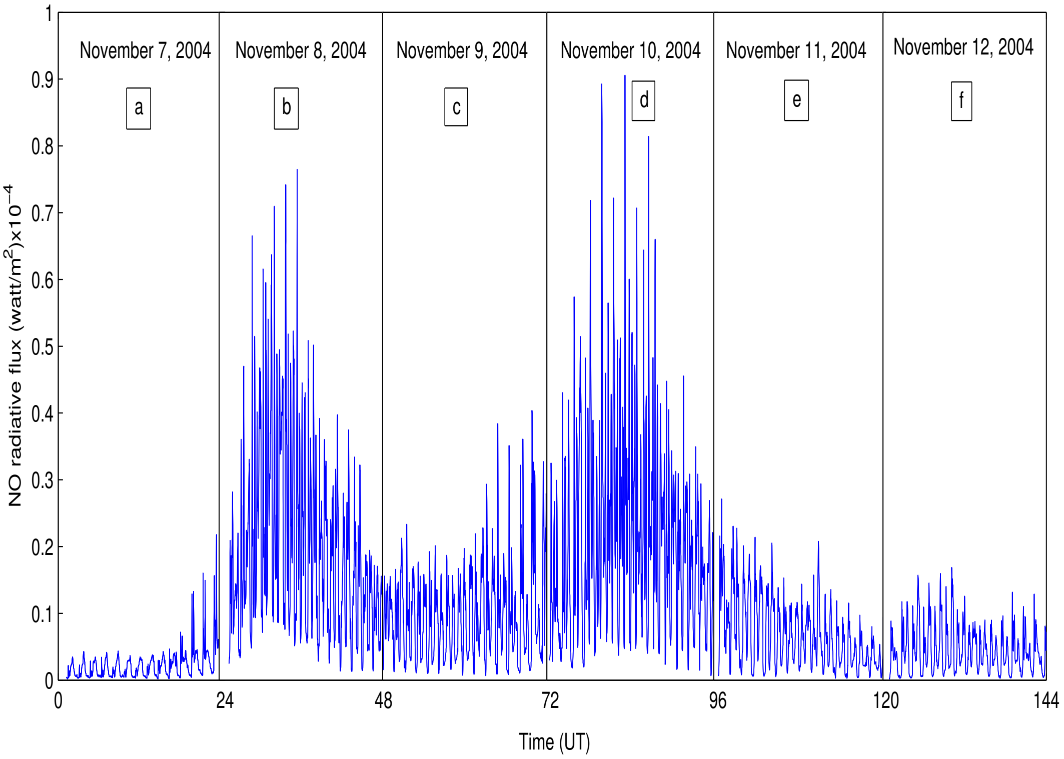

Figure 2.3: Vertically integrated radiative flux (W/m^2) as observed continuously by SABER during the entire storm period.

2.4.1 Storm time radiative flux & O/N_2

The variation of NO radiative flux during the entire double super-storm period is shown in Figure 2.3. The thermospheric radiative flux is the integrated cooling rate between 100 and 250 km altitude along the satellite path in north viewing mode. This gives the magnitude of flux exiting the thermosphere. The progression of the double storm is shown in Figure 2.2(b) for easy reference. It is noticeable from this figure that the thermospheric radiative flux undergoes a significant variation and shows a strong correlation with the progression of the storm. Figure 2.3(b) shows that the thermospheric flux increases significantly during the main phase of storm1. The large increase in the radiative flux could be due to polar Joule and particle heating, which subsequently moves the air along the pressure surface. The movement of air results in the depletion of O/N_2 [23, 173, 174]. By using the TIMED/GUVI retrieved O/N_2 and NO column density, Zhang et al. [23] have observed an anti-correlation between the O/N_2 and NO density on a global scale. As a result, it can be said that the depletion in O/N_2 ratio could have resulted in the enhancement of NO radiative flux. As the storm starts to recede the magnitude of radiative flux decreases. Figure 2.3 that the enhancement in NO radiative flux is relatively larger during the main phase of storm2 (10 November), although storm1 (-374 nT) is more severe compared to storm2 (-265 nT). This could be due to the fact that the second storm arrived before sufficient time had passed for the atmosphere to recover completely. As the storm starts to recover on November 11 the NO flux returns to the pre-onset conditions.

The densities of neutral as well as charged species are modulated during storm periods [23, 112, 175]. These variations in atmospheric species due to the Joule and particle heating in the polar region affect the O/N_2 which is negatively correlated with NO density [23, 112, 170, 173, 176, 177]. The observed variation in O/N_2 further decides the nature of storm (positive/negative) by influencing the electron density [23]. Generally, when the electron density increases as a result of storm dynamics, we call it a positive ionospheric storm and vice-versa. In the ionosphere, electron loss can be attributed to the dissociative recombination by N_2. In the present situation, O/N_2 depletion indicates Nitrogen-rich which increases the rate of recombination and hence reduces the electron density in the ionosphere. So the storm time availability or variation in electron density can also be attributed to fluctuations in O/N_2 ratio.

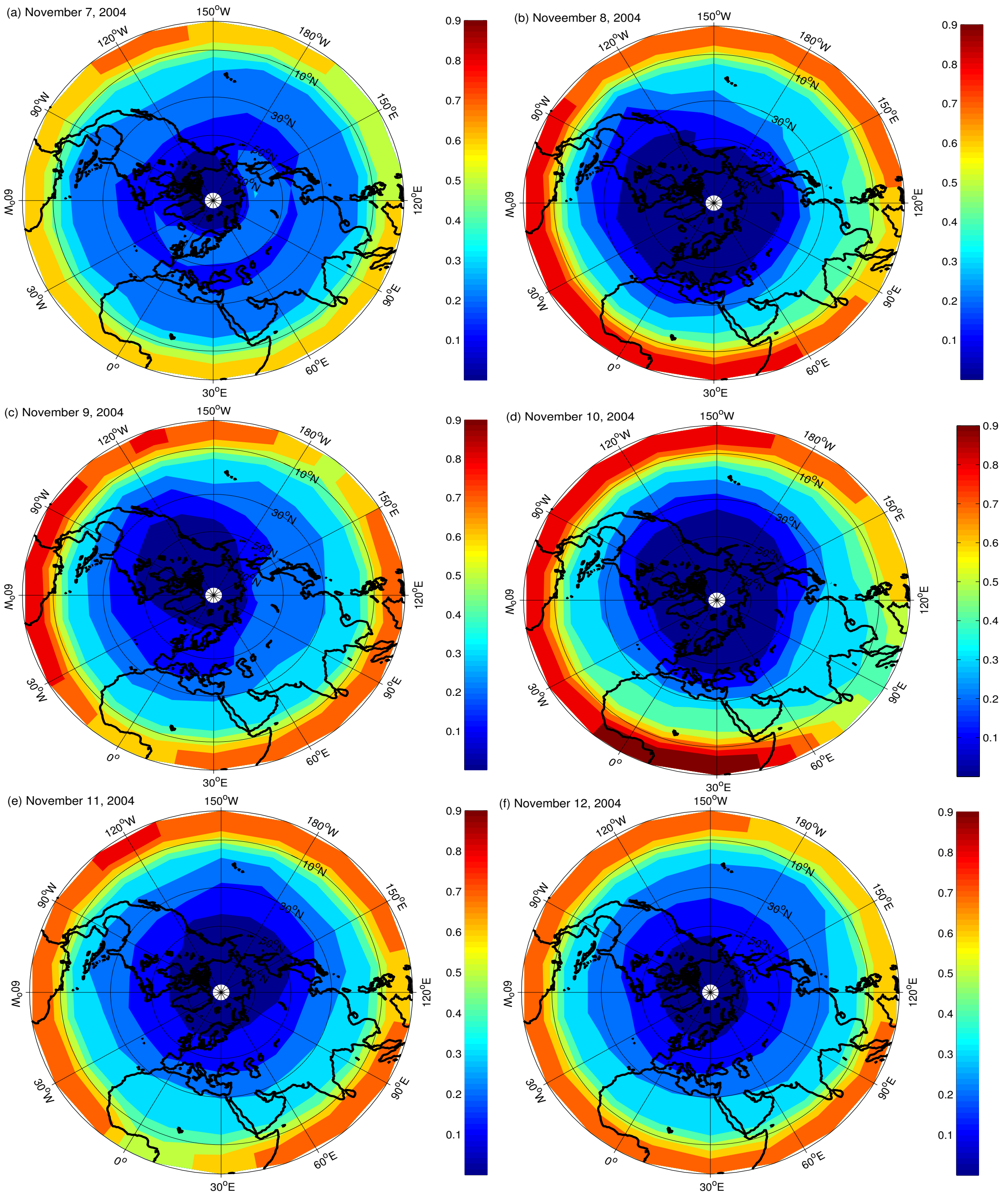

Figure 2.4: Daily O/N_2 variation during 7-12 November, 2004 at an altitude of 135 km as observed by GUVI.

The variation of O/N_2 ratio in the northern hemisphere during the entire storm period (7-12 November) is shown in Figure 2.4(a-f). We have used geographic coordinates in the present thesis. It is noticeable from Figure 2.4(a) that the ratio of O/N_2 is largest at the equatorial region with steady decrease towards the pole. During intense storm conditions, polar Joule heating becomes prominent and increases the temperature by hundreds of Kelvin in the upper thermosphere. This polar heating phenomenon causes a global effect by setting up large scale gravity waves or wind surge towards the equator. As a result, significant changes can be seen in the global circulation. The resulting meridional wind travels at nearly 400-1000 m/s [178]. The variations induced in O/N_2 ratio are also due to this meridional wind transport. The equatorward meridional wind brings oxygen-poor and nitrogen-rich air from high latitudes and deposits it at the mid and low latitudes [179]. This deposition results in the enhancement of O/N_2 ratio in the equatorial region during the main phase as can be seen in Figure 2.4(b). This deposition also results in the penetration of O/N_2 to lower latitudes. One important feature of this figure is that the surge of O/N_2 towards the equator is clearly seen in Figure 2.4(b & d) which actually represent the main phase of the storm. Further, it is also noticeable that the depleted O/N_2 shows a non-uniform distribution across the latitude and longitude. The depletion in O/N_2 is greater in western longitude sectors than what is seen in the eastern longitude sectors. This asymmetric distribution of O/N_2 could be due to the presence of the magnetic pole [137, 173]. As the storm starts to recede, the depletion in O/N_2 also starts to recover as shown in Figure 2.4(c). Figure 2.4(d) shows the variation of O/N_2 ratio during 10 November, 2004 i.e., the main phase of the storm2. It is important to note that depletion in O/N_2 at high latitudes ratio is greatest during 10 November although minimum Dst index (-265 nT) is lower than that on 8 November (-374 nT). This is similar to what has been observed with the integrated radiative flux (Figure 2.3). In the equatorial region, O/N_2 ratio enhances and reaches upto 0.9. The O/N_2 ratio starts to return to its pre-storm conditions as the storm recedes. This recovery to normal values is clearly visible in Figure 2.4(e & f).

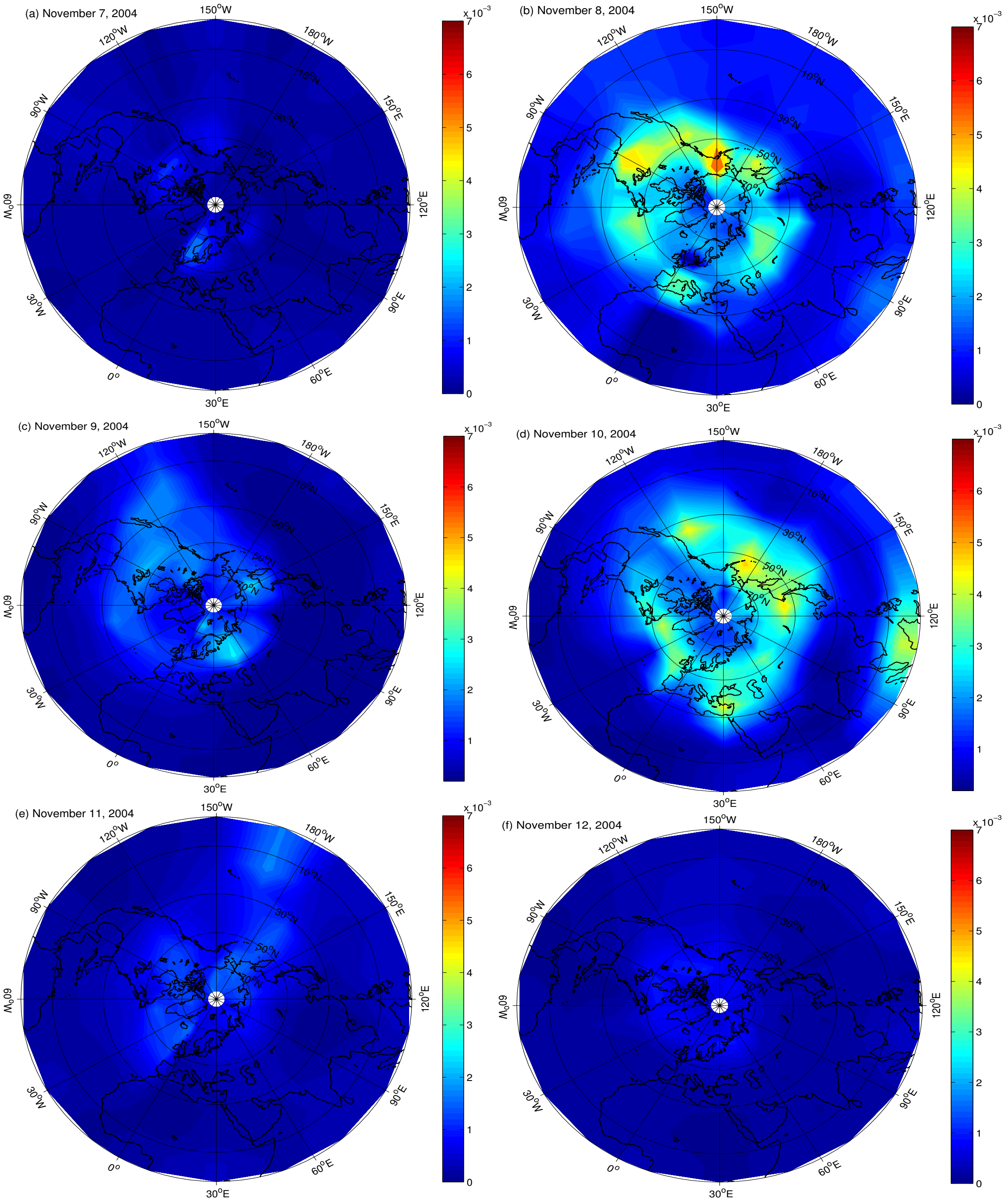

Figure 2.5: Daily Variation of integrated NO radiative flux (W/m^2) during 7-12 November, 2004 as observed by SABER.

2.4.2 Hemispheric variation of NO flux

The distribution of NO radiative flux exiting the thermosphere during the storm period is shown in Figure 2.5. The hemispheric distribution is shown for six consecutive days (a-f). Figure 2.5(a) marks the onset of the storm (7 November, 2004) whereas Figure 2.5(f) marks the recovery to pre-onset conditions (12 November, 2004). It can be seen from the figure that the radiative flux is almost uniformly distributed at the storm onset across the hemisphere except for small gulfs in the mid-high latitudes with slightly higher values. The radiative flux during the main phase of the storm (Figure 2.5(b)) shows very high values in mid to high latitudes across all longitudes. These observed values of high radiative flux can be understood as a combined effect of three different aspects explained below.

During the storm period, the equatorward meridional wind driven by Joule and particle heating in the polar latitudes brings O/N_2 depleted and NO enhanced air towards middle and low latitudes [23, 173, 174]. The storm effects are generally more prevalent in the higher altitudes. During the storm time, the increase of N_2 is responsible for the increased production of NO and decrease in the O/N_2 ratio. At the same time, thermospheric decrease in Oxygen also contributes towards the effective depletion in O/N_2 ratio. The storm-time O/N_2 depletion and enhancement in NO density are anti-correlated on a global scale. Due to this anti-correlation the enhanced NO density results in the net increase in the NO radiative flux exiting the thermosphere. A similar increase in radiative flux has also been reported in earlier studies [23]. During a geomagnetically disturbed period the high latitude ionosphere undergoes significant change in terms of temperature, density and composition. Among these parameters, thermospheric temperature increases significantly [174] affecting the NO flux because of the exponential dependence of NO density over temperature (reaction 2.2).

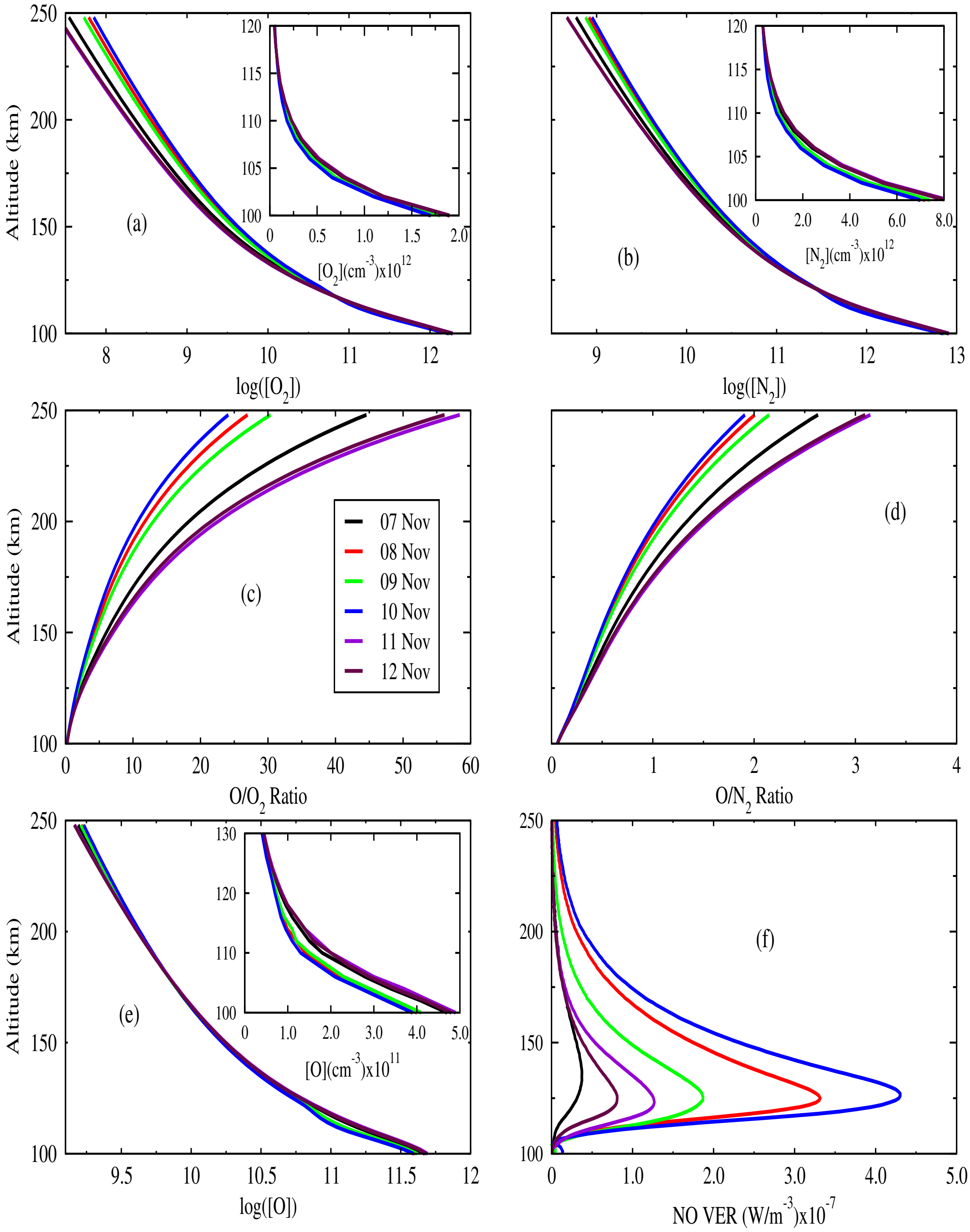

Figure 2.6: Altitude profiles of O_2 density (a), N_2 density (b), O/O_2 ratio (c), O/N_2 ratio (d), Atomic Oxygen density (e), and NO cooling rate as observed by SABER (f) during the entire storm period at a mid latitude (55°N, 180°E).

In addition to the changes induced in NO density due to meridional wind and thermospheric temperature, changes in neutral density become the third aspect influencing the NO density indirectly. The increase in neutral densities due to the onset of geomagnetic storm results in the enhanced production of [N] by dissociation of N_2 [149, 155]. From reaction (2.3) it is clear that the increased neutral density of O_2 and N_2 also contributes to the high rates of radiative flux. The maximum radiative flux is observed at mid to high latitudes in the high longitude sector (∼220-240°E) (Figure 2.5(b)). The radiative flux shows longitudinal asymmetry similar to variations seen in O/N_2 (Figure 2.4(b)) with more penetration to lower latitudes in western longitude sectors. This penetration can be attributed to the preference of wind surge to longitudes of magnetic pole and night side [137, 173].

The storm recedes on 9 November as IMF Bz turns northward (Figure 2.2). As a result the radiative flux also decreases from the high value during storm time. As seen from Figure 2.5(c) the radiative flux is low (shown in blue) globally except for small regions of slightly higher flux. From Figure 2.5(b & c) it is evident that the variation in radiative flux is very small in low latitudes. As the storm recedes, the atmosphere starts to return to its quiet time conditions. Interestingly, before the recovery is complete another super geomagnetic storm occurred on the recovery phase (Figure 2.2). The variation in flux during the second main phase on 10 November is shown in Figure 2.5 (d). From Figure 2.2(b) we can see that storm1 is stronger than strom2. The radiative flux during storm2 increases to very high values across all longitudes. It is worth mentioning that the percentage increase in radiative flux during storm2 is very high compared to storm1 although storm1 is more intense. This behaviour of NO radiative flux is also seen in integrated emission shown in Figure 2.3(b & d). The combined effect of storm2 overlapping on the background of storm1 is responsible for this change in the radiative flux. As the storm recovers (Figure 2.5(e & f)) the radiative flux decreases and returns to pre-onset conditions. It is well known that the neutral composition takes longer time to recover in the high latitude regions hence we see slightly higher values of radiative flux in high latitudes. In addition to this, the high latitudes also experience more energetic particle precipitation resulting in higher NO concentrations [20].

It is noticeable from Figure 2.4 that O/N_2 ratio depletes during the storm period with maximum depletion occurring during the main phase on 10 November. On the other hand, Figure 2.5 shows enhancement of radiative flux during the storm with maximum enhancement on November 8.The NO radiative flux is the integrated NO cooling rate for altitudes between 100 and 250 km. This difference in behaviour of O/N_2 ratio and NO radiative flux to storm could be due to the influence of geomagnetic storm and meridional wind which has more influence on higher altitude.

2.4.3 NO flux & neutral abundances

To understand the local variation of NO radiative flux under the effect of the double storm, we have tried to correlate variations in neutral densities (O, O_2, N_2) and density ratios (O/O_2 and O/N_2) with the NO cooling rate over a mid-latitude location (55°N, 180°E). The cooling rate profile has been obtained from SABER, and O, N_2 and O_2 densities have been taken from the NRLMSISE-00 model [165] at 6 UT. The local variations of NO cooling rate in combination with the densities and their ratios are shown in Figure 2.6. It is noticeable from Figure 2.6(a & b) that both O_2 and N_2 densities show similar variation under geomagnetic storm conditions. Below 120 km (shown in inlet), both O_2 and N_2 densities are depleted and above 120 km they show an increase under the main phase of geomagnetic storms. We have also calculated O/O_2 and O/N_2 ratios, which are shown in Figure 2.6(c & d), respectively. It is interesting to see that the modeled O/N_2 ratio (Figure 2.6(d)) shows similar variation as the O/N_2 ratio obtained from GUVI (Figure 2.4). The O/O_2 and O/N_2 ratios show depletion during the minimum Dst index. The maximum depletion in O/O_2 and O/N_2 ratios with respect to onset phase are about 80% and 50% respectively.

The altitude profile of modeled atomic oxygen density is shown in Figure 2.6(e). Here, it is important to note that the atomic oxygen density shows a depletion below

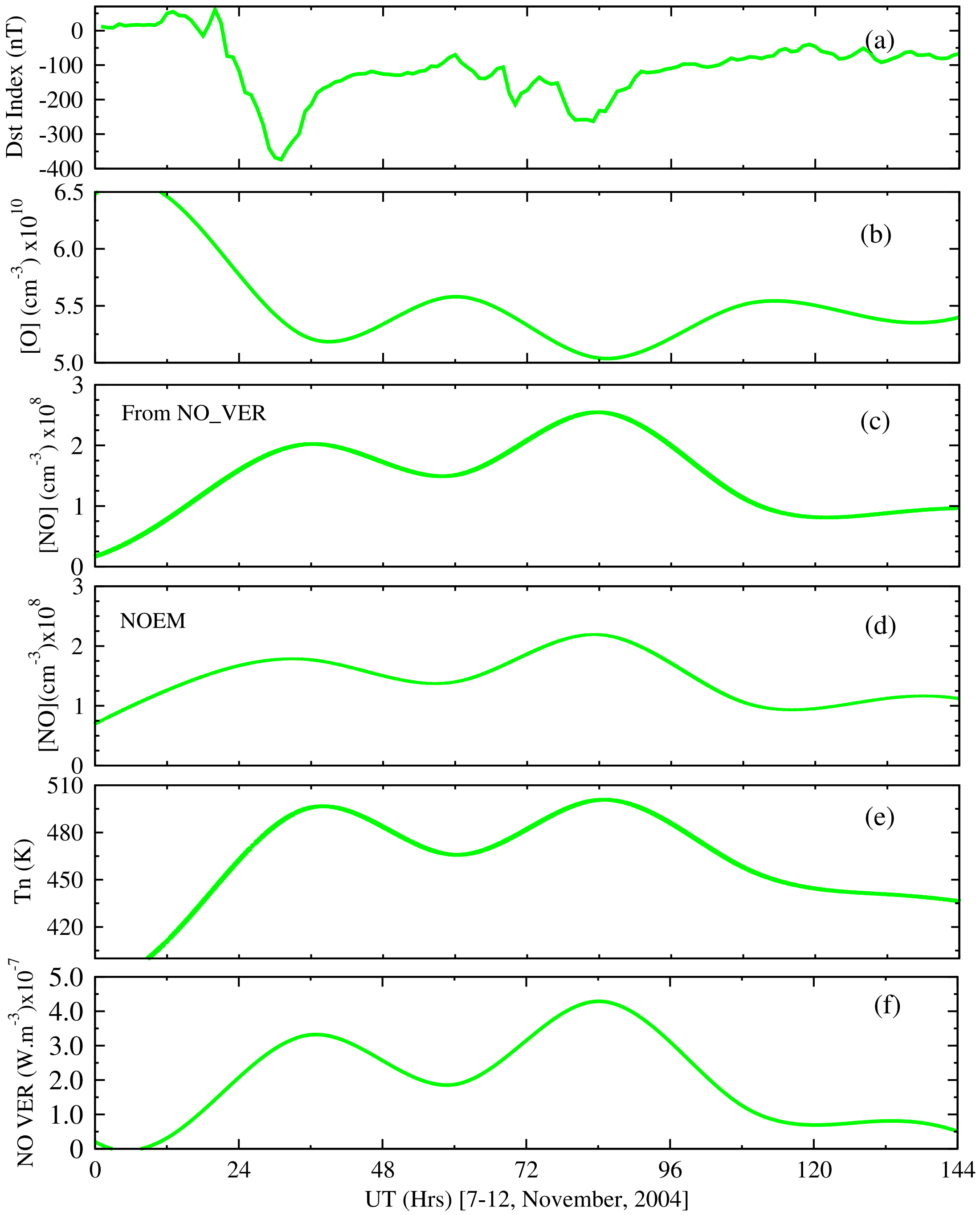

Figure 2.7: Summary plot indicating the correlation between Dst index (a), Atomic Oxygen density (b), and NO abundance from CR (c), NO abundance from NOEM (d), neutral temperature (e) and SABER observed cooling rate (f) during entire storm period at the peak emission altitude (125 km) and mid latitudes (55°N,180°E).

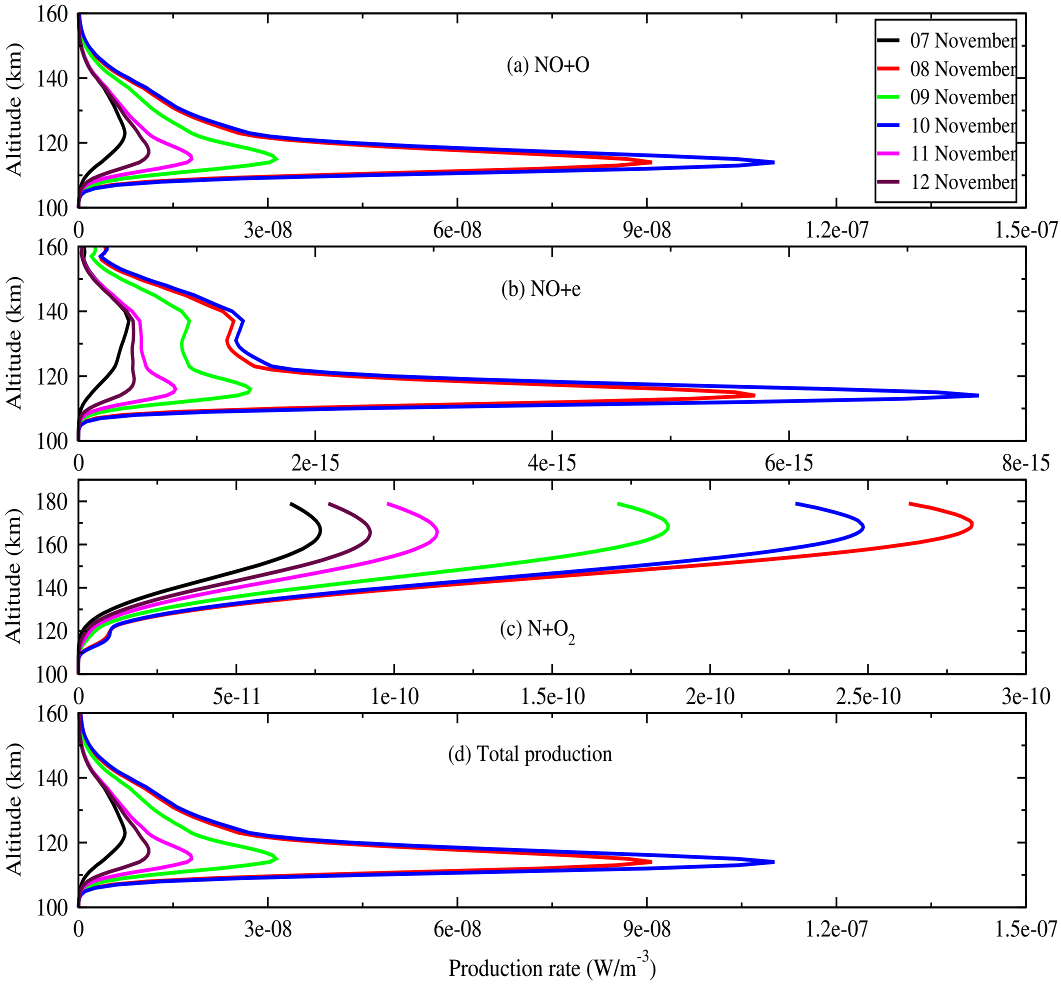

Figure 2.8: Excitation of NO(ν=1) by collisional excitation by O (a), electron excitation (b), collision of O_2 with N (c), and total NO(ν=1)(d).

160 km and enhancement above it [175]. The maximum depletion in atomic oxygen density below 160 km is observed on 10 November (storm2). Whereas, above 160 km the maximum enhancement is observed on 8 November (storm1). Since storm2 is happening on the background of storm1, it is natural to expect the effect of storm2 to be more pronounced. The maximum variation in density (O, O_2 and N_2) and ratio (O/O_2, O/N_2) are observed during 10 November. Similar depletion in O and O_2 densities below 120 km, during intense geomagnetic storms of August 2005 and April 2006, have also been reported by Bag et al. [175]. During storm periods, the O/N_2

ratio is anti-correlated to the NO density. So the production of NO from reaction (2.2) would be expected to increase. Similarly, both O_2 and N_2 densities enhancement would also result in the enhancement of NO cooling rate in accordance with reaction (2.3). Hence, the overall NO cooling rate increases during the storm period as shown in Figure 2.6(f). It is also noticeable from this figure that the maximum enhancement in NO cooling rate occurs during 10 November(storm2), although minimum Dst index is found on 8 November (storm1). Similar enhancements in NO cooling rate during storms have also been reported in literature [17, 21, 134, 144, 145]. Using data from SABER, Mlynczak et al. [17] have observed a factor of 5-7 increase in radiance between quiet and disturbed condition during 2002. Interestingly, the peak emission on NO VER shifts upward and downwards during the main and recovery phase of geomagnetic storm, respectively. The upward shifts of peak NO VER may be due the upwelling of air resulting from Joule heating and particle heating in polar region.

From the earlier discussion it is clear that the NO radiative emission mainly depends on three factors which are abundance of atomic oxygen, kinetic temperature and abundance of NO. From the SABER measurements we can establish how the radiative emission responds to the strong geomagnetic activity. Figure 2.7 shows the summarized results of variation in all these parameters at 125 km altitude during the entire storm period. From this figure, we can see how different number densities and emission rates respond to the geomagnetic storm. The observed variation in NO radiative flux must be a result of variation in the NO abundance. It will be interesting to know how the abundance of NO will correlate to the emission rate. In order to quantify the variation in NO abundance during the storm we have used two methods (1) By calculating the density of NO (ν=0) from the measured cooling rate (2) By calculating NO density using the NOEM model [153]. It is very important to explain the variation observed in emission rate with respect to decrease in [O], increase in [NO] and temperature. Figure 2.7(c) shows the calculated NO abundance using the scheme outlined before, and Figure 2.7(d) shows the same using NOEM model. Interestingly, both the methods suggest a multi fold increase in NO densities during the storm period. Both the methods listed above have predicted an increase in the NO abundance by 3-15 times. At the same time, the decrease in [O] should cause the CR to decrease. However, the decrease observed in atomic oxygen density (Figure 2.7(b)) is far too little to influence the total emission rate. So the relative competition between increase in [NO] and decrease in [O] decides the net increase in the radiative flux. From Figure 2.7(c & d), we can say that the increase in [NO] is more effective in the enhancement of total cooling rate. The third most important factor deciding the population of NO(ν=1) is the temperature. As can be seen from Figure 2.7 (e), the temperature will enhance the NO(ν=1) population, by means of the reaction rates listed in Table 2.1, during increased levels of geomagnetic activity.

The various sources contributing to the total NO(ν=1) as discussed earlier are shown in Figure 2.8. The collisional excitation of NO with atomic oxygen (Figure 2.8(a)) is the most dominant process for the total cooling rate. Other processes such as electron excitation (Figure 2.8(b)) and collision of O_2 with N (Figure 2.8(c)) do not contribute much to the total cooling rate (Figure 2.8(d)). We can notice from these figures that all the processes are identically influenced by the effect of geomagnetic storm. The increase of cooling rate can easily be correlated to the changes in neutral species and temperature.

It is clear from the discussions above that the geomagnetic storm will have a strong influence on the radiative cooling of thermosphere. The large amount of energy brought into the thermosphere is lost by the NO radiative emissions. This loss is evident interms of increased cooling rate. Both the methods discussed above conclude that the nitric oxide abundance undergoes a several fold increase during the main phase of the storm. In order to corroborate this we have identified three major geomagnetic storms during the observation period of Student Nitric Oxide Explorer (SNOE) (11 March, 1998 - 30 September, 2000). The SNOE database consists of measurements of nitric oxide abundance made using an ultraviolet spectrometer. The data covers 97-150 km altitude range and 80°S to 80°N, and 180°W to 180°E in the latitude and longitude range, respectively. For the sake of this study, we have

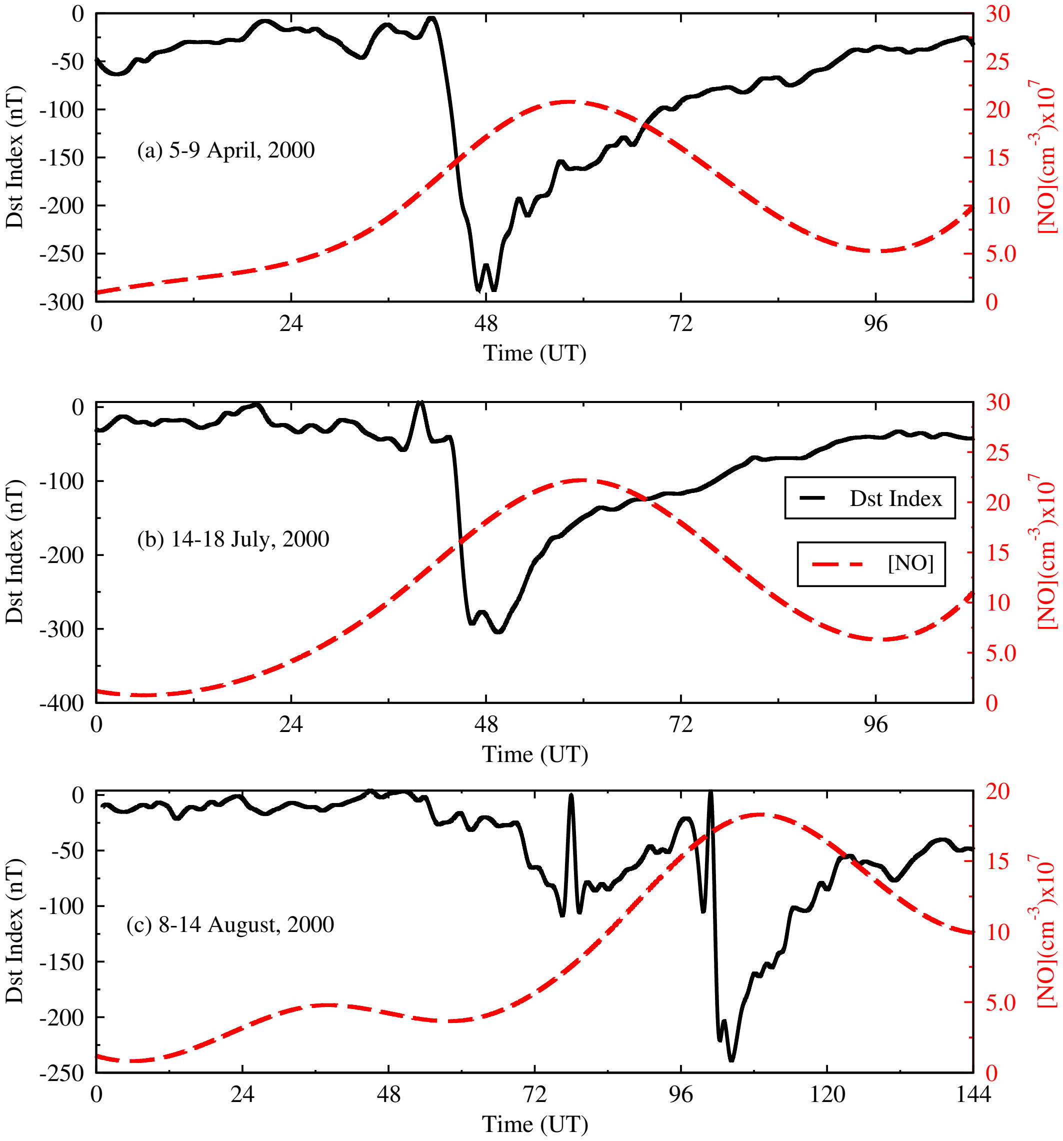

Figure 2.9: Variation of Dst index and NO abundance as observed from the SNOE during the geomagnetic storm, (a) during 5-9 April 2000, (b) 14-18 July, 2000 (c) 8-14 August, 2000.

considered the daily averaged NO abundance at about 100 km altitude and 65°N-75°N (Level 1). The three geomagnetic storms considered have the minimum Dst roughly of the same order as the double storm reported in this study. During these storms, NO abundances have been obtained from the SNOE database. Figure 2.9(a) exhibits the change in the [NO] during the storm of 5-9 April, 2000. It can be seen from the figure that the abundance of NO increases up to 8 times in comparison to the quiet time. Similarly the NO concentrations in Figure 2.9(b & c), indicating storms during 14-18 July, 2000 and 8-14 August, 2000, also suggest an increase in NO abundance by a factor of 11 and 9 respectively.

2.5 Conclusion

The northern hemispheric variation of O/N_2 ratio and Nitric Oxide radiative flux, exiting the thermosphere during the double super storm of 7-12 November, 2004 are studied using data from GUVI and SABER. On a global scale, O/N_2 ratio and NO flux are observed to be negatively correlated. The maximum depletion in O/N_2 ratio is observed during the main phase of geomagnetic storm2 on 10 November, Similarly on 10 November a maximum enhancement is found in the NO radiative flux. This difference in the behaviour of O/N_2 ratio and NO radiative flux may be due to the fact that the storm affects the higher altitude more compared to the lower altitude. Both O/N_2 and NO density were found to propagate equatorward due to the effect of meridional wind resulting from Joule and particle heating in polar region. A larger penetration of O/N_2 is observed in the western longitude sector. In the equatorial sectors, O/N_2 shows enhancements but almost no variation in NO radiative flux was observed. The maximum depletion and maximum enhancement for O, O_2 and N_2 densities and O/O_2 and O/N_2 ratios were found during the main phase of geomagnetic storm (10 November). The collisional excitation of NO with atomic oxygen is the most dominant process for the total cooling rate. The altitudes of peak emission rates are observed to shift upward during main phase of the storm. On both global and local scales, satellite retrieved NO radiative fluxes and O/N_2 ratios, as well as NRLMSISE-00 calculated densities, O/N_2, and O/O_2 ratios show correlation with the geomagnetic storm. The calculated NO abundances from the radiative flux and NOEM strongly suggest large (3-15 times) increase during the storm's onset. This increase is strong enough to counter the effect of decreasing atomic oxygen on the total thermospheric cooling rate. A Similar kind of enhancement in the NO abundance has also been observed by Student Nitric Oxide Explorer (1998-2000) during severe geomagnetic storm conditions.

CHAPTER 3

THERMOSPHERIC RADIATIVE COOLING OVER ASIAN SECTOR

3.1 Introduction

In the mesosphere and lower thermosphere (MLT) region, infrared emissions by carbon dioxide (CO_2) and Nitric Oxide (NO) molecules are the main agent for energy output. The MLT region receives input energy from the Sun and magnetosphere in the form of poynting flux and particle precipitation, as a result it heats up the atmosphere. This excess energy is released into the space by the infrared radiative emission produced by CO_2 and NO molecules. These molecules act as cooling agents in the MLT region. The radiative cooling below 130 km altitude is dominated by the CO_2 emission, while thermospheric cooling between 100-250 km is dominated by the NO emission. The maximum cooling is observed in the thermosphere due to NO radiative emission, which acts as a natural thermostat through which the energy

---

Part of the results presented in this chapter are reported as: Gaurav Bharti, Vir Singh, M. V. Sunil Krishna, Radiative cooling due to NO at 5.3 μm emission as observed by TIMED/SABER over Asian sector, revision submitted, J. Adv. Space. Res., 2018.

is lost into the space and lower thermosphere [17, 156]. The NO has low ionization energy and long chemical life time (1 day), as a result it is the main parameter to regulation of thermospheric temperature during the geomagnetic storms [180]. In addition to the above the vibrational excitation of NO produces IR radiation, which are responsible to cool the atmosphere. It has been observed that energy loss from NO emission is found to be more than 2000 Kelvin per day in the auroral region during the geomagnetic storm [18]. The radiative cooling due to CO_2 and NO emission depends on solar activity [181].

The NO plays an important role for understanding the composition of MLT region and the coupling between thermosphere and stratosphere [182]. The variation in NO density mainly depends on the latitude, longitude, altitude as well as seasons [138, 183, 184]. Barth et al. [139] have observed the enhancement in NO density during the winter and summer solstice. The fluctuations in the NO density at low latitudes is influenced by the Ultraviolet radiations and X rays [140, 185]. However, in the polar and mid latitude region, it is influenced by the Joule heating and particle heating which enhances kinetic temperature in the polar region [183, 186–188]. The neutral densities are also modulated by the geomagnetic storms. Therefore, the enhancement in the NO density at the higher latitudes is transported towards the mid and low latitudes. This resettlement in NO density is observed upto stratospheric altitudes [141, 189, 190]. It has been also found that compressional heating, meridional wind and molecular diffusion also contribute to transport of NO from higher latitudes towards lower latitudes [19, 139, 183]. The NO also acts as a catalyst in the stratosphere and destroys the Ozone [191, 192]. Barth et al. [19] have reported the maximum enhancement in NO density between 60-70 degree N latitude due to electrons precipitation near 110 km altitude in the northern hemisphere.

The solar ultraviolet radiation flux is the dominating source of heating during minimum geomagnetic activity. However, in the case of high geomagnetic activity the Joule heating and particle heating become main sources of thermospheric heating [193]. The Joule heating and particle heating are responsible for redistribution of depleted oxygen or enhance nitrogen air from lower thermosphere to the F region during geomagnetic storm [23, 112, 172, 175, 194–196]. This heating also accounts for increase in equatorward neutral winds which redistribute the enhance nitrogen/depleted oxygen air from higher latitude towards the lower latitude region. It has also been found that during geomagnetic storm the zonal wind increases at mid latitude due to Coriolis effect [179].

The excess energy in the MLT region provided by geomagnetic storm is rapidly lost from the atmosphere and heat balance occurs by infrared emissions [17, 22, 144, 145]. The fundamental vibration-rotation band emission ($\Delta\nu$=1, Δj=0, $\pm$1) of NO at wave length 5.3 μm is one of the important source in the MLT region through which radiative cooling takes place [146].

$$\mathrm{NO}(\mathrm{X}^2\Pi, \nu = 1) \rightarrow \mathrm{NO}(\mathrm{X}^2\Pi, \nu = 0) + h\nu(5.3\ \mu m) \tag{3.1}$$

The dominating source of production NO(ν=1) is the collision between NO molecules and atomic oxygen [24, 146–148].

$$\mathrm{NO}(\nu = 0) + \mathrm{O} \rightarrow \mathrm{NO}(\nu = 1) + \mathrm{O} \tag{3.2}$$

The reaction (3.2) is the dominant source for the production of NO(ν=1) in the altitude range 110-300 km [17, 18, 24, 197]. The rate coefficient for this reaction is 4.2×10^{-11} exp(-2700 $\cdot$ T^{-1}) ($\mathrm{cm}^3 \cdot \mathrm{sec}^{-1}$) [152, 154]. The maximum radiative cooling is found around 120-135 km altitude, while peak NO density is found around 105 km altitude. This altitude difference may be due to the exponentially temperature dependence of rate coefficient of reaction (3.2) [148, 149, 153, 154]. The variation in the NO emission shows linear dependence with atomic oxygen number density ([O]) and NO number density. However, it is non-linear with respect to temperature. The other possible sources for production of vibrationally excited NO molecules are the inelastic collisions of O_2 and N_2 with NO (ν=0) molecules. However, the contributions from these processes are much smaller than the reaction (3.2) [163]. Consequently, the reaction (3.2) can be considered as an important source for the production of NO excited molecules.

The following exothermic reactions may also be the main sources for production of exited NO^* in the vibration-rotational state.

$$\mathrm{N}(^4\mathrm{S}) + \mathrm{O}_2 \rightarrow \mathrm{NO}(\nu, j) + \mathrm{O} \tag{3.3}$$

$$\mathrm{N}(^2\mathrm{D}) + \mathrm{O}_2 \rightarrow \mathrm{NO}(\nu, j) + \mathrm{O} \tag{3.4}$$

The collision of O_2 with $N(^2D,^4S)$ is the dominant source for the production of NO^* (ν) during auroral and geomagnetic storm conditions [133, 155]. This process is more important during daytime than night time because the production of $N(^2D)$ during day time is higher than the night time [147].

In the light of above discussion, it is important to study the peak emission of NO VER and corresponding variation in the atomic oxygen number density during the geomagnetic storm. In the present study we have chosen the Asian sector to examine the response of peak emission of NO VER and corresponding atomic atomic oxygen number density during the storm. We have considered the Asian sector due to presence of mid to equator region (0°-60°N), and to understand the longitudinal and latitudinal variation, coincidentally no study has been reported on this sector using SABER observations.

3.2 Objective of the study

NASA TIMED (Thermosphere Ionosphere Mesosphere Energetic Dynamics) satellite was launched in circular orbit around the Earth on 7 December 2001. The TIMED satellite has four payloads namely SABER (Sounding of the Atmosphere using Broadband Emission Radiometer), TIDI (TIMED Doppler Interferometer), GUVI (Global Ultraviolet Imager) and SEE (Solar Ultraviolet Experiment). The TIMED is a polar satellite. SABER views the earth asymmetrically during any 60 days due to its anti-sun view [156, 159, 198]. This is the first mission to study the global variation of MLTI regions.

The SABER scans from 400 km tangent height to the surface and back up 400 km measuring radiance continuously. The time taken for a single scan is 53 second and within this time SABER travels about 350 km in the orbit. The SABER measures continuously the emitted radiation of NO and CO_2 (W. cm^{-2}. sr^{-1}) with vertical resolution of 2 km. The detailed description of the SABER instrument is given by Russel et al. [159]. Abel inversion technique is applied to SABER measured radiance to calculate the cooling rate [18, 156].

3.3 Methodology

In this study, we have analysed the latitudinal and longitudinal variation of peak NO VER at 5.3 μm and corresponding atomic oxygen number density over the Asian sector. The Asian sector is considered between latitude 0°-60°N, and longitude 40°-160°E. The Asian sector has been divided into bin sizes of 10° latitude and 20° longitude. In each bin, on average the satellite revolves around 2-4 times, and corresponding to each orbit we have noted the peak emission of NO VER (cooling rate) and corresponding altitude. In each bin we have on average 2-4 data points corresponding to NO VER, we averaged the data points in each bin. Therefore, corresponding to each bin we have one data point for NO VER. At the same altitude and time we have calculated the [O] by suing NRLMSISE-00 model.

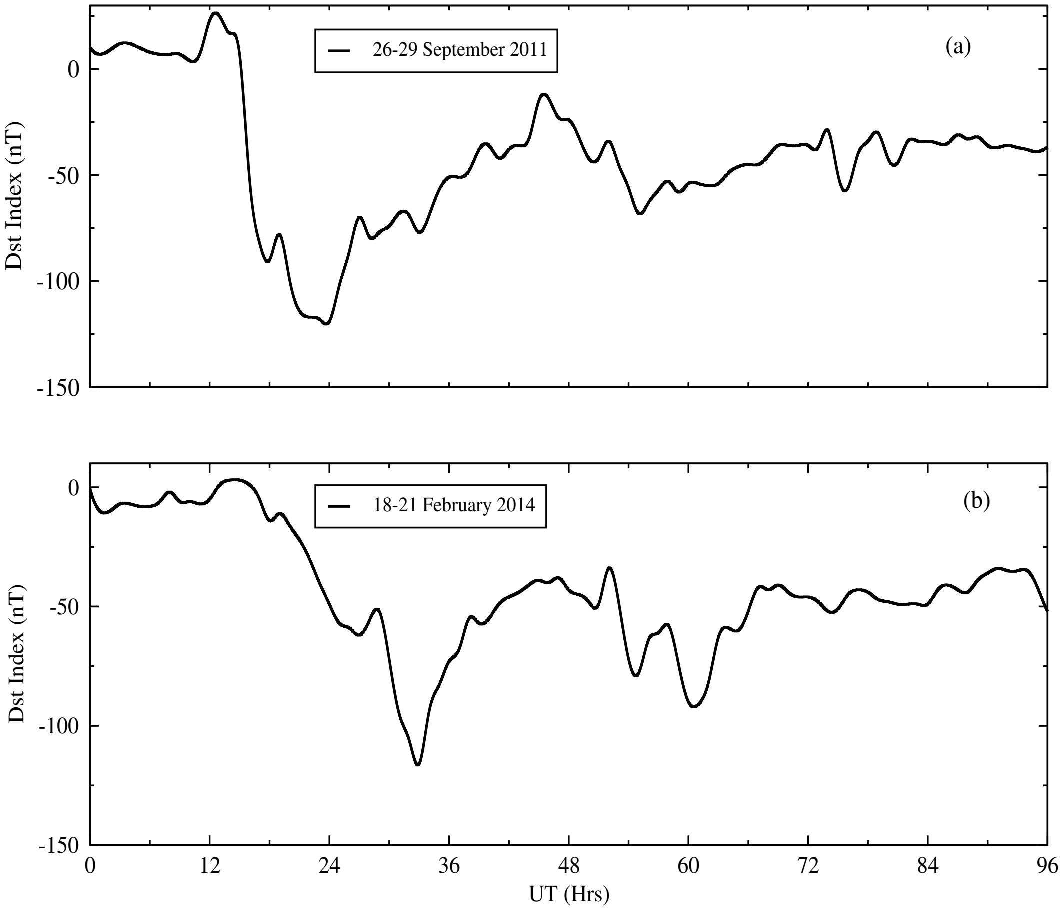

Figure 3.1: Variation of Dst Index (a) 26-30 September 2011 (b)18-21 February 2014

3.4 Result & Discussion

Figure 3.1(a & b) show the variation of observed Dst index during the geomagnetic storm 26-29 September 2011 (storm1) and 18-21 February 2014 (storm2), respectively. The data for Dst index has been obtained from the Word Data Center (WDC) for Geomagnetism, Kyoto, Japan. Figure 3.1(a) shows sudden commencement of storm at 11 UT on 26 September 2011 and reaches in main phase very quickly at around 1 UT on 27 September 2011 with a minimum Dst index of -118 nT. Figure 3.1(b) shows another storm which commenced at 12 UT on 18 February 2014 with minimum Dst index -116 nT at 9 UT on 19 February 2014. This storm superimposed with another storm Dst index of -90 nT on 20 February 2014 at 12 UT. The combined effect of these storms on peak emission of NO VER and corresponding atomic oxygen number density [O] is studied over Asian sector.

3.4.1 Longitudinal variation of peak NO VER and corresponding atomic oxygen number density during storm1

The longitudinal variation of peak NO VER at 5.3 μm, and corresponding [O] during the storm1 (26-29 September 2011) are presented in Figures (3.2 & 3.3) over Asian sector respectively.

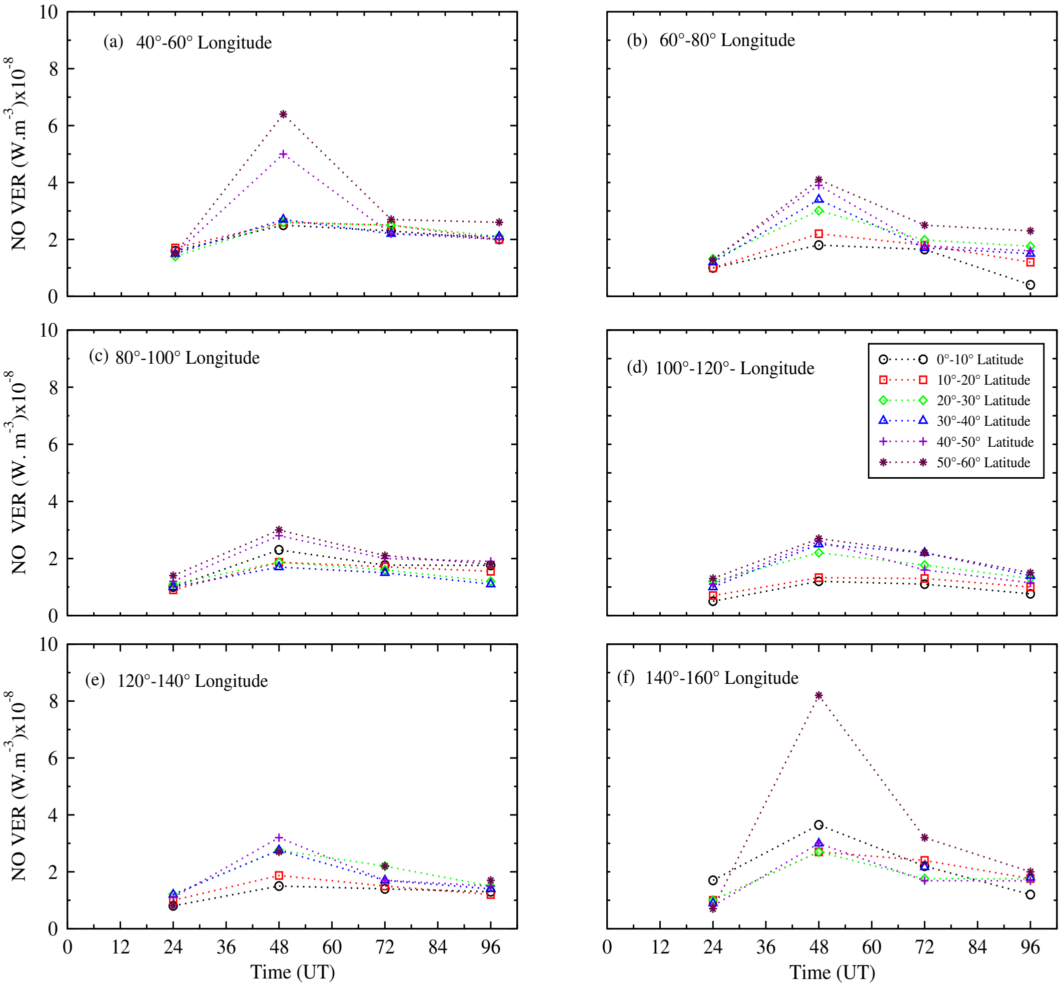

Figure 3.2: Longitudinal variation of peak NO VER during 26-29 September, 2011 (storm1)

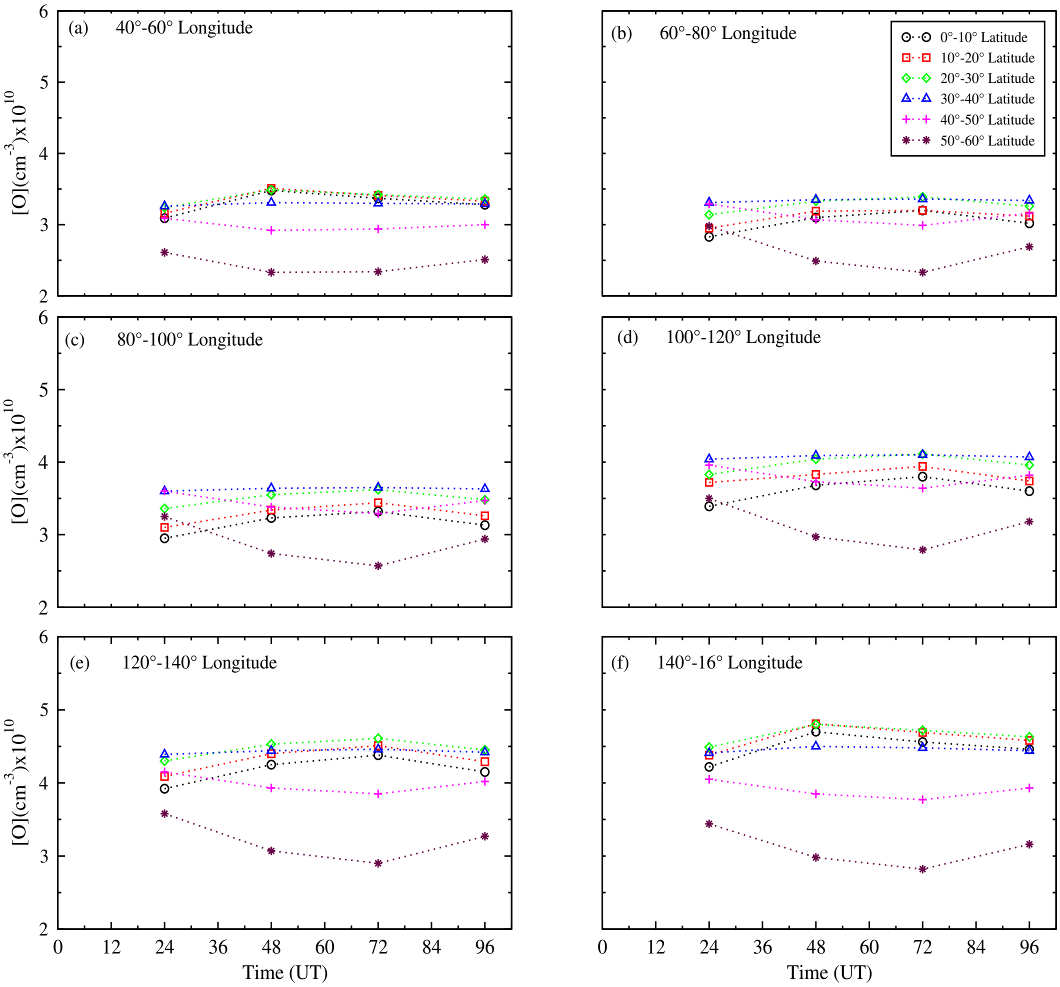

Figure 3.3: Longitudinal variation of [O] corresponding to peak emission of NO VER during storm1

Figure 3.2 shows the longitudinal variation of peak NO VER between latitudes 0°-60°N with 10 degree latitudinal interval. The panel (a) of Figure 3.2 shows the longitudinal (40°-60°E) variation of cooling rate between latitude range 0°-60°N. This panel shows that during the main phase (27 September 2011) of storm cooling rate increases over all latitudes. However, the maximum enhancement in the cooling rate is found between 50°-60°N latitude. Panel (b) of Figure 3.2 also shows the similar kind of variation as found in panel (a), however the magnitude of peak NO VER is quite low compare to panel (a), However the maximum enhancement in the peak of NO VER is found between latitudes 50°-60°N. Panel (b) also shows that there is a slightly difference in magnitude of peak NO VER between latitudes 50°-60°, 40°-50°, and 30°-40°N as compared to panel (a) of Figure 3.2. Panel (c & d) also shows the enhancement in the peak of NO VER during the main phase of storm over all latitudes. However, the difference in the peak of NO VER over all latitudes decreasing as compared to panel (a & b). Panel (e) also shows the similar variation as seen in the panels (a-d) except that the maximum enhancement in the peak of NO VER is found between latitude 40°-50°N. The enhancement in the peak of NO VER within latitude range 40°-50°N of panel (e) could be due to large penetration of NO abundance in this latitude during the main phase of the storm. During geomagnetic storm Joule heating and particle heating at the polar region setting up large-scale gravity waves or wind surge towards the equator. The equator-ward meridional wind brings depleted-oxygen or rich-nitrogen as well as enhance NO air form higher latitude and deposits it at the mid and low latitudes [179]. This deposition also results in the penetration of enhanced NO air towards the mid and low latitudes. However, this deposition is an asymmetric distribution due to presence of magnetic pole [137, 173]. Panel (f) shows the similar variation as found in panels (a-e). The maximum growth is observed between latitude 50°-60°N on 27th September. The maximum progression in the peak of NO VER is found between longitude 40°-60°N (panel a) and 140°-160°N (panel b) during the main phase of the storm. The enhancement in the peak emission of NO VER within longitude 40°-60°N, and 140°-160°N could be due to more penetration of NO enhance air during the main phase of storm. The similar type of enhancement in the cooling rate have been reported in the literature [17, 21, 134, 144, 145, 199]. The enhancement in the cooling rate can be explained in the following ways.

The variation of infrared radiative cooling due to NO at 5.3 μm emission mainly depends on the three factors i.e., NO abundance, atomic oxygen abundance and thermospheric temperature. It has been found that during the severe geomagnetic storm the above factors shows the significant variation. The enhancement in the NO density is increased about 3-15 times, and the thermospheric temperature also significant enhance during the storm time [24, 174, 200]. This enhancement in the NO density at the polar region is due to Joule heating and particles heating. However, the atomic oxygen number density shows a depletion at the polar region, while at the mid-low latitude enhancement is found [175, 200]. In addition to the above, cooling rate also depends on the abundance of nitrogen atoms and molecular oxygen as seen in the reaction (3.3 & 3.4). The energetic electrons, both auroral and photoelectrons produce the atomic nitrogen in the MLT region by ionizing and dissociation of N_2 molecules during the storm [149, 155]. The cooling rate due to reactions (3.3 & 3.4) increase at the higher latitudes. Therefore, the maximum enhancement in the peak of NO VER is found at the higher latitudes.

As the storm recovers, the atmospheric species starts to return to it's pre onset value. Panels (a-f) of Figure 3.2 show that during the recovery time of storm, peak emission of NO VER is decreasing. However, at higher latitudes (50°-60°N) peak emission of NO VER still remains higher as compared to mid and low latitudes. This difference could be due to time scale of thermospheric neutral density in other words at the higher latitudes atmospheric species take longer time to return to its pre onset value as compared to mid-low latitudes [201]. At the polar region the effective chemical life time of NO is about 1 day [134, 202]. Therefore, we observe the relative higher emission of NO VER at mid latitudes compare to equator during the recovery phase of the storm. It would be important to mention that, the peak emission of NO VER is strongly correlated with the elongation of the storm (Figure 3.1).

The corresponding climatological longitudinal variation of the atomic oxygen number density over Asian sector between longitude 40°-160°E is shown in the Figure 3.3. Panel (a) shows the longitudinal variation of [O] corresponding to peak altitude of NO VER, between latitudes 0°-60°N. This panel shows that the higher values of the atomic oxygen number density is found near equator, while at the higher latitudes depletion is found during the main phase of the storm. The similar type of variation in the [O] is also observed in the panels (a-f) of Figure 3.4 during the main phase of the storm. However, the maximum enhancement in the atomic oxygen number density is found between latitude 20°-30°N as shown in the panels (a-f). The atomic oxygen number density is observed at the peak altitude emission of NO VER which varying from 120-135 km. Therefore, this variation in the atomic oxygen number density could be altitude dependent. In addition to the above, it is also noticeable that the maximum depletion is found between latitudes 50°-60°N (panels (a-f)). The depletion in the atomic oxygen number density at the higher latitudes could be due to equatorward meridional wind which brings the atomic oxygen from the higher latitudes thereby depositing it at the low and mid latitudes [23,173,200]. This deposition results in the enhancement of the atomic oxygen number density in the mid-low latitudes as shown in panels (a-f) of Figure 3.3. It is well known that the neutral densities take longer time to recover at the higher latitudes [201]. It is evident from Figure 3.3 that there is a positive correlation between atomic oxygen number density and peak emission of NO VER below 40 degree latitude during the main phase of the storm. However, there is a negative correlation between peak emission of NO VER (Figure 3.2) and [O] between 50°-60°N latitudes (panels (a-f) of Figure 3.3). It is worthwhile to mention here that the cooling rate is more at higher latitudes than the mid and low latitudes [199]. Figure 3.3(f) shows that the variation of [O] is higher compared to panels (a-e) over all latitudes. This could be due to more penetration of the atomic oxygen number density in this longitude sector (140°-160°E (panel f)). As the storm recedes the atomic oxygen number density returns to its pre-onset value (panels (a-f) in Figure 3.3) during the recovery phase of the storm.

Interestingly, it is noticeable that during the severe geomagnetic storm conditions the NO abundance and thermospheric temperature show the significant enhancement. On the other hand, the [O] shows the enhancement at the equator region and depletion towards the higher latitudes. The maximum enhancement in the peak of NO VER is found at the higher latitudes. At the same time, [O] causes to decrease the peak emission of NO VER at the higher latitudes. The relative competition between increased NO abundance and decreased [O] decides the net enhancement in the peak emission of NO VER. However, it is evident that NO abundance shows a large enhancement (around 3-15 times) during the storm time, while the atomic oxygen number density shows small variation compared to NO abundance. Therefore, the NO abundance is the dominant factor to influence the peak emission of NO VER during the storm at the higher latitudes. In addition to the above, the third most important factor which influences the peak emission of NO VER is the thermospheric temperature as seen in reaction rate coefficient of reaction (3.1).

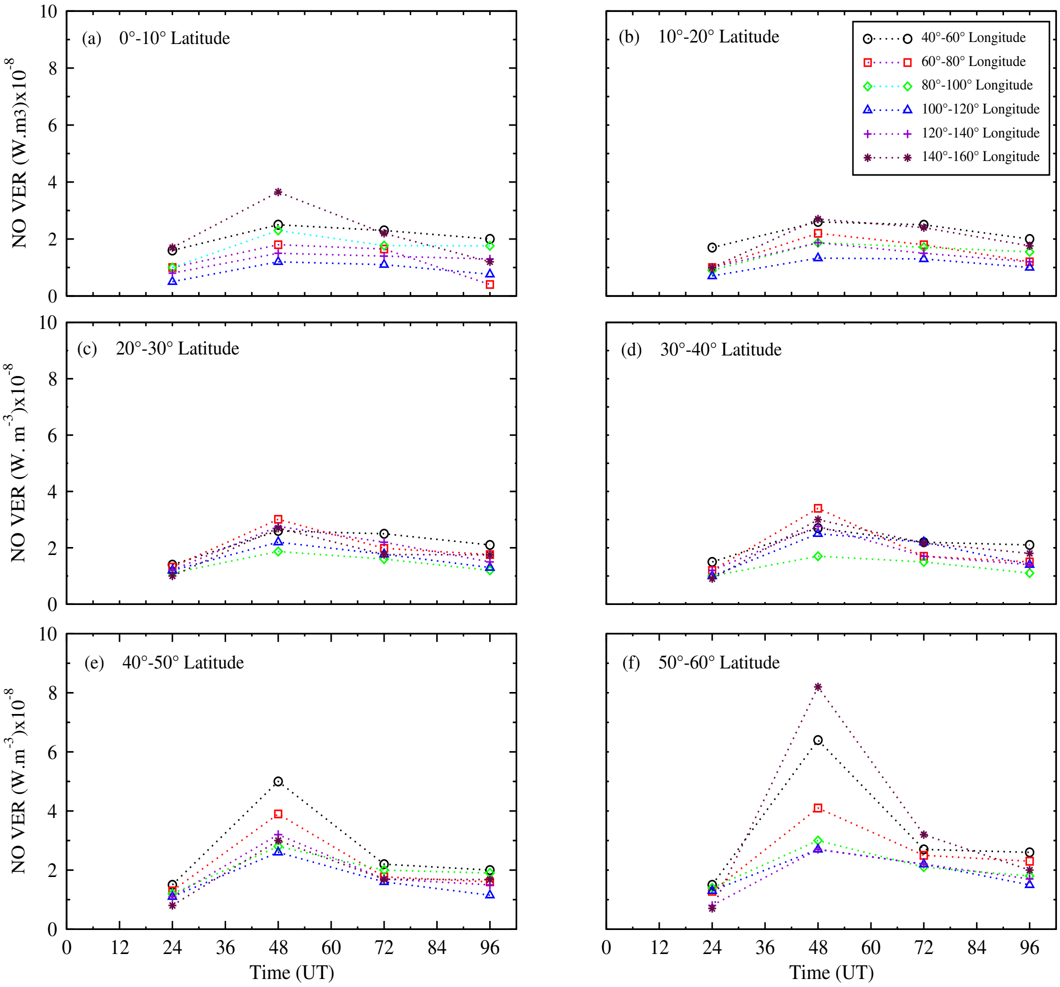

Figure 3.4: Latitudinal variation of peak NO VER during storm1

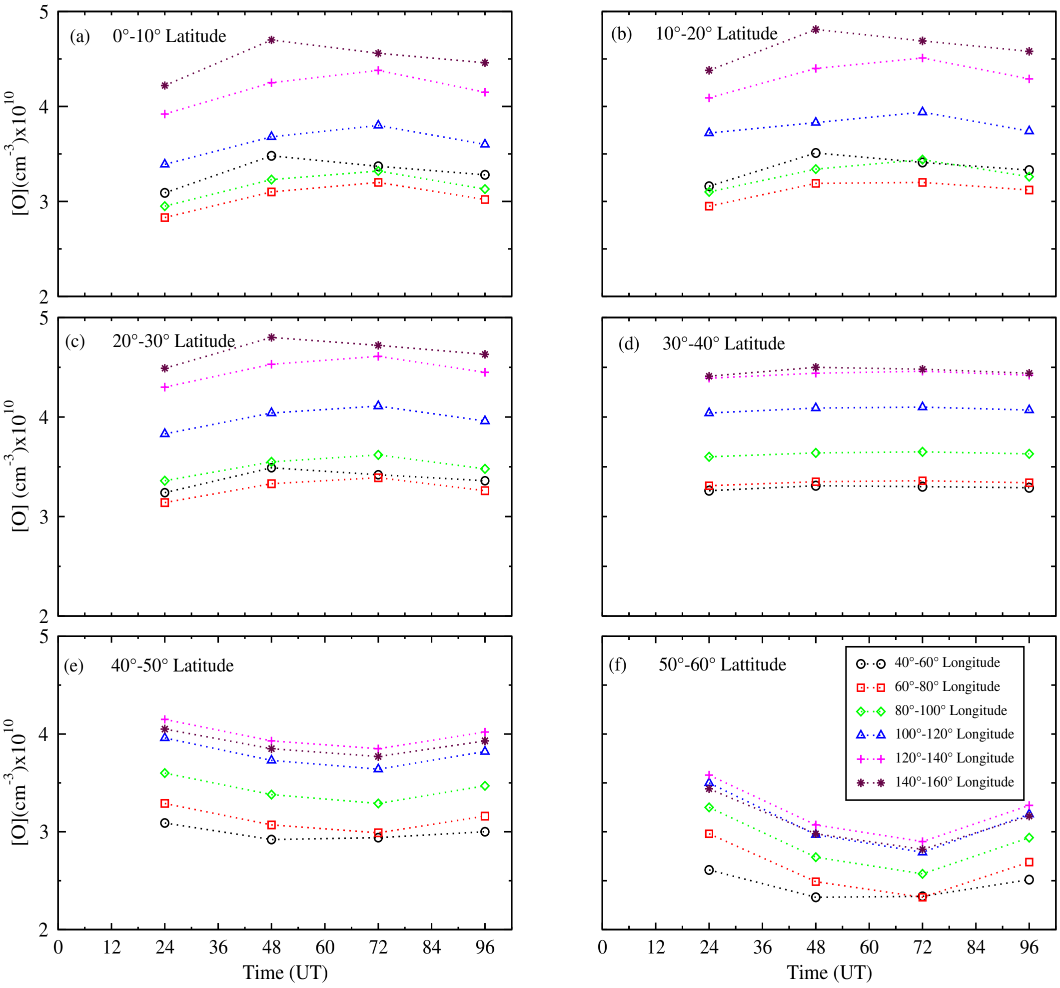

Figure 3.5: Latitudinal variation of [O] corresponding to peak NO VER during storm1

3.4.2 Latitudinal variation of peak NO VER and corresponding [O] during storm1

The latitudinal variation of peak NO VER between longitude 40°-160°E is shown in the panels (a-f) of Figure 3.4 during the storm1. The panel (a) shows the variation of cooling rate between longitude 40°-160°E within 10° latitudinal interval. It is noticeable from this panel that the maximum cooling rate is found between longitude 140°-160°E, and 40°-60°E during the main phase of the storm. Similar kind of variation is also found in panel (b) of Figure 3.4 during the main phase of the storm. Panels (a & b) show the maximum enhancement in the peak emission of NO VER between longitude 140°-160°E. However, the panel (b) shows that the magnitude of peak NO VER is slightly low compare to panel (a). Panel (c & d) also shows the enhancement in the peak of NO VER during the main phase. The maximum enhancement is found between latitude 60°-80°E, but the magnitude of peak NO VER is quite low compared to panels (a, e, & f). Panels (e & f) show the maximum enhancement in the peak of NO VER between longitude 40°-60°E and 140°-160°E, respectively. Interestingly, the maximum enhancement in the peak emission of NO VER is found between latitude 50°-60°N (panels f) during the storm time. This enhancement is due to Joule heating and particles heating in the polar region which subsequently increase the abundance of NO. Figure 3.4 shows negative correlation between the peak of NO VER and Dst index (Figure 3.1) during the main phase of the storm. It is interesting to notice that panels (a-f) of Figure 3.2 also show the maximum enhancement of peak NO VER between the longitude 140°-160°E during the main phase of the storm.

The corresponding latitudinal variation of the atomic oxygen number density between longitude 40°-160°E is shown in the Figure 3.5 during the storm1. The panels (a-d) show the enhancement in the [O] at the mid and low latitudes (0°-40°N) during the main phase of the storm, while at higher latitudes depletion is found (panel e-f). The depletion in the [O] towards the higher latitudes could be due to meridional wind that redistributes the air from higher latitudes towards the mid and low latitude. Therefore, the maximum depletion in the [O] is found at the higher latitudes, and enhancement at mid-low latitudes. It is evident from Figure 3.5 that the [O] shows a positive correlation with the peak emission of NO VER at mid and low latitude, while negative correlation at the higher latitudes. In addition to the above the atomic oxygen number density shows the positive correlation with the Dst index at higher latitude while in case of mid-low latitude vice-versa.

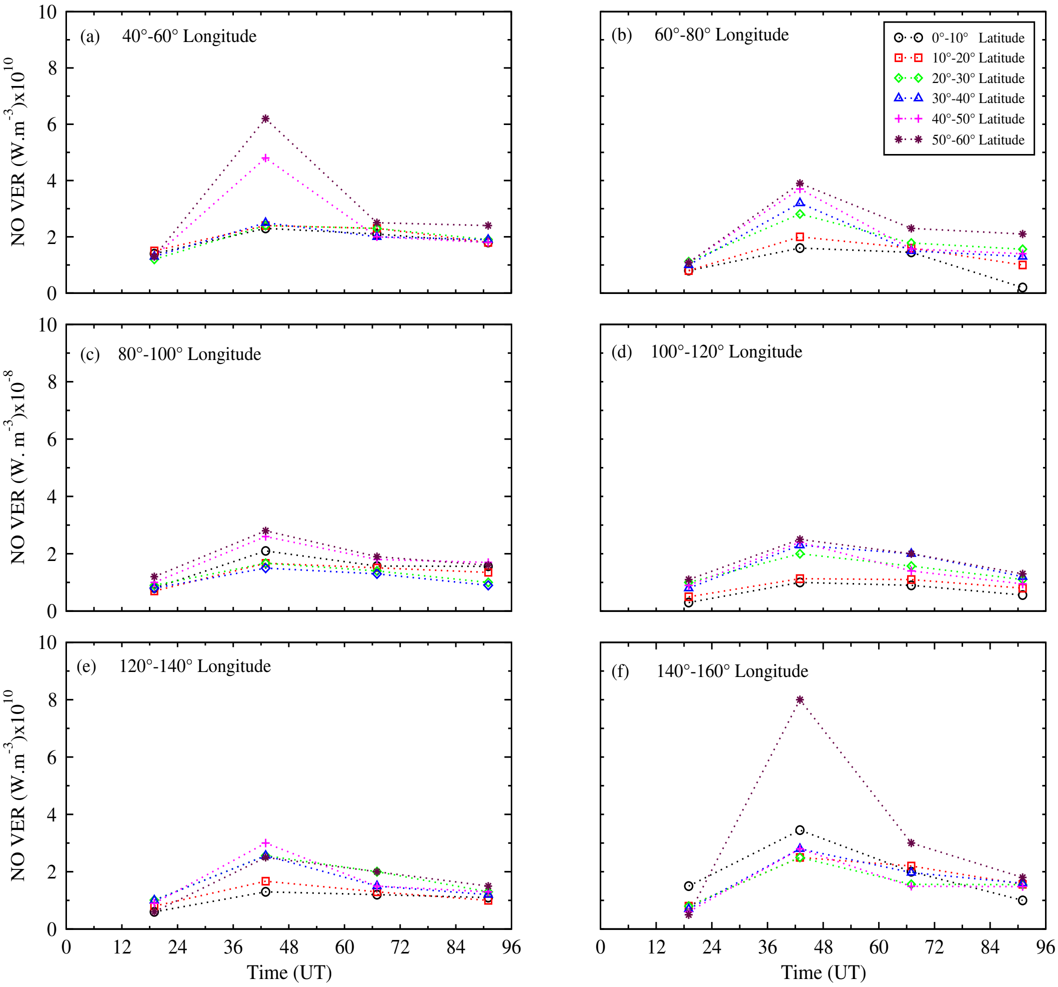

Figure 3.6: Longitudinal variation of peak NO VER during 18-21 February, 2014 (storm2)

3.4.3 Longitudinal variations of peak NO VER and [O] during storm2

The longitudinal variation of peak NO VER and corresponding [O] during the storm2 (18-21 February 2014) are shown in the Figures 3.6 (panels a-f) and Figure 3.7 (panels a-f), respectively. The panel (b) of Figure 3.1 shows the variation in the Dst index during 18-21 February, 2014. The storm reaches in its main phase on the 19 February, 2014 at 9 UT. As the storm started to recedes another storm superimposed on it. The Figure 3.6 (panels a-f) shows the longitudinal variation of cooling rate between latitude 0°-60°N. The longitudinal variation in the cooling rate is quite similar to that

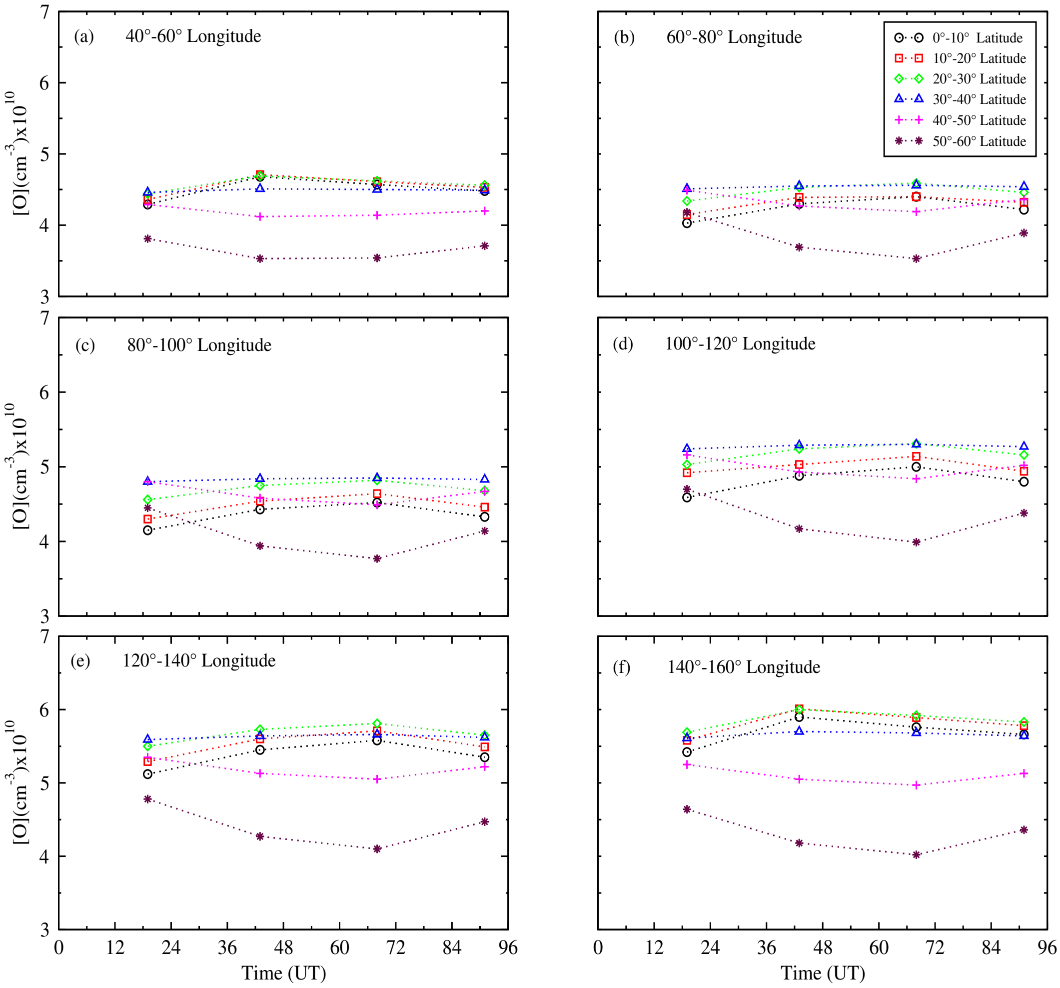

Figure 3.7: Longitudinal variation of [O] corresponding to peak emission of NO VER storm2

of storm1. The enhancement in the cooling rate during storm1 and storm2 show the strong correlation with observed Dst index. There is a positive correlation between peak emission of NO VER and corresponding [O] at the mid and low latitudes. However, at the higher latitudes negative correlation is found.

The corresponding variation in the atomic oxygen number density during storm2 is qualitatively similar as that of storm1. The atomic oxygen number density depletes during the main phase of the storm at the higher latitudes while at mid and low latitude enhancement take place as shown Figure 3.7(panels a-f). The maximum reduction in the [O] is found in the panel (f) of Figure 3.7. However, the maximum increments in the cooling rate is found between latitude 50°-60°N as shown in the panel (f) of Figure 3.6. The possible explanation for this depletion has been discussed in case of storm1.

3.4.4 Latitudinal variations of peak NO VER and [O] during storm2

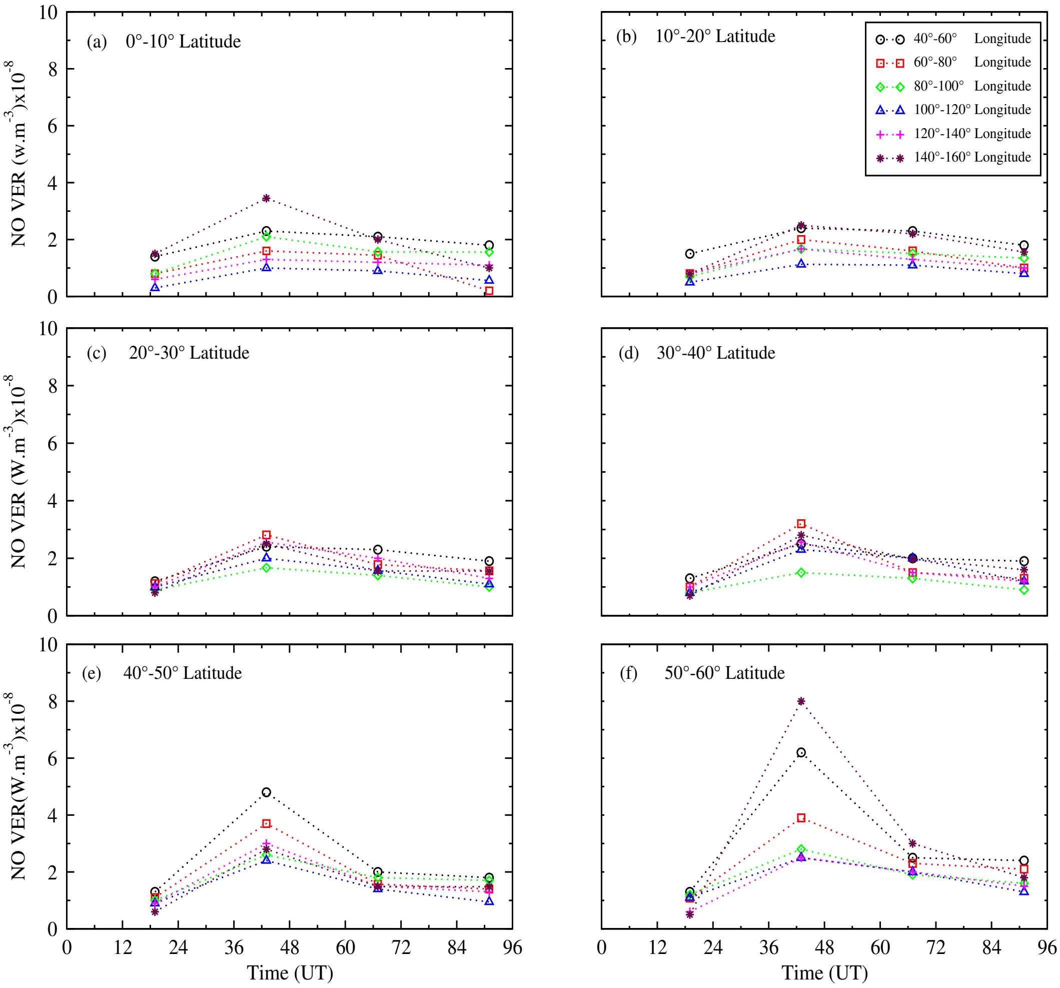

Figure 3.8: Latitudinal variation of peak NO VER during storm2

Figures (3.8 & 3.9) show the latitudinal variations of peak emission of NO VER and corresponding the atomic oxygen number density respectively, during the storm2. All panels of Figure 3.8 show cooling rate enhancement during the main phase of the

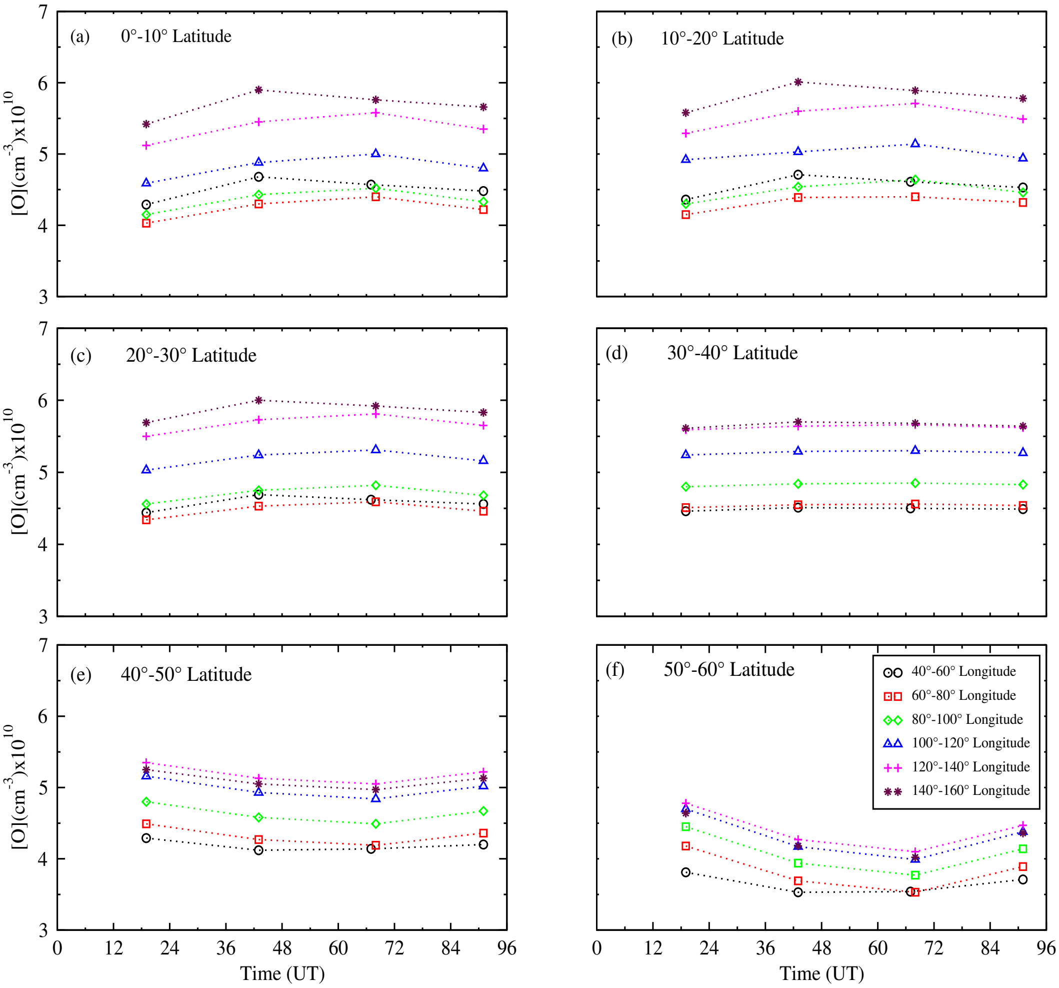

Figure 3.9: Latitudinal variation of [O] corresponding to peak emission of NO VER during storm2

storm in all latitude sectors. The similar, enhancement in the cooling rate at all latitudes is also observed during the main phase of the storm1. Figure 3.9 shows the latitudinal variation of [O] during the storm2. The fluctuations in the atomic oxygen number density is qualitatively similar as found in case of storm1. The possible explanation of [O] fluctuations is discussed above in case of storm1.

3.5 Conclusion

The latitudinal and longitudinal variation of peak emission of NO VER at 5.3 μm and corresponding atomic oxygen number density have been studied during the two geomagnetic storms over Asian sector. The data for cooling rate for NO emission is taken from SABER onboard on TIMED satellite and neutral density from NRLMSISE-00 model. It is found that the peak emission of NO VER increases gradually from lower latitudes towards higher latitudes. The peak emission of NO VER shows negative correlation with the Dst index. The atomic oxygen number density shows a positive correlation with Dst index at higher latitudes, while negative correlation at the mid-low latitudes during the main phase of the storm. The peak emission of NO VER at the higher latitudes shows the negative correlation with the atomic oxygen number density, while positive correlation at the mid-low latitudes during the storm. The depletion in the peak emission of NO VER towards the low and mid latitudes may be due to meridional wind which is generated due to Joule heating and particle heating in the polar region.

CHAPTER 4

EFFECT OF SPACE WEATHER EVENTS ON SODIUM AIRGLOW EMISSION

4.1 Introduction

The Sun drives the chemistry and dynamics of the Earth's atmosphere with varying time-scale. The significant effect of 11 year solar cycle have been observed on the Earth's atmospheric species by [203]. The Coronal Mass Ejections (CME) and solar flares are the most dominant sources of highly energetic charged particles that influence the Earth's atmosphere. The formulation of highly energetic charged particles such as protons, electrons, and ions are significantly enhanced during the CME and solar flare. These highly energetic charged particles are mostly precipitated into the Earth's middle and upper atmosphere through the high latitudes region (geomag-

---

The results presented in this chapter have been submitted in a research publication: Gaurav Bharti, M. V. Sunil Krishna, Effect of space weather events on sodium airglow emission, J. Geophys. Res.: Space Physics, 2018.

netic latitude >60°) due to presence of Earth magnetic field. The CME associated interplanetary shock waves accelerate the protons causing the sudden enhancements of proton flux near the Earth, which is known as the solar proton events (SPE). This enhancement in proton flux induces change in the neutral and ion densities in the atmosphere [204–211]. This occurs due to the interaction which undergoes a series of processes such as ionization, dissociation, excitation of atmospheric species.

It is well known that the mesosphere-lower-thermosphere (MLT) is the main source region for the meteoric metallic species such as Na, Fe, K etc. Among all the meteoric metals, sodium (Na) is extensively studied due to its large scattering cross section which makes it an excellent tracer for the thermal and dynamic state of MLT region [25, 26]. A number of sources for free sodium atoms have been reported in the literature, but the dominating source is the impact of Ozone (O_3) with sodium [212]. The neutral sodium atoms upon excitation and de-excitation result in Na airglow. The de-excitation of sodium atoms to the ground state results in the emission of sodium doublet at 589.0 nm and 589.6 nm. These lines are well known as the sodium D lines. The chemical scheme for the sodium airglow is given below [26, 213, 214].

$$\mathrm{Na} + \mathrm{O_3} \xrightarrow{k_1} \mathrm{NaO} + \mathrm{O_2} \tag{4.1}$$

$$\mathrm{NaO} + \mathrm{O} \xrightarrow{\alpha k_2} \mathrm{Na}^*(^2P_J) + \mathrm{O_2} \tag{4.2}$$

$$\mathrm{NaO} + \mathrm{O} \xrightarrow{(1-\alpha)k_2} \mathrm{Na}(^2\mathrm{S}) + \mathrm{O_2} \tag{4.3}$$

$$\mathrm{Na}^*(^2\mathrm{P}_J) \rightarrow \mathrm{Na}(^2\mathrm{S}) + h\nu\ (589.0\ nm, 589.6\ nm) \tag{4.4}$$

Where α is a branching ratio and k reaction rate coefficient. From the above chemical scheme it is evident that the sodium airglow emission in the mesosphere mainly depends on the Ozone (O_3) and atomic oxygen (O) densities [26]. In addition, the airglow intensity also depends on the mesospheric temperature. Fan et al. [215] and Clemesha et al. [123] reported a strong correlation between mesospheric temperature and sodium abundance due to temperature-dependent sodium chemistry.

Ozone has secondary peak at the mesospheric altitude and it significantly influences the sodium concentration during the SWE. It has been established that mesospheric Ozone shows depletion during solar proton events observation and model based studies [205, 206, 216–219]. The depletion of Ozone abundance during the 23^{rd} solar cycle has been reported by Krivolutsky et al. [218] and Jackman et al. [209] by using the model based study. Similarly, Jackman et al. [207] and Verronen et al. [206] reported the depletion in the Ozone abundance about 70% and 90% during SPE of July 2000 and January 2005 by using the UARS HALOE and NOAA 14 SBUB/2, and GOMOS/ENVIRSAT measurements, respectively. This Ozone depletion is altitudinal dependent due to the enhanced production of odd hydrogen and odd nitrogen species during a SPE event [206]. Odd hydrogen is responsible for the depletion of Ozone in mesosphere while odd nitrogen species play an important role in low altitude to reduce the Ozone abundance [206].

The MLT region is highly sensitive to external forcing such as waves, tides from the below and solar activity from the above [31, 214]. There have been a number of studies to examine the response of MLT region to various geophysical conditions, atmospheric waves, and tides. However, there are limited studies that have been reported to investigate the response of metallic layer such as sodium abundance in the MLT region to various geophysical conditions and thus, the response of metal layers to the varying geophysical conditions is still unclear. Few studies have pointed towards the enhanced abundances [45, 46] while few others have reported depleted abundance of sodium during a space weather event [43,220,221]. Recently, the long-term response of sodium abundance has been reported by Dawkins et al. [214] using the National Center for Atmospheric Research (NCAR)'s Whole Atmospheric Community Climate Model (WACCM) which shows a significant variation with 11 year solar cycle. The sodium abundance also shows a significant variation in the high as well as low latitude regions. The effect of auroral particle precipitation on sodium has been studied by the Tsuda et al. [221] and Takahashi et al. [43]. Tsuda et al. [221] reported a significant depletion in the sodium abundance over Tromso, Norway (69.6°N, 19.2°E) from 24-25 January 2012, by using the common-volume-observation by European Incoherent Scatter (EISCAT) VHF radar and by a sodium lidar. These simultaneous observations show a nightly mean sodium density depletion by 60 percent at an altitude of 100 km. Similar kind of depletion has also been reported by Takahashi et al. [43] during pulsating auroras in January 2012. These results indicate the possible effects of geomagnetic activity on the metallic abundances in the mesosphere. This might be due to the charge exchange reactions between sodium and molecular charged species and energetic charged particles.

From the above discussion it is clear that the chemical compositions, dynamics of the MLT region are significantly influenced by the geomagnetic conditions. The abundances of metallic species in addition to the neutral species such as O, O_2, and N_2 are also proved to be susceptible to changes induced by strong geomagnetic activity. The airglow resulting from these chemical species is naturally expected to be correlated to geomagnetic activity. So far, to the best of our knowledge, no studies have been reported to examine the effect of space weather events simultaneous on sodium abundance and variation of sodium airglow emission and the possible correlation with the participating chemical species. In present study, we will examine the effect of geomagnetic storms and solar proton events on sodium abundance and Na airglow at 589.6 nm. This study is first of its kind to examine the simultaneous effect of storms and solar proton events on sodium abundance, sodium airglow and Ozone abundance.

4.2 The sodium Airglow model

There are very few studies reported in the literature to calculate the altitudinally resolved volume emission rate and intensity of sodium airglow emission [28,31,222,223]. These studies were mostly used density profile derived from either ground based airglow intensity or rocket measurement intensity. In the present study we have used photochemical model of sodium airglow emission to calculate the Volume Emission Rate (VER) and columnar brightness of sodium airglow. The model can be used for any given latitude and longitude and will require the abundances of neutral species, Ozone and sodium. The model is validated using a variety of measurements such as the combined rocket and lidar measurements [223], rocket and imager study of Clemesha et al. [222], and the lidar and photometer observation of Sarkhel et al. [29, 30]. The model is further updated by incorporating latest reaction rate coefficients of few key chemical processes. The updated reaction rate coefficients are summarized in table 4.1. The detailed description of this model is given by Bag et al. [25]. The VER

Table 4.1: Updated reaction rate coefficients for Na airglow emission

Reaction	Rate coefficients	Value	reference
$NaO+H_2O \rightarrow NaOH+H$	k_1	$5.06 \times 10^{-10} \cdot \exp(-240/T)$	[224]
$NaOH+CO_2+M \rightarrow NaHCO_3+M$	k_2	$2.3 \times 10^{-28} \cdot (T/300)^{-4.12}$	[224]
$NaOH+CO_2+M \rightarrow NaCO_3+M$	k_3	$1.2 \times 10^{-27} \cdot (T/300)^{-3.14}$	[224]

of sodium D line emission mainly depends on the production mechanism, loss mechanism, and the reaction rate coefficient of the sodium. The production mechanism for sodium can be broadly divided into three types namely, ion, neutral, and photochemistry, depending on the peak density of sodium layer. The ion chemistry dominated above the peak density of sodium layer, while neutral chemistry dominated above the peak density of sodium layer. On the other hand, the photochemistry dominated during the daytime and plays an important role for the formation of sodium D line. The volume emission rate for the sodium D line is the sum of the production rate due to ion, neutral, and photochemistry sources. The detailed chemistry of production rate and VER is given by Bag et al. [25].

4.3 Data Acquisition

The neutral sodium density and temperature have been obtained from the Utah State University (USU) Na lidar located at Logan, Utah (41.7°N, 111.8°W). Initially the sodium Doppler lidar was located at Fort Collins, CO (41°N, 105°W), and it was relocated to USU in 2010. This lidar is an advanced resonance Doppler lidar operating at the Na D2 line (589.159 nm) and 120 MHz FWHM (full width at half maximum) laser pulse bandwidth. This lidar has the ability to continuously monitor MLT region for parameters such as neutral temperature, horizontal wind, and sodium density in full diurnal cycles under clear sky conditions [225, 226]. The detailed techniques to extract data of various parameters such as density, temperature, tidal perturbation have been reported by She et al. [227]. In the present study we have used hourly averaged Na density and temperature to calculate the VER of Na airglow using the Na airglow model.

The Na airglow model requires the abundances of neutral species, such as [O_2], [N_2], and charged species concentrations such as [O_2^+], [NO^+], . These abundances have been obtained from NRLMSISE-00 and IRI-2012 model, respectively [165,166]. The atomic oxygen [O], Ozone [O_3] and Hydrogen [H] densities have been derived from the measurements of SABER (Sounding of the Atmosphere Broadband Emission Radiometry) on board TIMED (Thermosphere Ionosphere Mesosphere Energetics Dynamics) satellite. The storm events are identified using the Dst index, obtained from the Word Data Center (WDC) for Geomagnetism, Kyoto, Japan. The proton flux is obtained from Space Weather Prediction Center (www.swpc.noaa.gov) GOES satellites.

4.4 Results & Discussion

In this study, we have presented the effects of space weather events on sodium density and resulting airglow emission by relating them with the fluctuations seen in Ozone

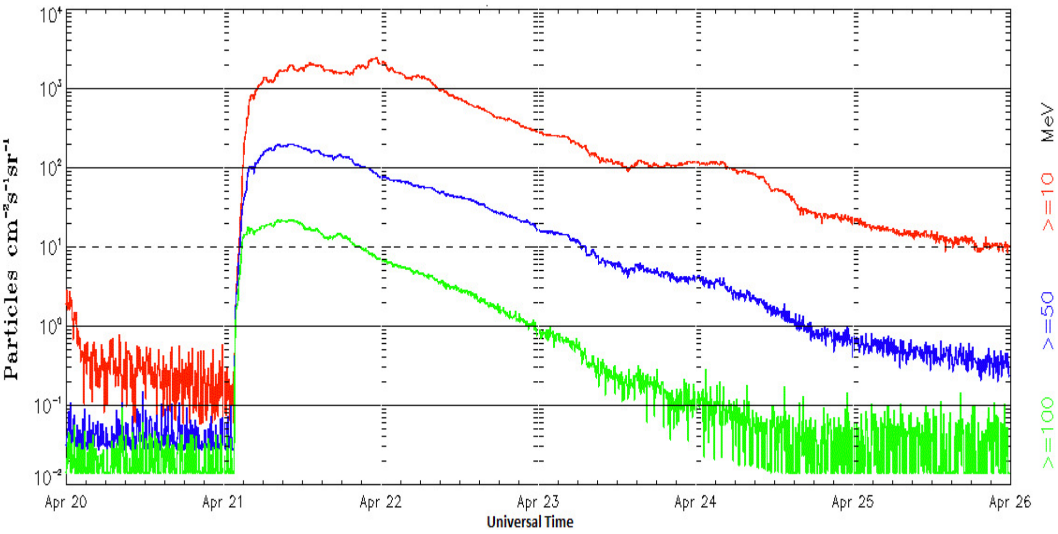

Figure 4.1: Solar proton flux observed by GOES during 20-26 April, 2002

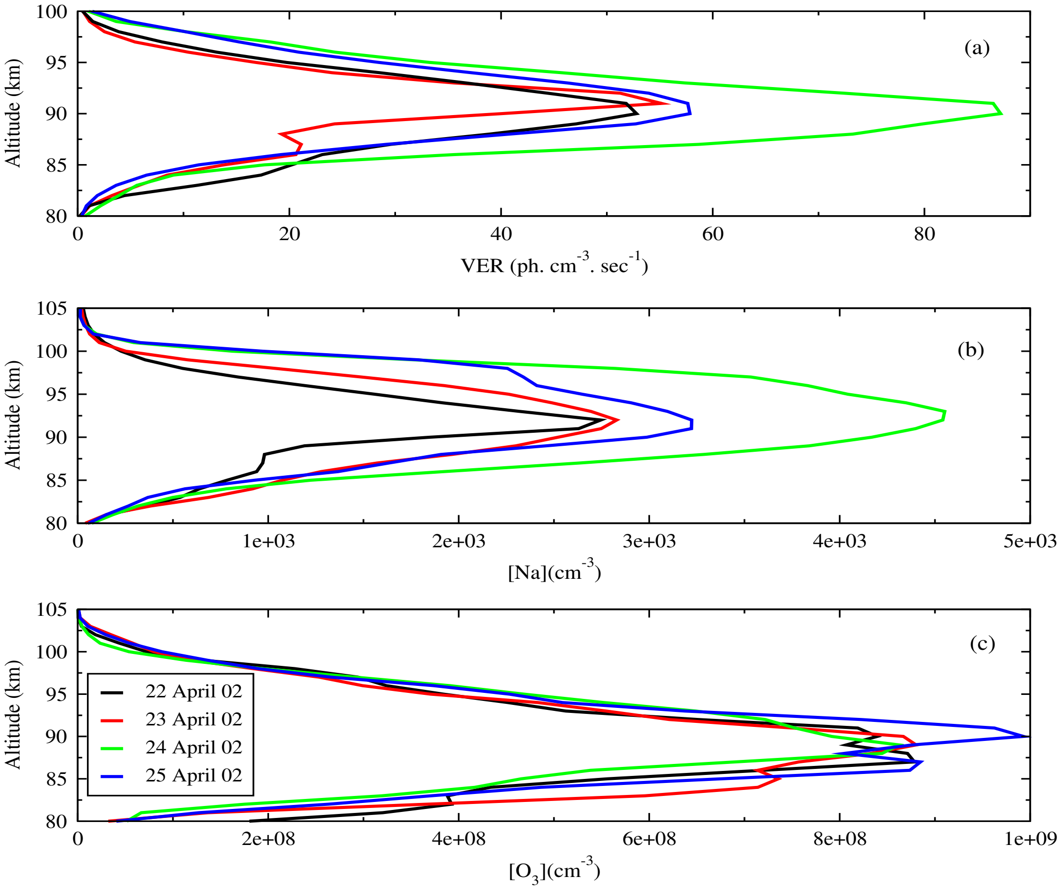

Figure 4.2: Variation of Na VER (a), [Na] (b), and [O_3] (c), during the solar proton event (22-25 April, 2002).

and Na densities. This study is the first of its kind to report simultaneous effects of geomagnetic storms and solar proton events on Na, O_3 abundance and the resulting Na airglow. The results have been broadly divided into two parts (1) effect of SPE (2) combined effect of geomagnetic storm and SPE. This study brings together analysis based on lidar measured Na abundance, temperature data, and model based Na airglow volume emission rate profiles.

During 22-24 April, 2002 an X class solar flare was produced near the Sun's surface accompanied by a strong radio burst and parallel halo CME. The velocity of this CME was around 2400-2500 km/s. This CME induced solar proton flux enhancement can be seen in Figure 4.1. We can see a sudden enhancement in proton flux (> 50, and 100 MeV) at around 2 UT on 21 April 2002. The proton flux (>10 MeV) shows maximum enhancement at 2320 UT. This can be considered as a very intense proton event spanning over several days, the same period has been observed to be geomagnetically quiet (Dst=-38 nT). During this period, the measured Na density (Utah State University (41°N, 105°E) Na lidar) is shown in Figure 4.2(b). The density of Na and Ozone (from SABER) are used in the model calculation to obtain volume emission rate of Na airglow.

It can be seen from Figure 4.2(b) that Na density is depleted during the main phase of the SPE with a minimum density on 22 April and it increases as we move towards the recovery phase with maximum density on 24 April, indicating that the proton flux and Na density are anti-correlated. This depletion in Na density during the particle events can be due to the charge transfer reactions between Na atoms and molecular ions produced by energetic particles. It has been found that, during the SPE, highly energetic charged particles produce the NO^+ and O_2^+ ions at mesospheric heights. As a result, these ions react with neutral Na as shown below leading to the loss of neutral Na atoms and increase of Na^+ ions.

$$\mathrm{Na} + \mathrm{NO}^+ \rightarrow \mathrm{Na}^+ + \mathrm{NO} \tag{4.5}$$

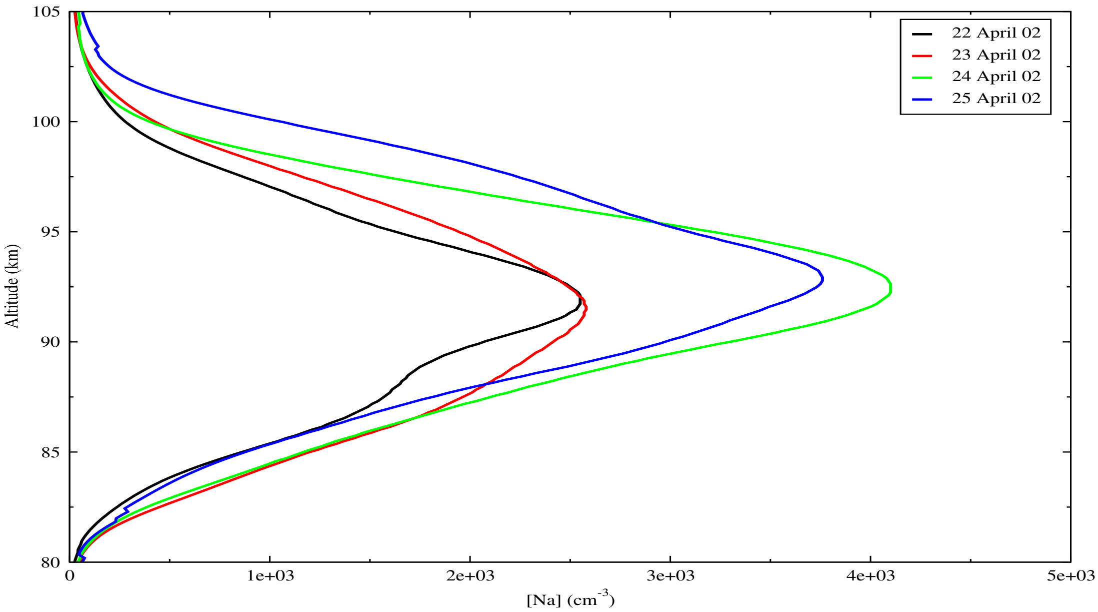

Figure 4.3: Nightly averaged Na density during solar proton event (22-25 April, 2002).

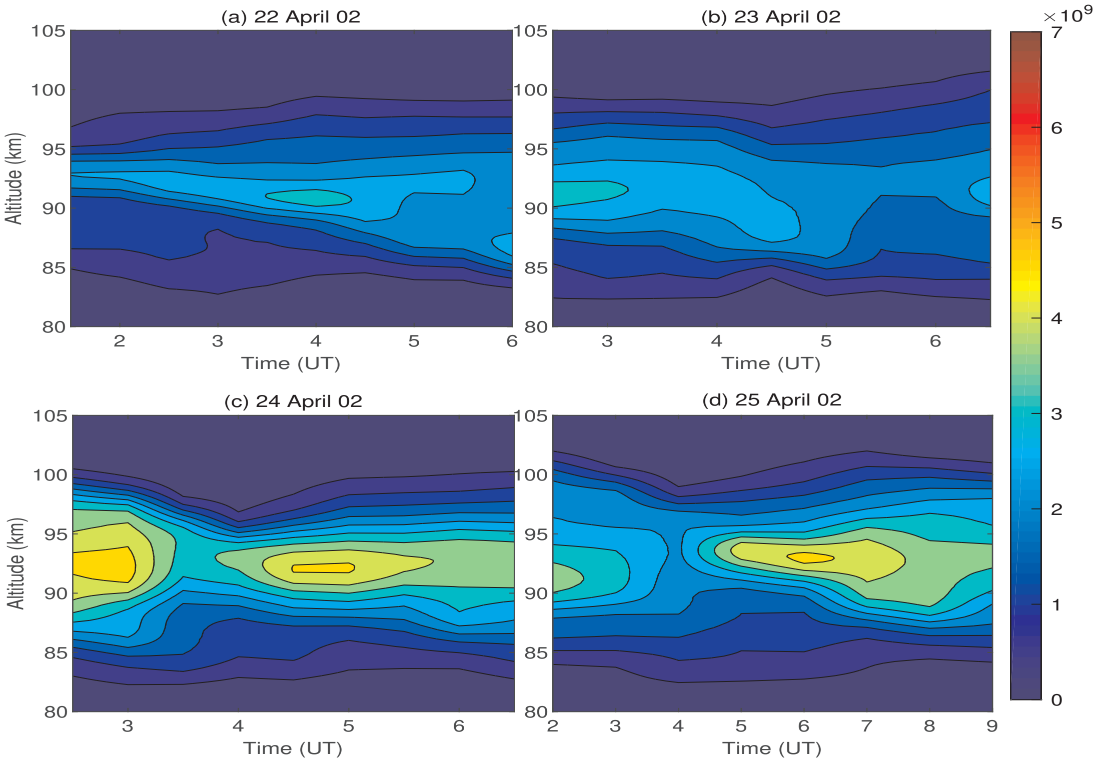

Figure 4.4: Variation of Na density with solar proton event .

$$\mathrm{Na} + \mathrm{O}_2^+ \rightarrow \mathrm{Na}^+ + \mathrm{O}_2 \tag{4.6}$$

It has been proven [228] that this effect is very significant above 85 km. In addition, the increase in the electron and ion densities during SPE also contributes to the decrease in Na density at these altitudes [43].

Figure 4.2(c) shows the variation of Ozone density during 22-25 April 2002 as observed by the SABER on board on TIMED satellite. It is noticeable from Figure 4.2(c) that the Ozone density shows a slight depletion just after the main phase of the proton event. The density recovers to a maximum value on 25 April during the recovery phase of the SPE. A similar kind of depletion in the Ozone density during the SPE has also been reported by using satellite and model-based studies [203, 207, 229–231]. Recently, Zou et al. [232] reported the depletion in the Ozone density by using the Aura Microwave Limb Sounder. During the SPE, energetic charged particles are deposited in the middle and upper atmosphere leading to the creation of ionized radicals such as HO_x (H, HO, and HO_2), and NO_x(N, NO, and NO_2). These radicals act as catalysts and destroy the Ozone molecules in mesospheric heights [232].

The variation in the modeled VER of Na airglow is shown in Figure 4.2(a). From the chemistry discussed in the earlier sections, it is very clear that the Na airglow intensity is very sensitive to the fluctuations in [Na] and $[O_3]$. We can see from Figure 4.2(a) that the airglow intensity follows a similar trend as seen in [Na] and $[O_3]$ with a minimum emission rate on 22 April, 2002. From the reaction 4.1, we can say that during the SPE, the production of NaO starts to decrease leading to the depletion in the number of excited sodium atoms. As a result, we see the VER to be depleted.

The nightly averaged Na densities during the SPE are shown in Figure 4.3. It can be seen that the Na density is minimum during the main phase of the particle event and slowly increases with the recovery. Further, the peak altitude of Na density shows a slight shift towards the higher altitudes with the progression of the event. The increase of Na density with the recovery of solar proton event can also be seen

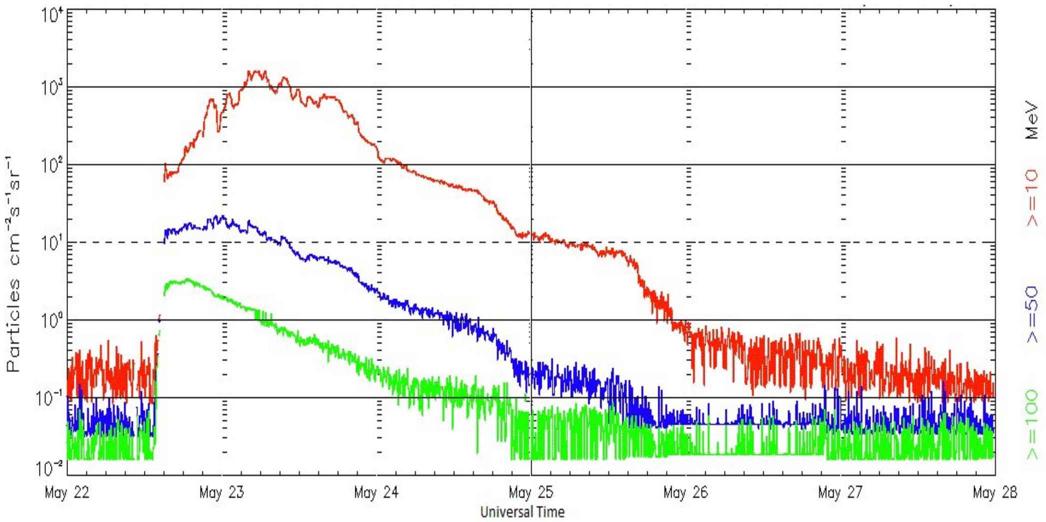

Figure 4.5: Solar proton flux observed by GOES (22-28 May, 2013).

Figure 4.4. From the above discussion, we can say that solar proton event causes the Na and O_3 densities to decrease and their fluctuations also reflect in the airglow emission intensities.

An M5.0 class solar flare Occurred on 22 May 2013 at around 13 UT Which was a magnetic quiet time (Dst = -10 nT). This solar flare lead to a solar proton event during 22-28 May 2013 as shown in Figure 4.5. The maximum enhancement in the proton flux is found in the 10 MeV range on 23 May at around 6-7 UT with nearly 1660 pfu. On the other hand proton flux with energy greater than 100 and 50 MeV show, maximum enhancement on 22 May at around 15 UT. As the SPE recedes, the proton flux starts to recover to its pre-onset value. The influence of this SPE on sodium airglow emission is shown in Figure 4.6(a).

The variation in the Na VER, [Na] and [O_3] during the solar proton event (22-26 May, 2013) is shown in Figure 4.6. It can be seen that the densities and airglow are depleted during the main phase of SPE and they start to recover as the proton particle flux returns to the base value. The enhancement in densities is profoundly seen in Figure 4.6(b & c). These fluctuations follow the earlier cases discussed in paragraphs above. Based on these two cases (Figure 4.2 & 4.6) of isolated solar proton events,

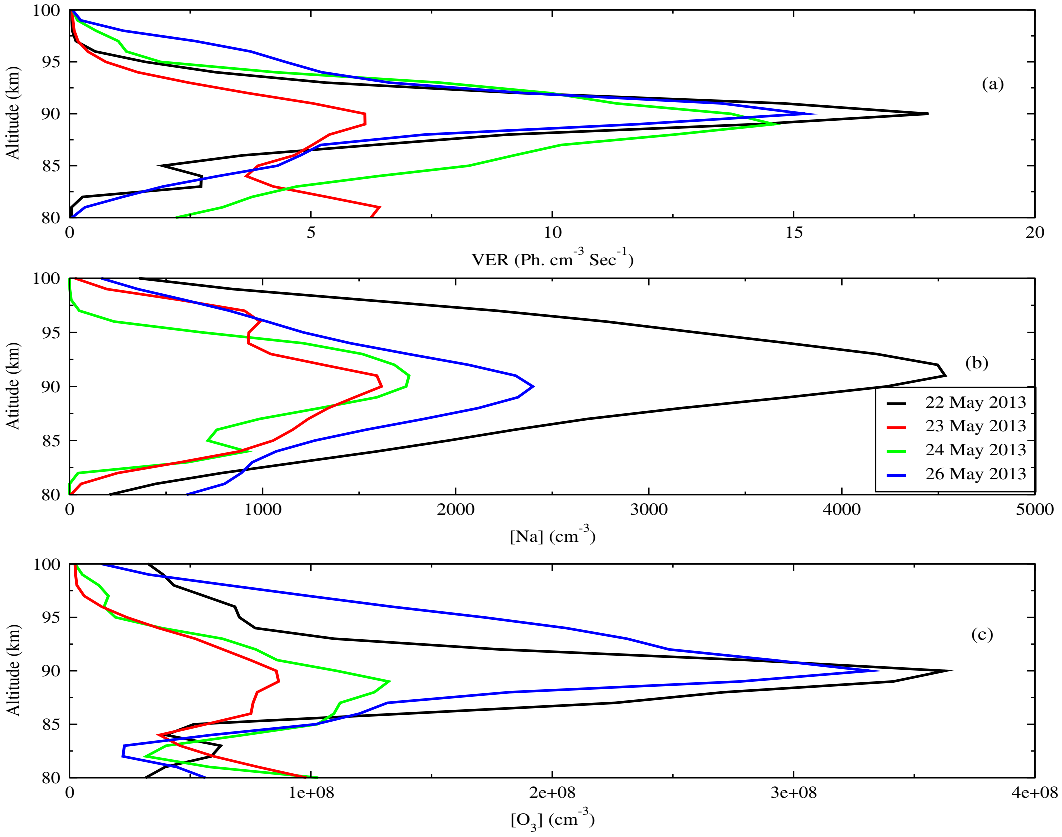

Figure 4.6: Variation of Na VER (a), [Na] (b), and [O_3] (c), during the solar proton event (22-26 May, 2013).

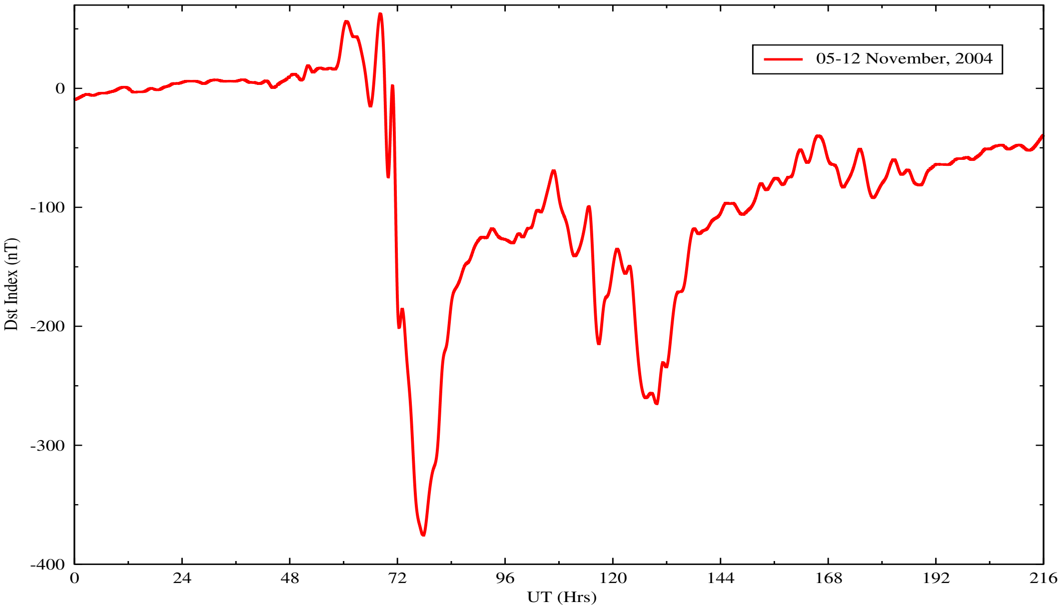

Figure 4.7: Variation of Dst index during the geomagnetic storm (05-08 November, 2004).

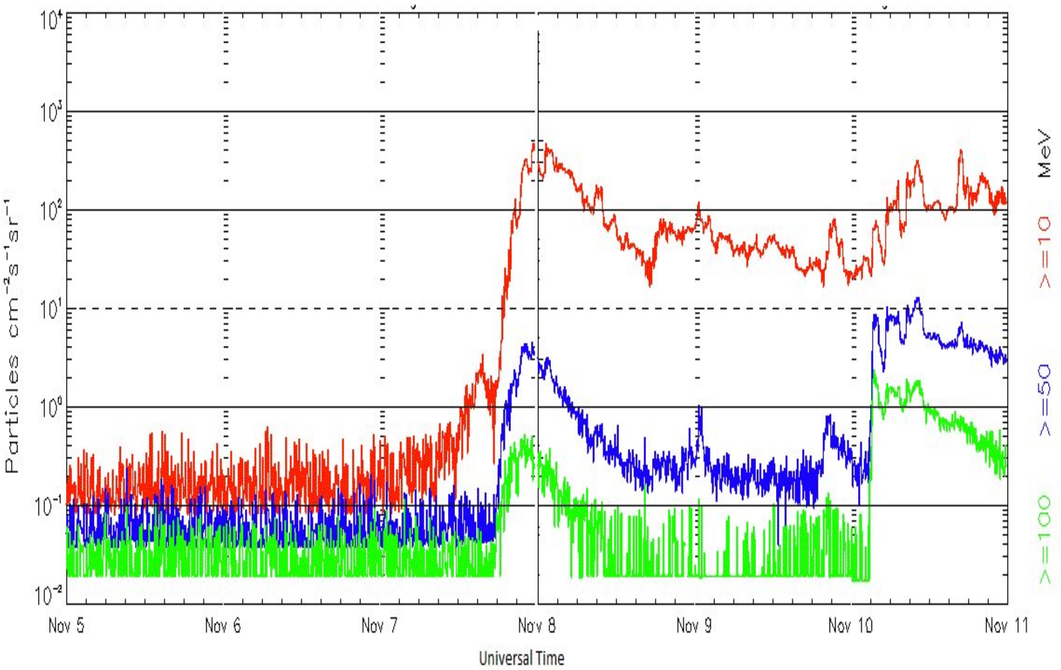

Figure 4.8: Solar proton flux observed by GOES (05-11 November, 2004).

we can say that the densities and airglow emission intensity are anti-correlated with the advent of 10 and 50 MeV proton flux.

In order to understand the effect of geomagnetic storms on Na abundance and airglow, we have considered a period of intense geomagnetic storm during 05-12 November, 2004. This storm is also accompanied by an increase in proton flux during 8-12 November 2004. The storm resulted from two groups of sun spots that appeared on the visible solar disk in the beginning of November 2004. This magnetic storm is considered as one of the most intense (Dst = -347 nT) in the space era. During this period, the measurement of Na density is available for three nights (5, 7, 8 November). This dataset can be assumed to be indicative of the effect of storms on Na density. The period of minimum Dst coincides with the enhanced proton flux on 8 November 2004 at 7 UT (Figure 4.7 & 4.8). The combined effect of SPE and geomagnetic storm on the airglow and densities is shown in Figure 4.9. It can be seen that at the storm's onset, the densities (Figure 4.9(b & c)) are severely depleted resulting in the decrease of airglow intensity. The depletion in Ozone density could

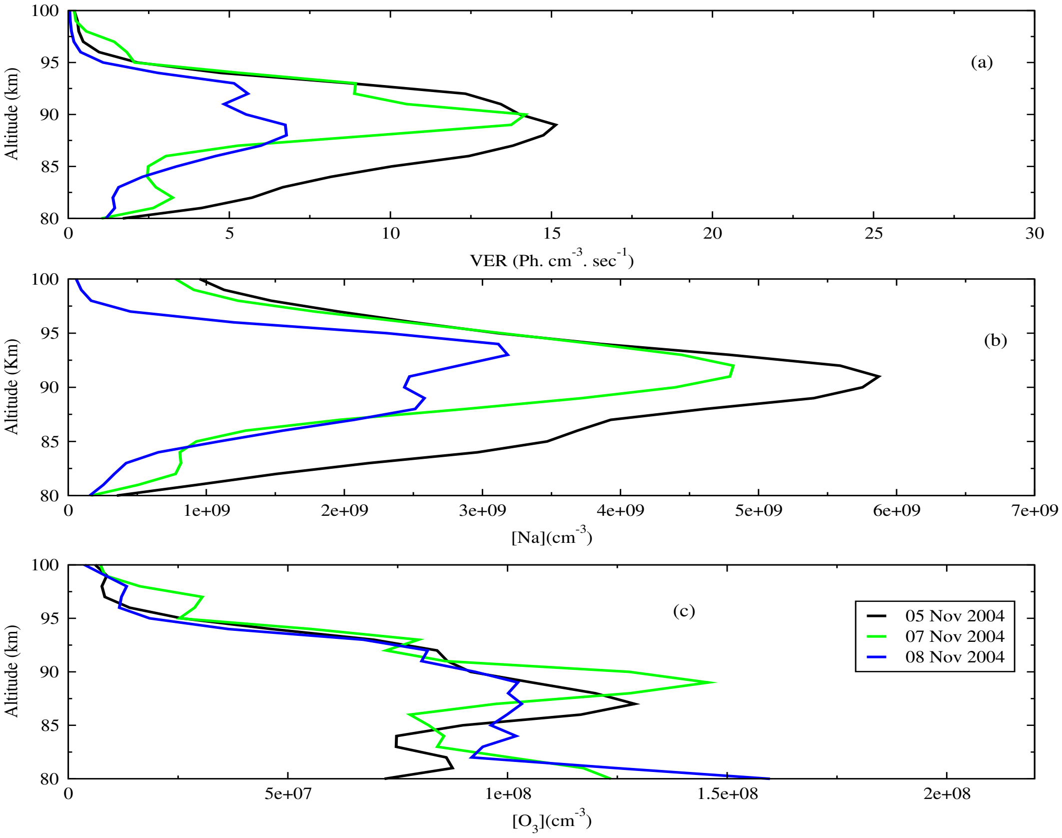

Figure 4.9: Variation of Na VER (a), [Na] (b), [O$_3$] (c), during solar proton event (05-08 November, 2004).

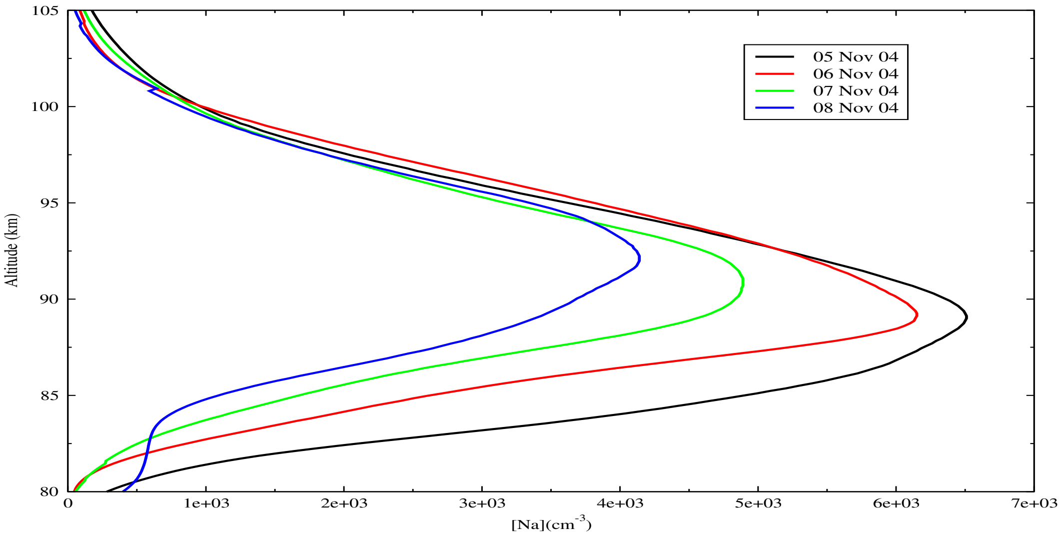

Figure 4.10: Nightly averaged Na density during solar proton event (05-08 November, 2004).

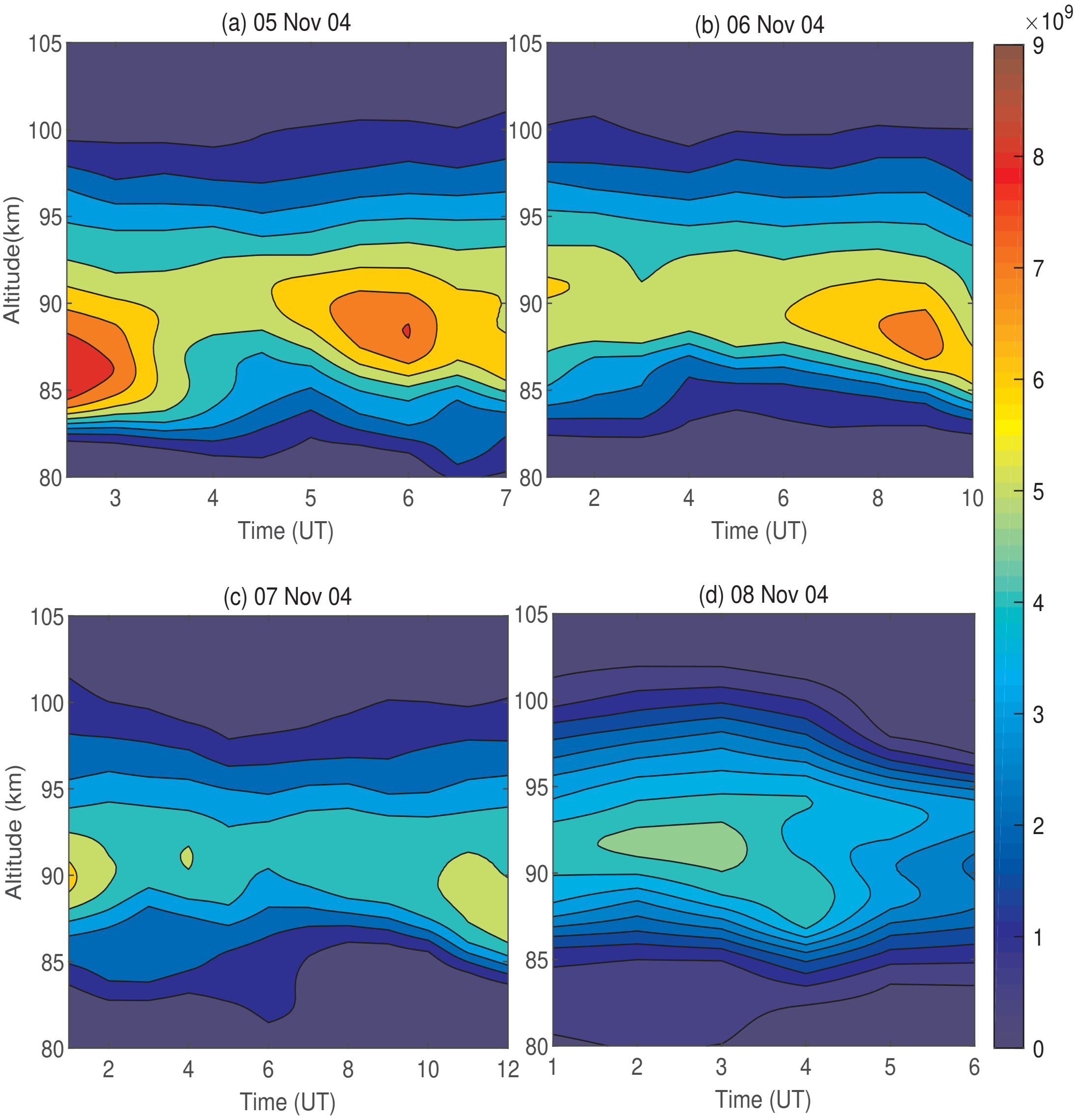

Figure 4.11: Variation of Na density as a function of time during solar proton event (05-08 November, 2004).

be due to the enhanced ionization of atmospheric species. A similar type of depletion in Na density during geomagnetic storms has been reported by Tsuda et al. [221] by using optical Spectrograph and Infrared Imager System on board the Odin satellite and by Takahashi at al. [43] by using the EISCAT radar. These studies also propose the same mechanism for the loss of neutral Na due to charge exchange reaction listed in reactions (4.5 & 4.6) triggered by the increased electron and ion densities during storm period. This case allows to conclude that the fluctuations in neutral Na and O_3 are anti-correlated with the storm time index (Dst) as well as along with the proton flux. The nature of Na depletion during the storm is well supported by the nightly averaged Na densities as shown in Figure (4.10 & 4.11).

A similar case of solar proton event superimposed on the background of a geomagnetic storm is shown in Figure (4.12 & 4.13). A X5 solar flare resulted in an intense geomagnetic storm during 8-12 March, 2012. The solar flare has led to an enhanced proton flux at nearly 2 UT on 7 March 2012. It can be seen that the proton flux (100 and 50 MeV) undergoes a large increase on 7 March and flux in the energy range of 10 MeV spikes on 8 March, 2012. Interestingly, minimum Dst (-145 nT) is observed at 9 UT on 9 March 2012. The Na density data is available from 8-11 March, 2012, which gives a very good overlap with the storm. We have performed a similar analysis of modeling Na airglow and correlated it with, Na density, and O_3 density during the overlapping period of geomagnetic storm and SPE.

The variation of modeled airglow emission rate with height during the storm is shown in Figure 4.14 (a). The temperature profile measured by Lidar has been used in the model calculation. The neutral Na and O_3 densities are shown in Figure 4.14(b & c). It can be very clearly seen that the airglow emission intensity is maximum in the recovery phase and minimum during the main phase of storm. The airglow emission rate is proportional to the available Na density. The Na density as measured by Lidar shows a strong depletion during the main phase of storm and SPE and hence can be said to be anti-correlated to the Dst index and proton flux. These results support our earlier inference of space weather effects on the Na and O_3 densities,

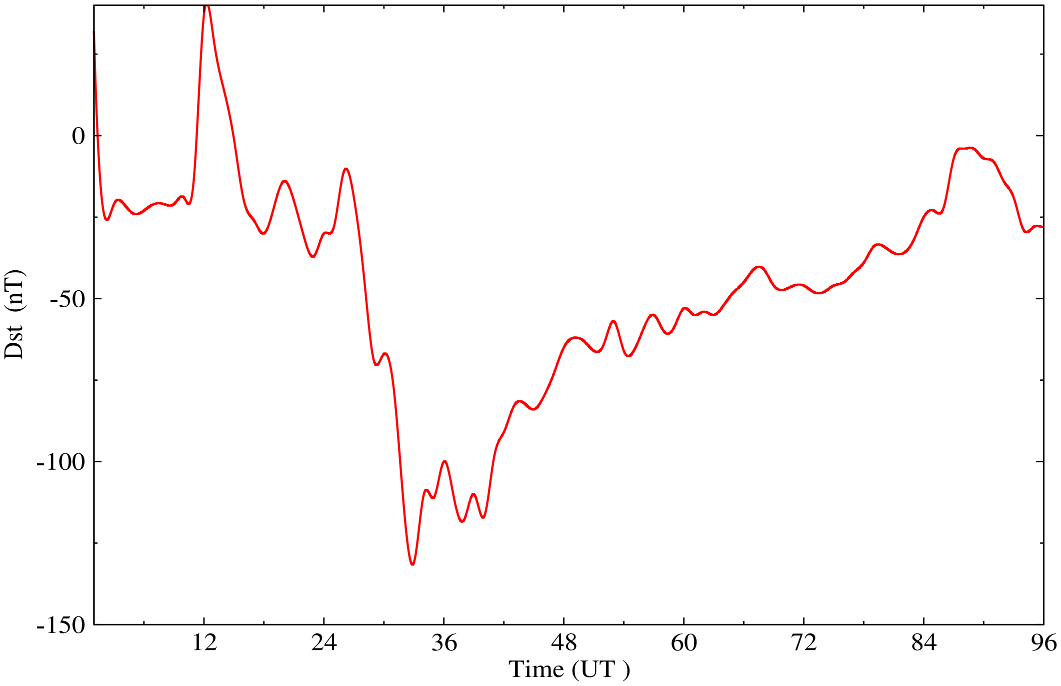

Figure 4.12: Variation of Dst index during the geomagnetic storm (08-11 March, 2012).

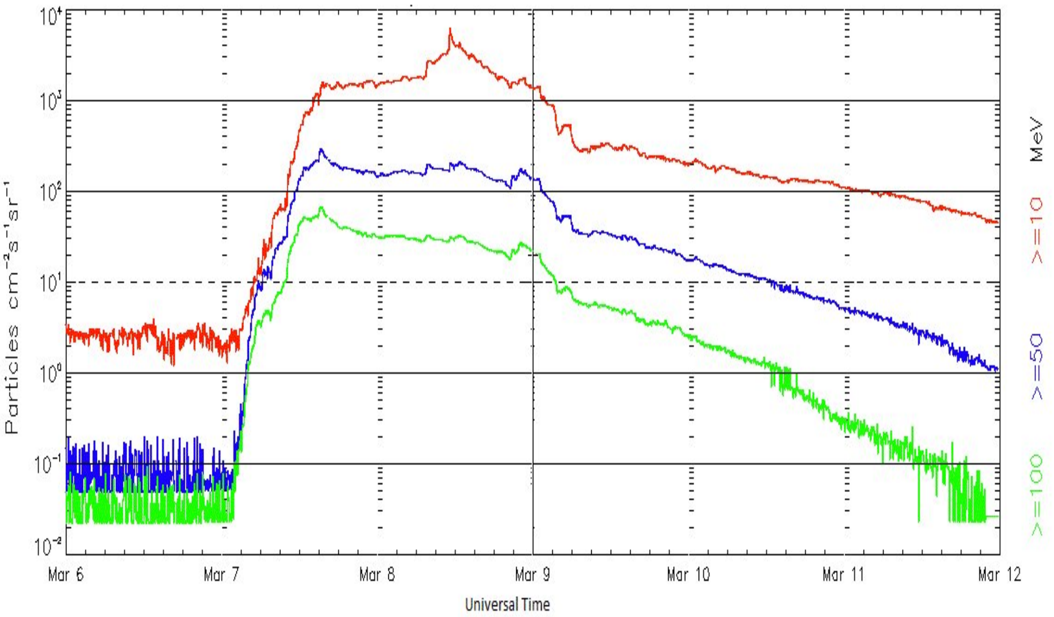

Figure 4.13: Solar proton flux observed by GOES (06-12 March, 2012).

and airglow emission rate. They also corroborate the decrease of density due to the charge exchange and recombination reactions. The energetic particles are mainly responsible by increasing the ion and electron densities, increased production of HO_x (H, HO, and HO_2), NO_x(N, NO, and NO_2) leading to the destruction of available neutral density of metal atoms and Ozone.

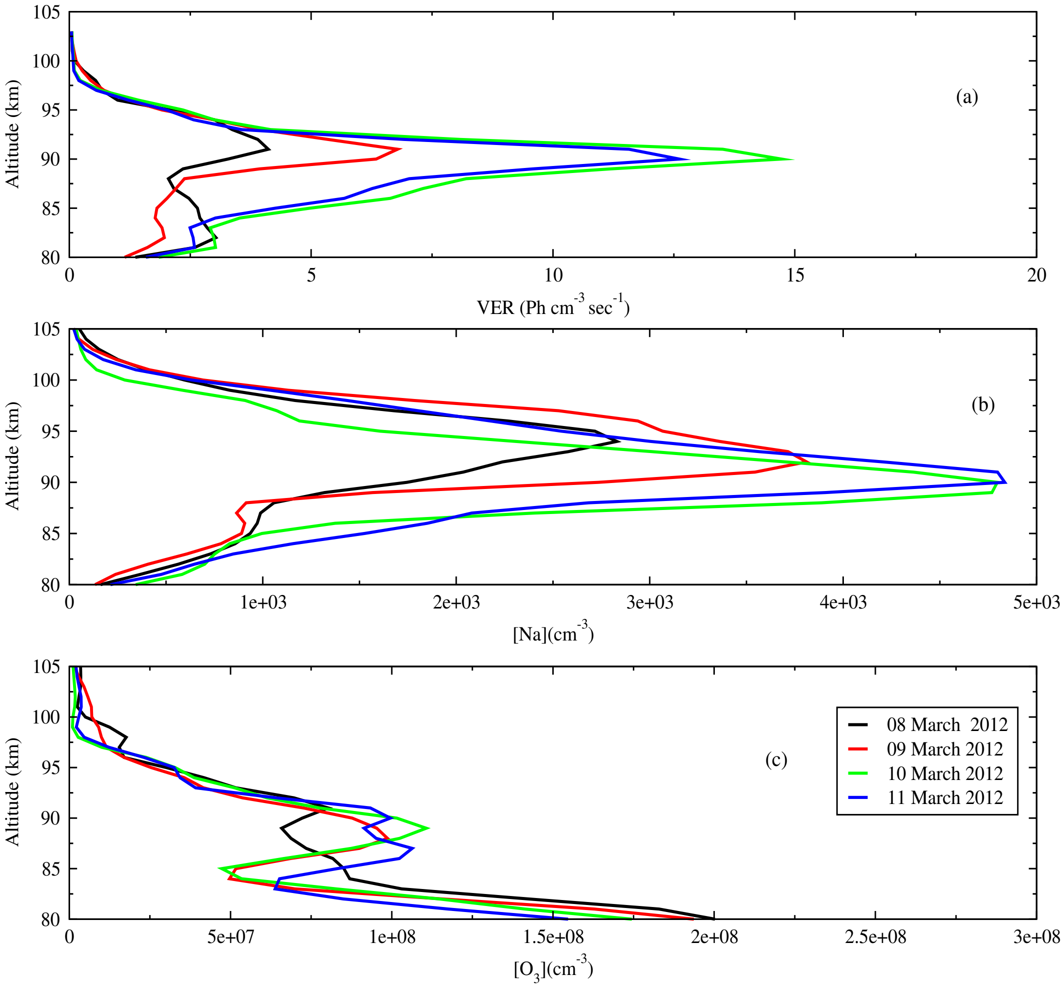

Figure 4.14: Variation of Na VER (a), [Na] (b) and [O_3] during solar proton event (08-11 March, 2012).

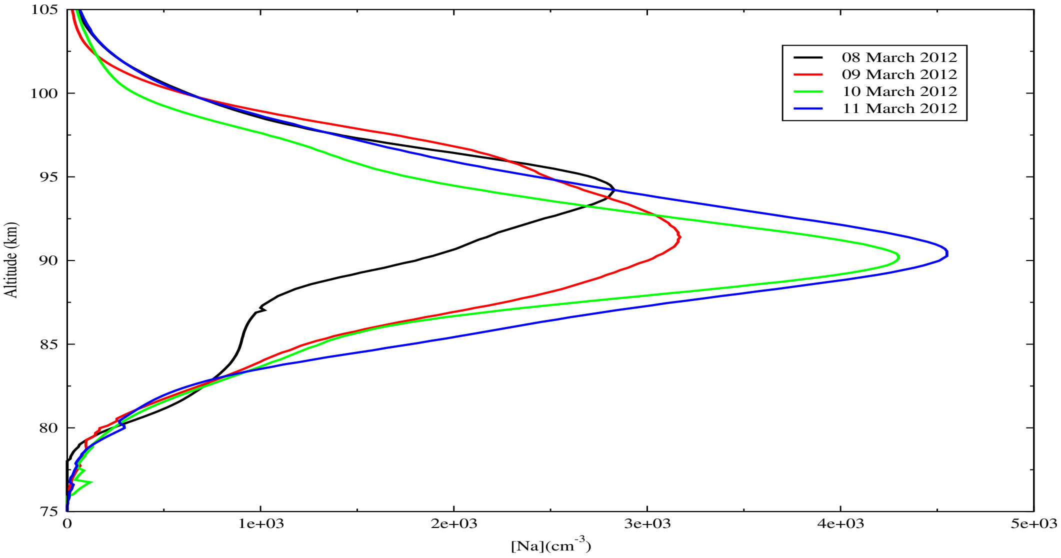

Figure 4.15: Nightly averaged Na density during the solar proton event (08-11 March, 2012).

4.5 Conclusion

The influence of space weather events on sodium density and resulting airglow emission has been studied using lidar observations of Na density and physics based sodium airglow model. The input parameters for the model have been obtained from the NRLMSISE-00, Lidar, and satellite-based instruments. Few cases of extreme geomagnetic storms and solar proton events have been considered during which measurements of Na density are available. The SWE affects the dynamics and chemistry of the atmosphere in terms of change in Ozone and sodium densities. It has been seen that, the sodium and Ozone densities are significantly depleted during the SPE. The reason for this depletion could be due to the enhanced production of ion and electrons which subsequently decrease the Na density by charge exchange reactions. The increased production of NO_x and HO_x are responsible for the decrease of Ozone in the mesospheric altitudes. As a consequence of these fluctuations, it has been seen that the airglow emission rate is depleted during the main phase of the space weather events. The nightly averaged Na densities show a very strong correlation with the progression of geomagnetic storms and solar proton events.

CHAPTER 5

INFLUENCE OF GEOMAGNETIC STORMS ON THE EQUATORIAL IONIZATION AND TEMPERATURE ANOMALIES

5.1 Introduction

The electric field, both in E- and F-region, plays significant roles in the equatorial and low latitudes electrodynamics [233]. The electrodynamic coupling of ionosphere and thermosphere creates peculiar phenomena in low latitude sectors. One of such effect is the equatorial ionization anomaly (EIA). The solar heating and the meridional wind play significant roles in the plasma drifting and in the formation of EIA. It is due to the electrodynamic drift of plasma and diffusion from equator [234]. It is

---

Results presented in this chapter have been reported in a research publication: Gaurav Bharti, T. Bag, M. V. Sunil Krishna, Effect of geomagnetic storm conditions on equatorial ionization anomaly and equatorial temperature anomaly, J. Atmos. Sol-Terr. Phys, 168, 8-20, 2018.

well-known that the fountain effect distributes the plasma with trough at the equator and crests in the regions away from equator in both hemispheres resulting in EIA. The crest of the EIA depends on the strength of E-region electric field and moves towards a farther latitude with the increasing current strength. The vertical drift of plasma in the equatorial region shows diurnal variation with upward drift during day and downward drift during night [235]. Similarly, zonal drift shows diurnal variation by being westward during day and eastward during night [236]. Recent study of Hui et al. [237], using radar from Jicamarca Observatory, observed that the vertical and zonal drifts are season dependent [233, 238, 239]. The vertical upward drift is maximum during September-October. Whereas, maximum daytime westward zonal drift occurs maximum during July-October [237].

The energy and particles precipitation in the polar region during the storm change the structure, dynamics, and the chemistry of atmosphere significantly. The Joule heating and particle precipitation are the two main channels by which the magnetospheric energy enter the ionosphere. This incoming energy results in temperature and pressure gradients which forces the air to move towards the pressure surface [173,174]. Therefore, it results in the composition bulge which propagates to the low and equator sectors with the meridional wind [173, 240, 241]. The meridional wind along with the magnetospheric electric field penetrates towards equatorial latitudes affecting the morphology and dynamics of EIA [242]. This wind and dynamics of the atmosphere create non-uniform distribution in the temperature with a trough at the equator, the equatorial temperature anomaly (ETA) [243–245]. The storm might result either in the enhancement or depletion in EIA but the wind always inhibits [246]. The exact nature of modification entire depends on the local time and it can be said that modification to the equatorial ionization anomaly is produced by the disturbance winds. The strength of east-west electric field in F-region (F-region drift) is also strongly affected by the magnetic activity and is opposite to the quiet-time behaviour [233]. During magnetically active period, the electric field penetrates to the low latitudes. The disturbance electric field along with the dynamo and wind will have a combined effect on the EIA during a storm period. This effect mainly depends on the local time. It may be noted that the electric field will also depend on the local time.

The ETA is a phenomenon more likely to occur during solar maxima during which, the spatial characteristics of ETA are very much similar to EIA. Many times it has been seen that EIA appears as a pre-requisite for the formation of ETA. Unlike EIA, there have been limited studies of ETA owing to the limited thermospheric observations. Since the discovery of ETA in late 1970s [247] various efforts have been made to understand the mechanism of its generation. The earliest efforts pointed out that the anomaly arises from the latitudinal variations in the zonal ion drag related to the EIA in F-region ionization accompanied by the downward vertical wind around the dip equator. Subsequent efforts have considered chemical heating and upward propagating tide to be the additional factors responsible for the formation of ETA [248]. However, the formation mechanism of ETA is still unclear. The uncertainties that exist in the understanding of ETA also puts some limitation on the use ability of global models such as NRLMSISE-00, TIEGCM etc. Earlier model based [249] studies have also suggested that the ETA is sensitive to the fluctuations in geomagnetic activity.

The neutral and charged densities are strongly modulated by geomagnetic storm activity [175,249]. Airglow processes are known to be highly sensitive to the variations in neutral densities. So, it is naturally expected that the variations induced in EIA and ETA by the geomagnetic activity will have a strong signature in the airglow emission patterns. It has been observed that during magnetic quiet time, there is no significant variation in the airglow emission rates. The various parameters such as emission rates of airglow, neutral and charged species densities will form a standard background over which the effects of storms can be easily understood. Hence, studying airglow in geomagnetically disturbed conditions will give us a better understanding of physics and chemistry of airglow. In this study we report how strong geomagnetic activity induced variations in EIA and ETA modulate the airglow emission patterns. For this study we have considered the OI 557.7 nm and $O^+(^2P)$

732.0 nm airglow emissions. The models developed and validated by [92, 250] are used to calculate the volume emission rate (VER). These are global models which can be used to study airglow emissions under different geographic and geophysical conditions [175, 251, 252].

5.2 Model Description

The atomic oxygen airglow emission models (OI 557.7 nm and $O^+(^2P)$ 732.0 nm) have been used to study the EIA and ETA during storm period. The models used here have been verified for various conditions with the satellite based measurements ([92], [250], [251]) These models are most up-to date in terms of various reaction rate coefficients etc. They give us the opportunity to compute variations in airglow emission rates globally or in those situations when there are no direct observations. The full description of the development of comprehensive models for OI 557.7 nm and $O^+(^2P)$ 732.0 nm emissions can be found in the references mentioned above. A brief description of the model used for the present study is as follows.

5.2.1 Atomic oxygen greenline (OI 557.7 nm) airglow emission

The atomic oxygen greenline emission at OI 557.7 nm results due to the following transition.

$$\mathrm{O}(^1S) \rightarrow \mathrm{O}(^1\mathrm{D}) + 557.7\ nm \tag{5.1}$$

The $O(^1S)$ is the metastable state with lifetime 0.91 sec. $O(^1S)$ in the thermosphere is populated by variety of sources. The reaction mechanisms, populating $O(^1S)$, are give below.

- Photo-dissociation of molecular oxygen by Solar EUV photons

$$\mathrm{O}_2 + h\nu(\lambda < 133.25\ nm) \rightarrow \mathrm{O}(^1S) + 557.7\ nm \tag{5.2}$$

The production rate of O(^{1}S) due to the photo-dissociation reaction can be written as,

$$\mathrm{R_{PD}[O(^1S)] = [O_2]} \int \mathrm{F}_{z,\lambda}\ \mathrm{Q}_\lambda\ \sigma_\lambda\ d\lambda \tag{5.3}$$

Where $F_{z,\lambda}$ is the solar EUV flux at altitude z and at wavelength λ. Q_λ is the quantum yield at wavelength λ and σ_λ the photo absorption cross-section of O_2.

- Three body recombination reaction

Three body recombination reaction also makes a significant contribution to the production of O(^{1}S) state. This source was extensively studied in nightglow and thought to proceed via Chapman reaction [253].

$$\mathrm{O(^3P) + O(^3P) + O(^3P) \rightarrow O_2 + O(^1S)} \tag{5.4}$$

However, it is generally accepted that the production of O(^1S) is a two step mechanism as proposed by Barth [254]. This reaction proceeds in the presence of a third body M as

$$\mathrm{O(^3P) + O(^3P) + M} \xrightarrow{\gamma k_1} \mathrm{O_2^* + M} \tag{5.5}$$

- Dissociative recombination of O_2^+.

$$\mathrm{O_2^+ + e}_{th} \xrightarrow{k_4} \mathrm{O(^1S) + O} \tag{5.6}$$

The corresponding production rate of O(^{1}S) can be written as,

$$\mathrm{R_{DR}[O(^1S)]} = \beta_4 k_4 [O_2^+][\mathrm{e}] \tag{5.7}$$

Here, β_4 is the quantum yield and k_4 is the reaction rate coefficient.

- Photoelectron impact on atomic oxygen.

$$\mathrm{O(^3P) + e}_{ph} \rightarrow \mathrm{O(^1S) + e}_{ph} \tag{5.8}$$

The production rate of $\mathrm{O(^1S)}$ due to photoelectron impact on atomic oxygen can be written as,

$$\mathrm{R_{PE}[O(^1S)] = [O]} \int_{\mathrm{E}_{th}}^{\infty} \Phi(\mathrm{E_s, z}, \alpha)\sigma\mathrm{O(^1S)(E_s)dE_s} \tag{5.9}$$

Where, [O] is the atomic oxygen number density, $\Phi(E_s, z, \alpha)$ is the photo electron flux, E_s is the photoelectron energy, z is the altitude and α is the solar zenith angle. $\sigma_{O(^1S)}(E_s)$ is the photoelectron excitation cross-section of $\mathrm{O(^1S)}$.

- Collisional deactivation of $\mathrm{N_2(A\Sigma_u^+)}$ with atomic oxygen.

$$\mathrm{N_2 + e_{ph} \rightarrow N_2(A\Sigma_u^+) + e}_{ph} \tag{5.10}$$

$$\mathrm{N_2(A\Sigma_u^+) + O(^3P)} \xrightarrow{k_7} \mathrm{N_2 + O(^1S)} \tag{5.11}$$

The production rate of $\mathrm{O(^1S)}$ is given as,

$$\mathrm{R_{[N_2A]}[O(^1S)]} = \beta_7 k_7 \mathrm{[N_2(A\Sigma_u^+)][O]} \tag{5.12}$$

Here, β_7 and $\mathrm{k_7}$ denote the quantum yield and reaction rate coefficients respectively.

The $\mathrm{O(^1S)}$ produced due to the above reaction mechanisms is quenched by interaction with various atmospheric species as follows,

$$\mathrm{O(^1S) + (O_2, O)} \xrightarrow{k_8, k_9} \mathrm{O(^3P) + (O_2, O)} \tag{5.13}$$

$$\mathrm{O(^1S)} \xrightarrow{\mathrm{A_{10}}} \mathrm{O(^1D)} + 557.7\ \mathrm{nm} \tag{5.14}$$

$$\mathrm{O(^1S)} \xrightarrow{\mathrm{A_{11}}} \mathrm{O(^3P)} + h\nu(total) \tag{5.15}$$

From above reactions the quenching factor can be written as,

$$\mathrm{Q} = \frac{\mathrm{A_{10}}}{\mathrm{A_{11}} + k_8[\mathrm{O_2}] + k_9[\mathrm{O}]} \tag{5.16}$$

Here, [X] indicate the number density of corresponding species, while $\mathrm{A_{10}}$ & $\mathrm{A_{11}}$ are the Einstein's coefficients. From the above mention reactions the volume emission rate (VER) of $\mathrm{O(^1S)}$ can be written as,

$$\mathrm{VER[O(^1S)]} = \mathrm{Q} \cdot \mathrm{R[O(^1S)]} \tag{5.17}$$

$\mathrm{R[O(^1S)]}$ shows the total production rate due to all above reactions.

The cross-sections, and quantum yields for the above mention reaction have been taken from Sunil et al. [92] in the present study. Hence, We have not listed here. On the other hand the Einstein's coefficients and reaction rate coefficients have been obtained from the theoretical studies and experimental studies reported in literature. These values are mention in the Table (5.1).

5.2.2 Atomic oxygen $\mathrm{O^+(^2P)}$ 732.0 nm airglow emission

The atomic oxygen $\mathrm{O^+(^2P)}$ 732.0 nm is a week emission. The complete details of model development and the validation of the same using satellite data is given in Sunil et al. [250]. This emission generally peaks at around 200-250 km. This, is a doublet feature at 732.0 nm and 733.0 nm, emission results due to the following transition.

Table 5.1: Reaction rate coefficients for 557.7 nm emission

Reaction	Rate constants	Value	Reference
$O_2^+ + e_{th} \rightarrow O(^1S) + O$	k_4	$1.6\times10^{-7}(300/T_E)^{0.5}$	[255]
$N_2(A\Sigma_u^+) + O(^3P) \rightarrow N_2 + O(^1S)$	k_7	$4.8\times10^{-11}(T_N/298)^{0.5}$	[256]
$O(^1S) + O_2 \rightarrow O(^3P) + O_2$	k_8	$4.0\times10^{-12}exp(-865/T_N)$	[257]
$O(^1S) + O \rightarrow O(^3P) + O$	k_9	2.0×10^{-14}	[258]
$O(^1S) \rightarrow O(^1D) + 557.7$ nm	A_{10}	1.18	[259]
$O(^1S) \rightarrow O(^3P) + h\nu(total)$	A_{11}	1.35	[259]

Table 5.2: Reaction rate coefficients for 732.0 nm emission

Reaction	Rate constants	Value	Reference
$O^+(^2P) + O \rightarrow O^+ + O$	k_O	5.2×10^{-11}	[260]
$O^+(^2P) + N_2 \rightarrow O^+ + N_2^*$	k_{N_2}	4.8×10^{-10}	[261, 262]
$O^+(^2P) + e \rightarrow O^+(^2D,^4S) + e$	k_e	$1.89\times10^{-7}(T_e/300)^{0.5}$	[263]

$$\mathrm{O^+(^2P)} \xrightarrow{\mathrm{A_{12}}} \mathrm{O^+(^2D,^4S)} + \mathrm{h}\nu(732.0\ \mathrm{nm}, 733.0\ \mathrm{nm}) \tag{5.18}$$

The $O^+(^2P)$ is a metastable state with life time of 4-5 sec. There are two sources for the production of $\mathrm{O^+(^2P)}$ 732.0 nm emission.

- Photoionization excitation of atomic oxygen by solar EUV radiation

$$\mathrm{O} + \mathrm{h}\nu(\lambda < 66.6\ \mathrm{nm}) \rightarrow \mathrm{O^+(^2P)} \tag{5.19}$$

- Photoelectron impact ionization of atomic oxygen

$$\mathrm{O} + \mathrm{e_{ph}} \rightarrow \mathrm{O^+(^2P)} + 2\mathrm{e} \tag{5.20}$$

The production rates due to the above reaction mechanisms can be written as,

$$\mathrm{R1(Z)} = [\mathrm{O}]\Sigma_\lambda \mathrm{I_z}(\lambda, \alpha)\sigma_{\mathrm{O^+(^2P)}}(\lambda) \tag{5.21}$$

and

$$\mathrm{R2(Z)} = [\mathrm{O}]\int_{\mathrm{E_{th}}}^{\infty} \sigma_{\mathrm{e}}(\mathrm{E})\Phi(\mathrm{E}, \mathrm{Z}, \alpha)\mathrm{dE} \tag{5.22}$$

Here, [O] denotes the density of atomic oxygen, $I_z(\lambda, \alpha)$ and $\Phi(E, Z, \alpha)$ are the solar EUV flux and photoelectron flux at wavelength λ and at solar zenith angle α respectively. $\sigma_{O^+(^2P)}(\lambda)$ is the photoionization cross-section and $\sigma_e(E)$ is the photoelectron cross-section. E_{th} is the threshold energy for the production of $O^+(^2P)$.

The $O^+(^2P)$ produced by above reaction mechanisms is quenched by its interaction with atmospheric species such as, [O], [e], and [N_2]. The quenching mechanisms are give as,

$$\mathrm{O^+(^2P)} + (\mathrm{O}, \mathrm{N_2}) \xrightarrow{\mathrm{k_O}, \mathrm{k_{N_2}}} \mathrm{O^+} + (\mathrm{O}, \mathrm{N_2^*}) \tag{5.23}$$

$$\mathrm{O^+(^2P) + e \xrightarrow{k_e} O^+(^2D,^4S) + e} \tag{5.24}$$

Hence, the quenching factor can be written as,

$$\mathrm{Q[O^+(^2P)] = \frac{A_{2P}}{A_{2P} + k_O[O] + k_{N_2}[N_2] + k_e[e]}} \tag{5.25}$$

where [X] denotes the corresponding number density, A_{2P} is the loss frequency of $\mathrm{O}^+(^2P)$ due to all radiative transitions. Its values has been taken as 0.281 sec^{-1}. The values of the reaction rate coefficients are summarized in Table (5.2).

Taking into account above production and loss mechanisms, the VER for $\mathrm{O^+(^2P)}$ 732.0 nm can be written as,

$$\mathrm{VER[O^+(^2P)] = 0.781 \cdot Q[O^+(^2P)] \cdot R(Z)} \tag{5.26}$$

Where R(Z) is the total production of 732.0 nm (i.e. R(z)=R1(Z)+R2(Z)).

5.3 Results and Discussion

In the given work, we have mention 4 intense geomagnetic storms during the ascending phase of solar cycle 24 over a low latitude at 190°E longitude such that the geomagnetic equator nearly coincides with the geographic equator. The details of these storms are given as follows.

S No.	Notation	Duration	Minimum Dst Index
1	storm1	25-28 September 2011	-118 nT
2	storm2	16-18 March 2013	-132 nT
3	storm3	23-26 October 2011	-147 nT
4	storm4	14-17 July 2012	-127 nT

The airglow emission rates have been calculated at three different altitudes during the storm period by incorporating the densities and temperature as discussed in the model section. The variations induced in EIA and ETA by the geomagnetic storms are discussed by the means of their effect on OI 557.7 nm and $O^+(^2P)$ 732.0 nm airglow emission rates. The effects of storm conditions are understood by correlating observed variation in airglow emissions to the parameters associated with EIA and ETA which are most likely to be influenced by the onset of geomagnetic storms.

5.3.1 Storm time EIA & $O^+(^2P)$ 557.7 nm emission

The fluctuation in Dst index, latitudinal neutral densities, and VER of OI 557.7 nm greenline emission during storm1 is shown in Figure 5.1. The geomagnetic storm commenced at nearly 17:00 UT on 26 September reaching a minimum value of Dst within twelve hours as shown in Figure 5.1(a). The latitudinal variation in the O, O_2, N_2 and VER during storm1 at 150 km is shown in Figure 5.1(b-e) respectively. It can be seen from Figure 5.1(b) that the atomic oxygen density shows significant enhancement during the main phase of the storm to a relative high order over the equator as compared to both the hemispheres. Also the southern hemispheric oxygen density is slightly higher than the northern hemisphere. The atomic oxygen density returns approximately to its base value during the recovery phase. A composition bulge occurs in the polar region which then propagates to the low latitudes with the meridional wind [235, 241]. $[O_2]$, and $[N_2]$ also show similar enhancement to the [O]. However, the O_2, and N_2 number densities have a higher values on either sides of equator (Figure 5.1 (c & d)). In effect we can see the resultant enhancement of O/N_2 at low latitudes. Similar variation in the equatorial thermospheric anomaly during geomagnetic storm conditions at the equinox has also been reported by Lei et al. [249] using TIEGCM simulation. The fluctuation induced by the storm in the O, O_2, and N_2 would affect the VER of green line emission by influencing the chemical scheme of the $O(^1S)$. It can be seen from Figure 5.1(e) that at any given latitude the VER of 557.7 nm is positively correlated to the Dst index. The variations in neutral densities as seen in Figure 5.1(b-d) are negatively correlated with the progression of the storm at any latitude. The interesting feature about these variations is that the variation

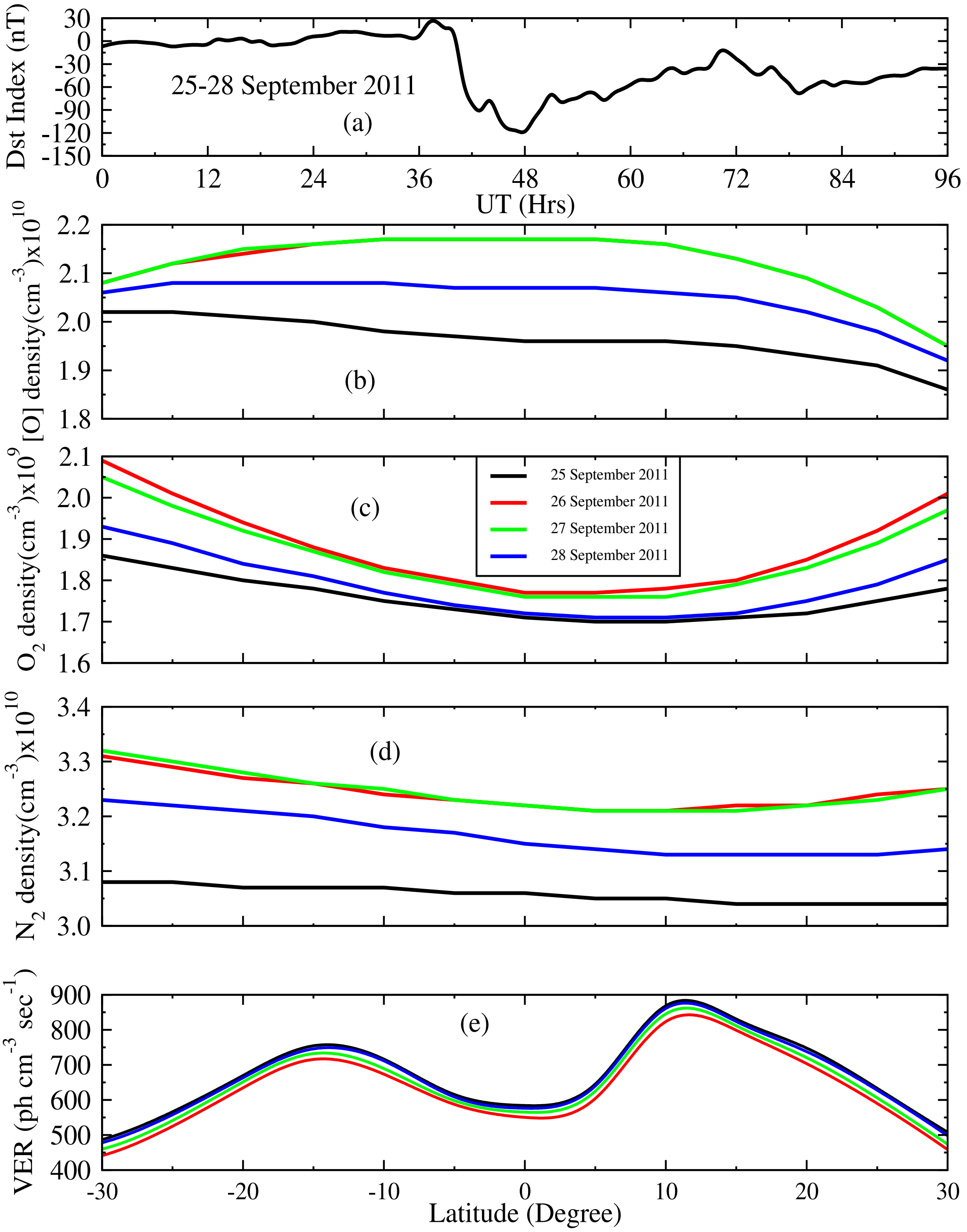

Figure 5.1: Variation of Dst Index (panel a), [O] (panel b), [O_2] (panel c), [N_2] (panel d), and VER of O(^{1}S) (panel e) with latitude during storm1 at 150 km.

is not uniform across the latitudes and is different for each of O, O_2 and N_2 unlike what is seen in the variation of volume emission rate (Figure 5.1(e)). These variations in neutral densities can affect the VER by the means of production and quenching of O(^1S). The relative competition between the production and quenching processes driven by fluctuations in neutral species will determine the final VER. reaction (5.16) shows that the quenching would be higher due to the enhancement in the number densities, hence the depletion is seen in the VER at the equator (Figure 5.1 e). It is noticeable that the VER shows a crest at around 12° latitude in both the hemispheres with a trough near the equator with the northern hemispheric peak slightly higher in magnitude.

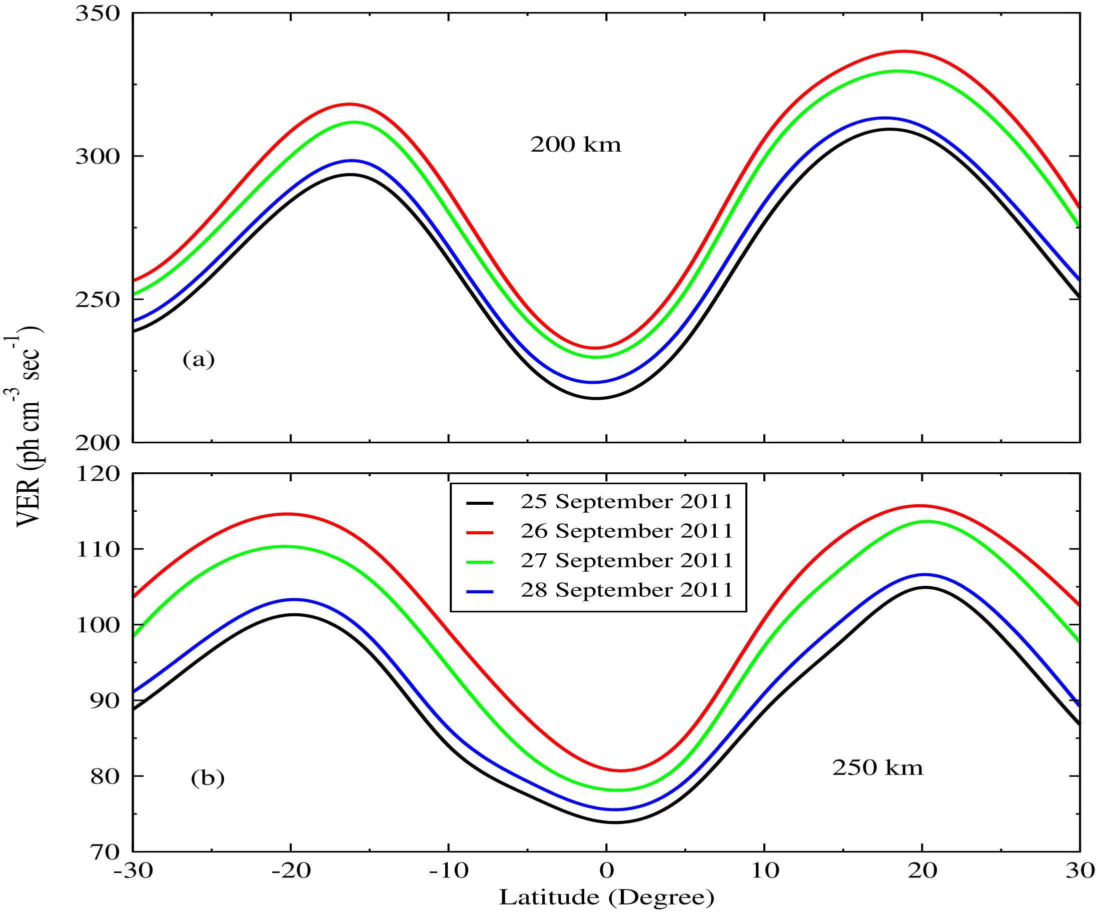

Figure 5.2: Latitudinal variation of VER of O(^{1}S) at 200 km (panel a), and 250 km (panel b) during storm1.

The latitudinal variation in the VER of O(^{1}S) during storm1 at 200 and 250 km is shown in Figure 5.2(a & b), respectively. The VER has been calculated at

200 km and 250 km during the storm period using the densities obtained from the NRLMSISE-00 and IRI-2012. It is noticeable that the VER at both 200 and 250 km show negative a correlation with the Dst index at any given latitude. This negative correlation of VER with Dst index could be due to the influence of the quenching mechanism. Although the densities of the neutral species at these altitudes show a similar enhancement to that found at 150 km but the concentration of neutral species is very less at higher altitudes. As a result the quenching factor becomes high resulting in a heavy loss in the net volume emission rate. This fact is clear if we compare Figure 5.1(e) with Figure 5.2(a & b). The equatorial ionization anomaly also shows a strong signature in the VER profile of $O(^1S)$. The EIA crest in the northern hemisphere has a higher value compared to the southern hemisphere. This hemispheric difference in magnitude of volume emission rate becomes less pronounced while going towards higher altitudes. The poleward movement of the EIA crest with increasing altitude can be clearly seen from the Figures 5.1(e), 5.2(a & b). This poleward movement is consistent with the earlier reports by Balan et al. [264]. The latitudinal trend of volume emission rate with a dip at equator and crests on either sides of equator is mainly due to the electron density profile which shows a similar variation from pole to pole. This fact can be further confirmed by the electron dominated source mechanisms of $O(^1S)$ emission. Figure 5.1(e), 5.2(a & b) confirm the effect of storm induced variations in the electron density and temperature on the latitudinal variation of volume emission rates. The dissociative recombination of O_2^+ is a dominant source for the production of greenline emission. The rate of production from this source is mainly dependent on the available density of the electrons. From this we can say that the latitudinal variation induced in a greenline airglow is positively correlated to the structure of EIA. The day-to-day variations in the VER is also positively correlated to the strength of EIA during the storm period. The poleward movement of the EIA crest can be attributed to the conversion of plasma fountain into a super fountain during an intense storm due to the prompt penetration of electric field.

Figure 5.3 shows the variation of Dst Index, latitudinal fluctuation of O, O_2, N_2,

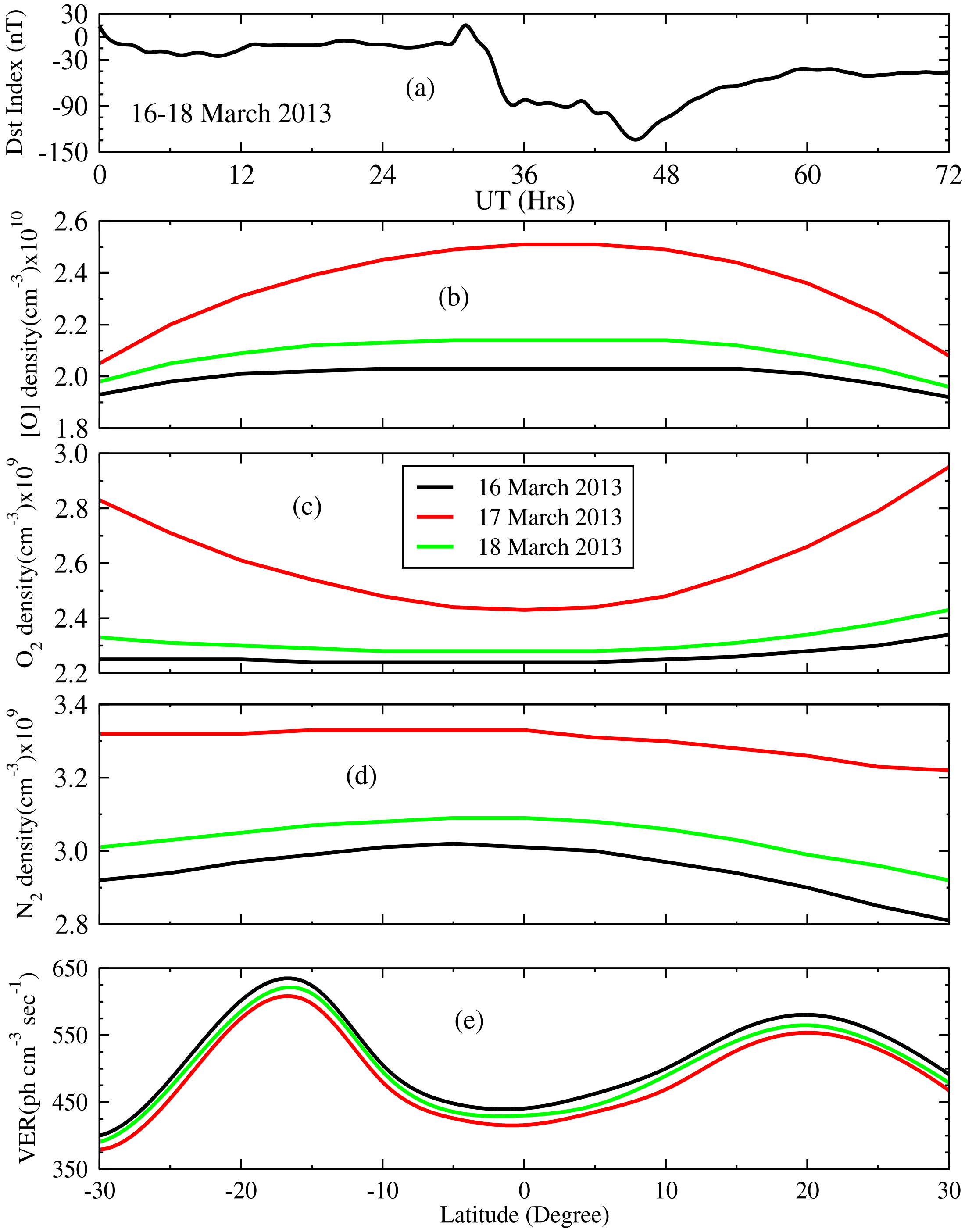

Figure 5.3: Variation of Dst Index (panel a), [O] (panel b), [O_2] (panel c), [N_2] (panel d), and VER of O (^{1}S) (panel e) with latitude during storm2 at 150 km.

and VER of O(^{1}S) at 150 km during storm2. The storm2 commenced at around 1 UT on March 16, 2013 and reached a minimum value of Dst (-132 nT) at around 21

UT on 17 March, 2013 as shown in Figure 5.3(a). The latitudinal variation in the density of [O] is shown in Figure 5.3(b). The [O] shows a strong enhancement near the equator during the main phase of the storm2. [O_2] and [N_2] as shown in Figure 5.3(c & d) are also perturbed by the onset of the geomagnetic storm and recover back to the pre-onset values as the storm recedes. However, one interesting feature of these variations is that the maximum variation in O_2 density is observed towards the mid-latitudes unlike the variation seen in [O]. The observed variation in VER is also similar to what has been discussed for storm1 (Figure 5.1). The southern hemispheric EIA crest shows a higher value compared to the northern EIA crest which could be due to the effect of hemispheric wind.

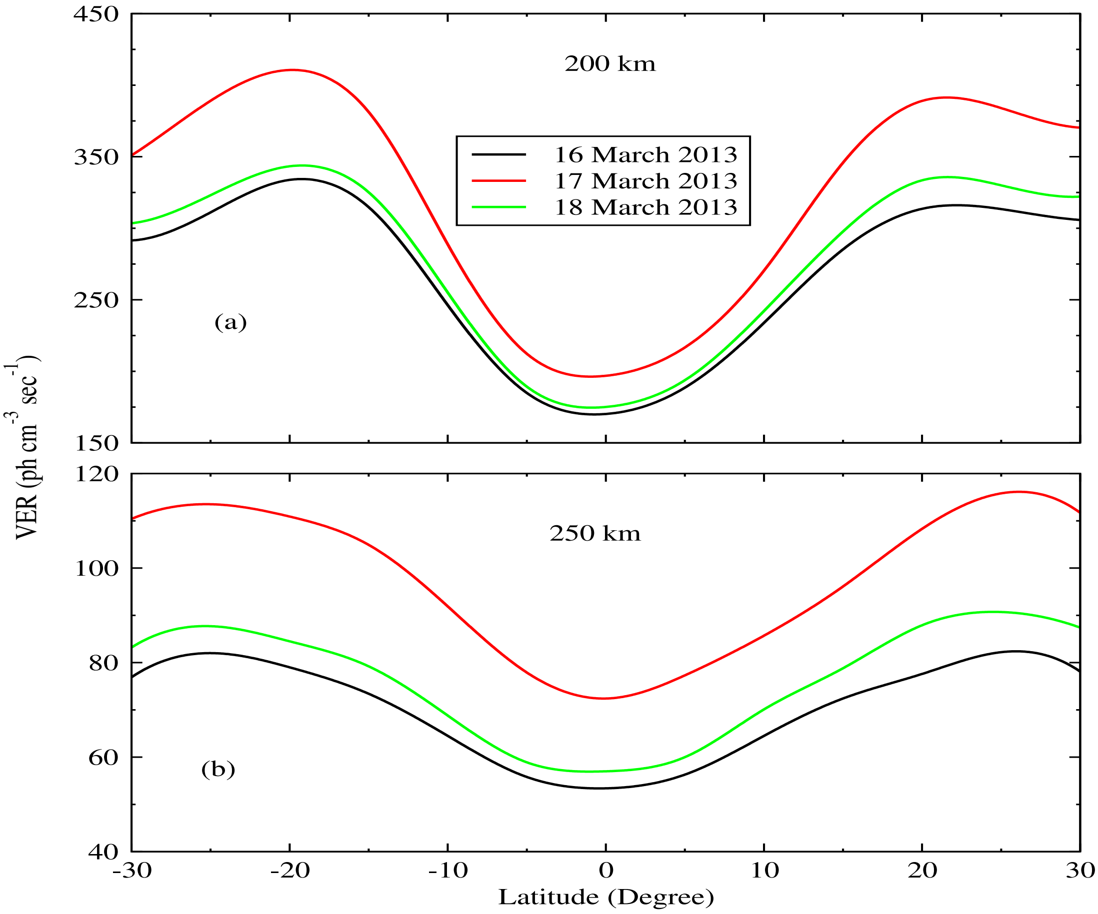

Figure 5.4: Latitudinal variation of VER of O(^1S) at 200 km (panel a), and 250 km (panel b) during storm2.

The latitudinal variation in the volume emission rate of O(^{1}S) at two different heights 200 and 250 km during the storm2 is shown in Figure 5.4(a & b). At these two heights the VER increases during the main phase due to the dominating production by enhanced neutral densities. The poleward movement of EIA crest is also observed during storm2.

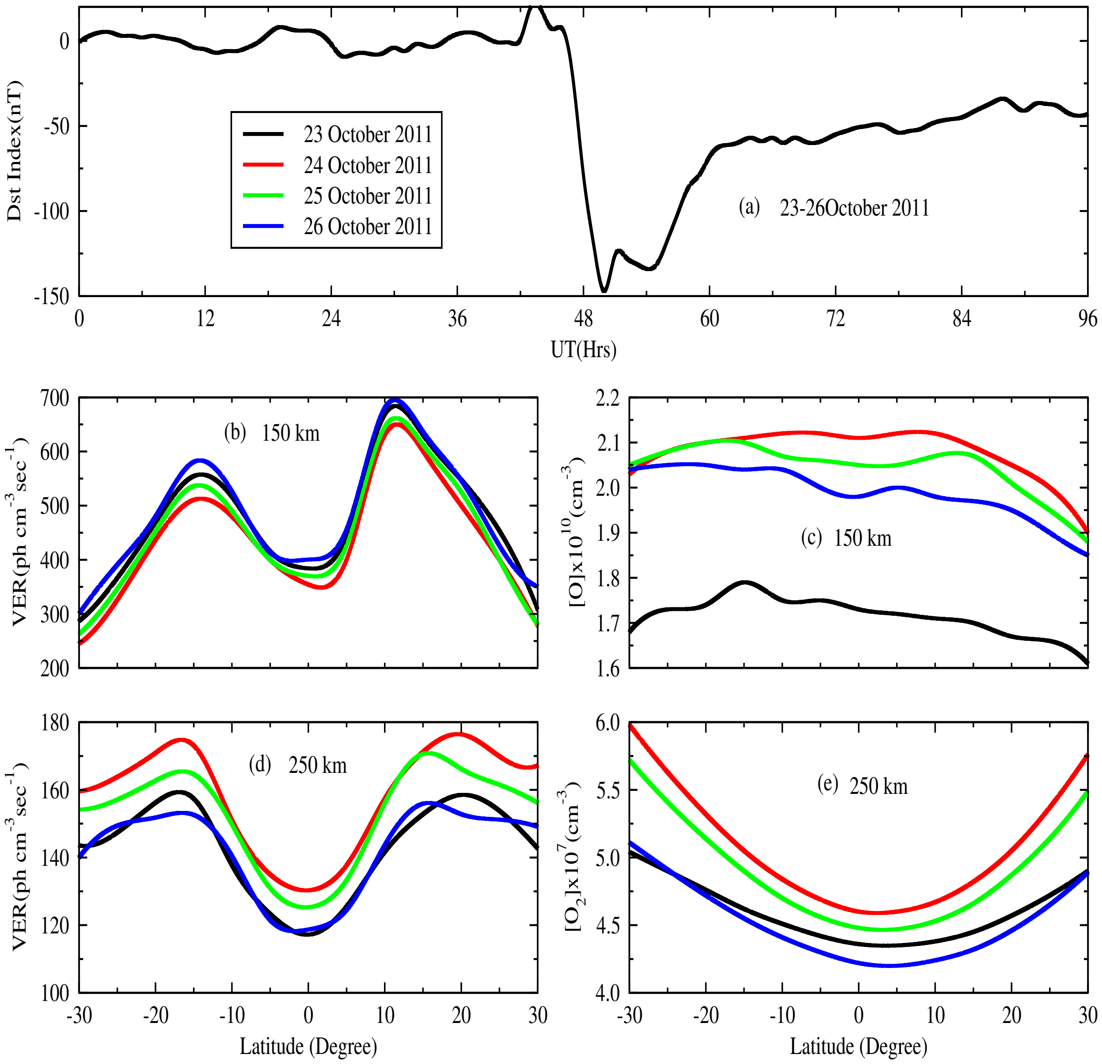

Figure 5.5: Variation of Dst Index (panel a), Latitudinal variation of O(^{1}S) VER at 150 km (panel b) and 250 km (panel d), [O] abundance at 150 km (panel c), [O$_2$] abundance at 250 km (panel e) during storm3

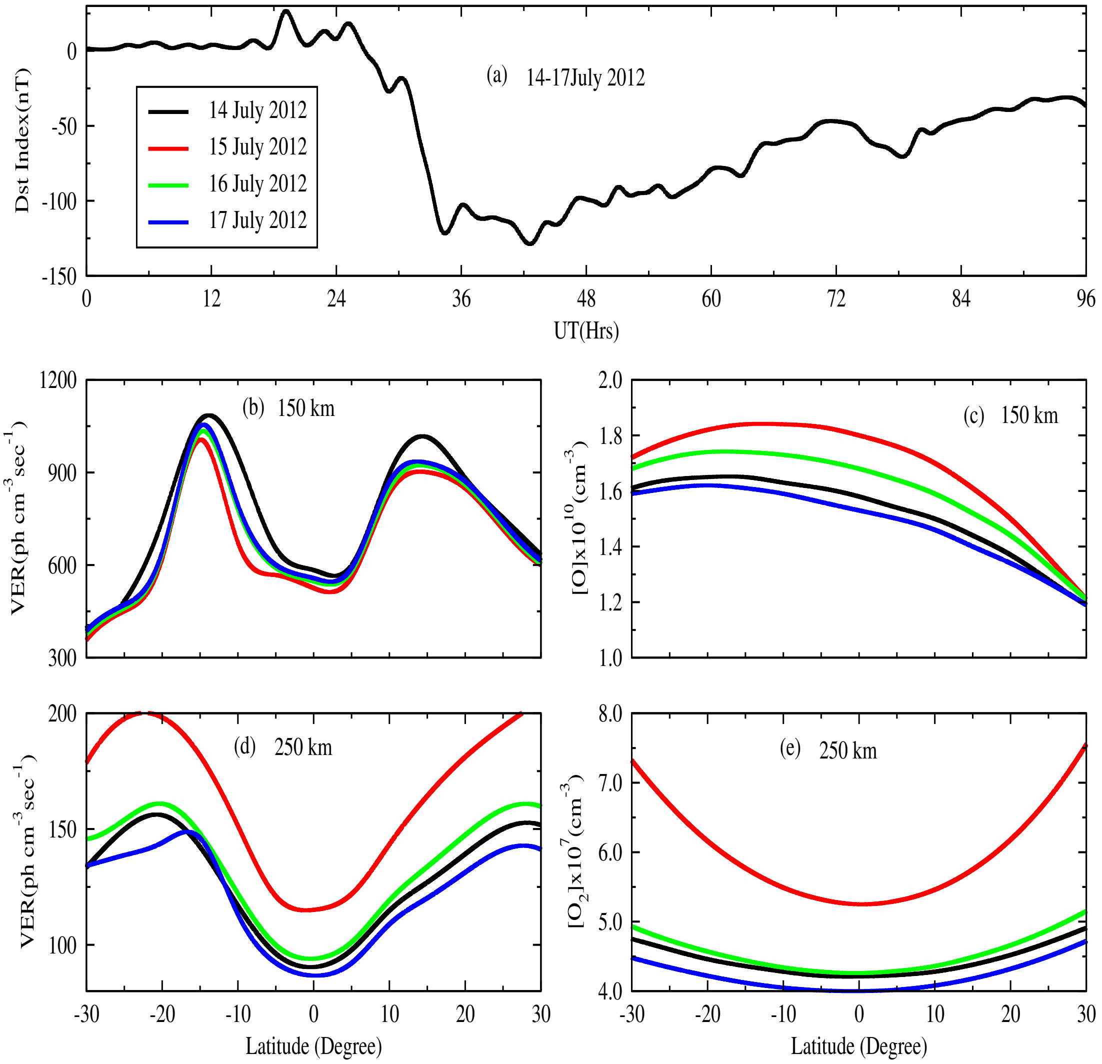

Figure 5.6: Variation of Dst Index (panel a), Latitudinal variation of O(^{1}S) VER at 150 km (panel b) and 250 km (panel d), [O] abundance at 150 km (panel c), [O_2] abundance at 250 km (panel e) during storm4.

5.3.2 Storm time EIA & 732.0 nm emission

In order to see if the nature of results does not change with other storm conditions, we have performed similar set of calculations for two more storms. During the ascending phase of solar cycle 24 nearly 17 intense geomagnetic storms (<-100 nT) have occurred. Out of these, we have taken four intense storms to make the study more general and to establish the nature of correlation between airglow and ion-neutral species. The two more conditions chosen for the study are 23-26 October, 2011 (storm3, Dst:-147 nT) and 14-17 July, 2012 (storm4, Dst:-127 nT). Figures (5.5 & 5.6) show the variation of Dst index along with the latitudinal profile of O(^1S)VER at 150 and 250 km altitude. The neutral abundances of [O] and [O_2] are shown the panels (c & e) respectively in Figures (5.5 & 5.6). The nature of these fluctuations is very much similar to what has been seen in the case of storms 1 & 2. It can be noticed that the volume emission rate is positively correlated with the progression of storm at low altitudes and negatively correlated at high altitudes. The variation in neutral abundances of O and O_2 are shown in panels (c) and (e) respectively. Here, it is worth mentioning that the VER follows the fluctuations in [O] density at low altitude (<100 km) attributing to the fact that three body recombination reaction reaction (5.5) is the main source of production for greenline emission in the upper mesosphere region. While, at high altitudes the VER mainly depends on the available [O_2] density due to the dissociative recombination process reaction (5.6). At high altitudes, the maximum contribution to the total production rate is due to dissociative recombination process which is driven by the available electron density and the O_2^+ abundance. The other source for the production of O(^{1}S) is the photo-electron impact on atomic oxygen. This process will also depend on the available density of electron. Hence we see the double hump structure in the latitudinal profile of VER.

The EIA affects the dynamics and composition of the E- and F- regions. The atomic oxygen is a highly reactive species and the density of the same fluctuates highly in these regions. The atomic oxygen airglow emission at 732.0 nm occurs in the thermospheric altitudes (above 200 km) and has been suggested to be a potential indicator to monitor atomic oxygen density at these altitudes. This is a very weak emission and at the same time very sensitive to the variations in neutral densities in terms of both production and loss. The latitudinal variation in the volume emission rate of 732.0 nm airglow emission at three different altitudes (220, 250, and 280 km) are shown in Figure 5.7(b-d) along with Dst index (Figure 5.7 a). The variations in neutral species with the storm1 and storm2 are already discussed in Figure 5.1(b-d) and Figure 5.3(b-d). The first observation about the latitudinal variation is that the

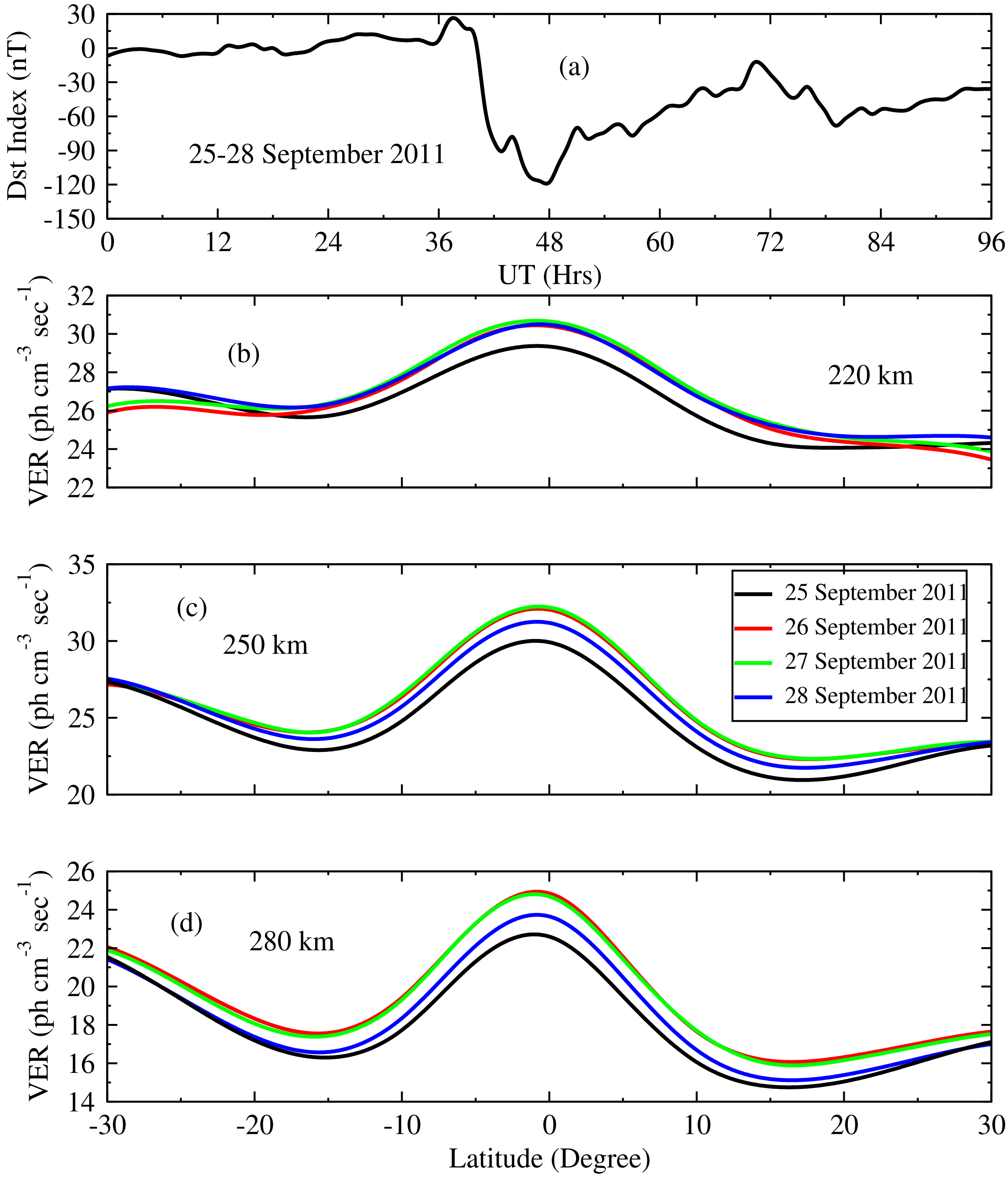

Figure 5.7: Variation of Dst Index (panel a), VER at 220 km (panel b), 250 km (panel c), and 280 km (panel d) with latitude for OII 732.0 nm during storm1.

peak VER occurs near the equator for all the altitudes unlike the greenline emission. The volume emission rate however increases during the storm period showing a negative correlation with the Dst index of the storm. The maximum variation in VER is seen on 27 September between 15 degree latitude in both hemispheres. It can be noticed that the maximum enhancement in VER occurred at different phases of storm for the three different altitudes. The latitudinal variation is anti-correlated to the EIA. Thus we can see that the emission rate is minimum at the EIA crests and maximum at the equator. This is mainly because of the quenching factor which is indirectly Proportional to the electron density. However, the day to day variations in the 732.0 nm emission during the storm period are positively correlated with the variations induced in the strength of EIA during the same period.

The variation of Dst index, and the VER of 732.0 nm emission at different altitudes during storm2 are shown in Figure 5.8. The VER shows enhancement throughout the main phase of storm at all altitudes unlike variation seen during storm1 (Figure 5.7). The enhancement in the VER during the main phase is more pronounced at higher altitudes. The effect of quenching on 732.0 nm emission and the lack of the EIA crest in the latitudinal profile of VER is discussed in more detail using Figures (5.9 & 5.10).

It is noticeable from Figures (5.7 & 5.8) that the VER doesn't show anomaly on the lines of EIA in the equatorial region like the greenline (OI 557.7 nm) airglow emission (Figure 5.1 & 5.2). To understand this unexpected behaviour of OII 732.0 nm airglow, we have analysed the production sources along with the quenching mechanism. It can be noticed from reaction (5.21 & 5.22) that the production rate of OII 732.0 nm is proportional to the densities of electron, atomic oxygen and EUV fluxes (Calculated using SIP, V2.38). The rate at which excited $O^+(^2P)$ is quenched is indirectly proportional to the densities of [e], [O] and [N_2]. The [e] is the main contributor to the net quenching factor. As a result we see the effect of quenching on the net VER. Hence, there is a minimum VER on either sides of equator appearing to be anti-correlated to the latitudinal profile of electron density. At the same time the high value of atomic oxygen density available at the equatorial region also maximizes production of $O^+(^2P)$. A combined effect of these two factors results in the observed latitudinal variation of 732.0 nm emission rate. It may appear that there is no signature of EIA crest on the 732.0 nm emission latitudinal profile but the anti-correlation

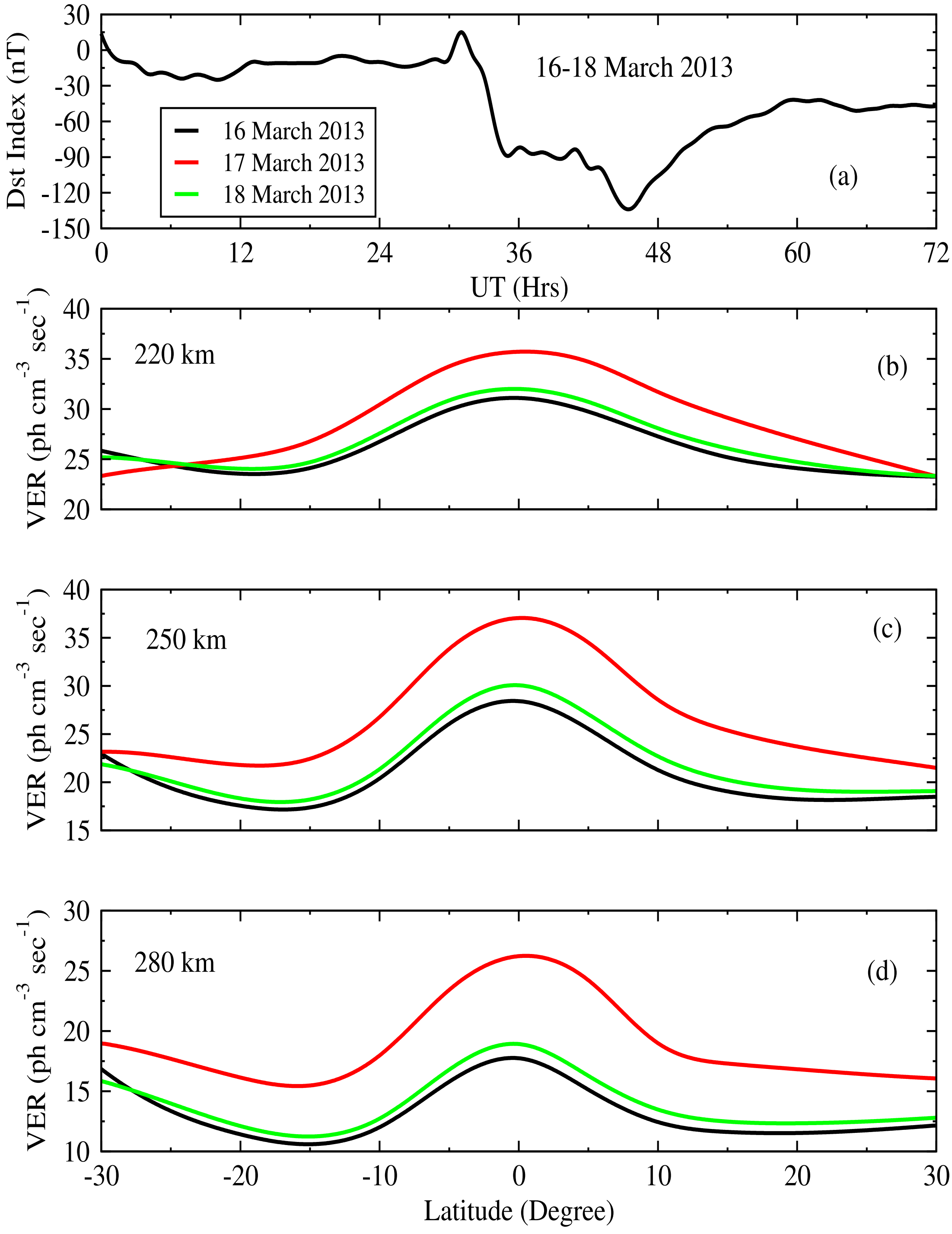

Figure 5.8: Variation of Dst Index (panel a), VER at 220 km (panel b), 250 km (panel c), and 280 km (panel d) with latitude for OII 732.0 nm during storm2.

between electron density and quenching is what decides the latitudinal variation of 732.0 nm emission.

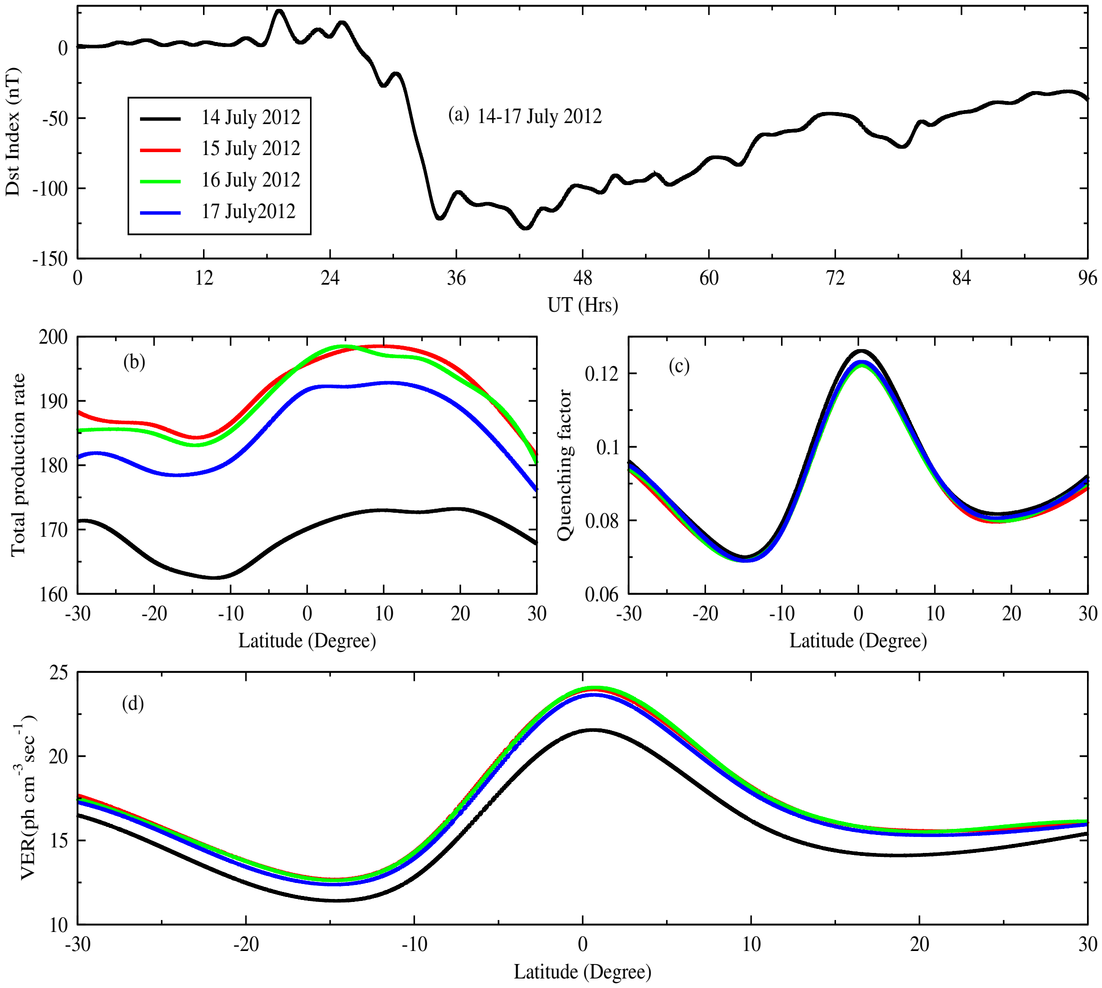

Figure 5.9: Variation of Dst Index (panel a), latitudinal variation of total production at 280 km (panel b), quenching factor (panel c), and total VER (panel d) for OII 732.0 nm during storm3.

The latitudinal variation in the VER of 732.0 nm emission during storms 3 and 4 are shown in Figures (5.9 & 5.10), respectively. The panel (a) in both the figures show the variation of Dst during the storm. Panels (b & c) show the total production and quenching rates. Whereas panel (d) shows the net volume emission rate (5.26). It can be seen that the nature of variation observed in VER in storms 3 and 4 are similar to storms 1 and 2. However, the electron density dominated quenching processes will eventually decide the anti-correlation between the latitudinal EIA and VER profiles

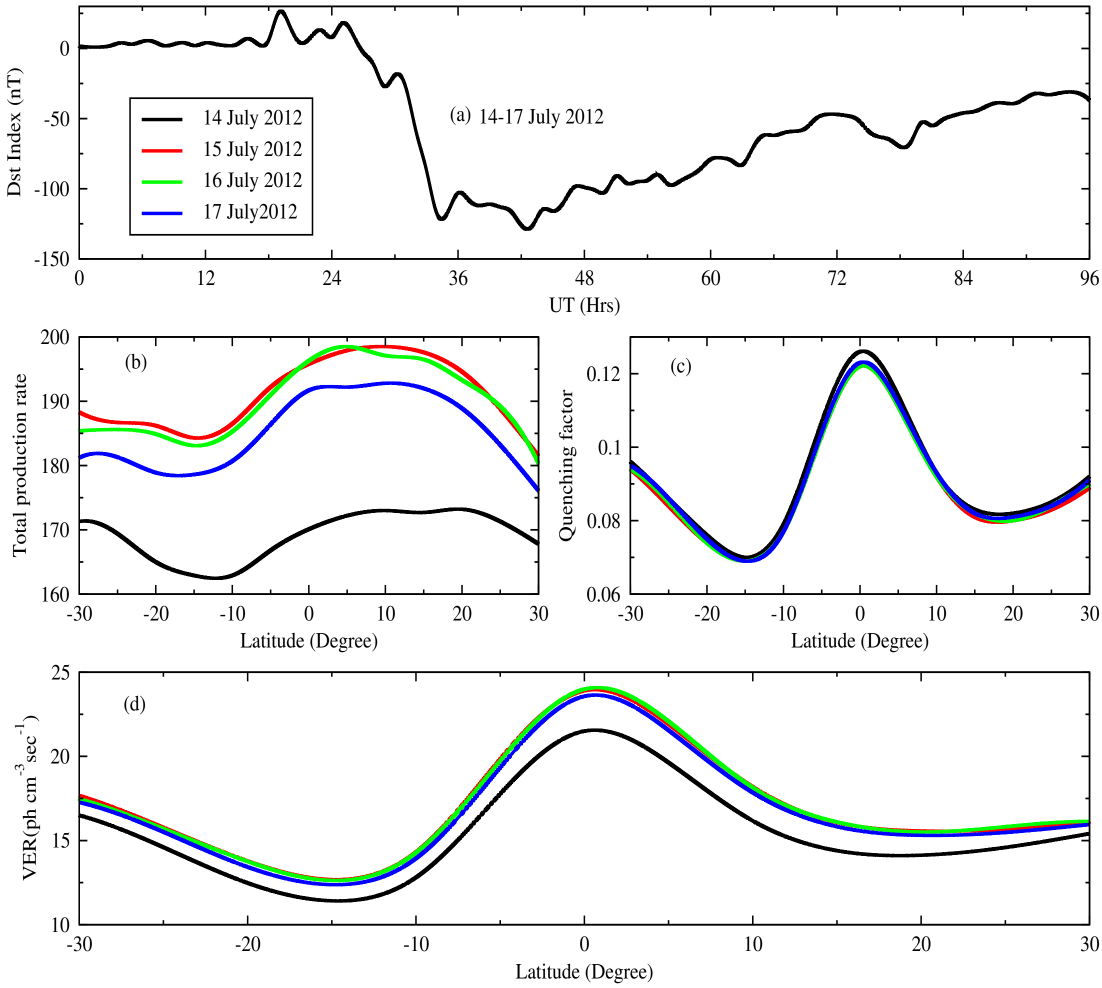

Figure 5.10: Variation of Dst Index (panel a), latitudinal variation of total production at 280 km (panel b), quenching factor (panel c), and total VER (panel d)for OII 732.0 nm during storm4.

as discussed in the above paragraph.

5.3.3 Equatorial temperature anomaly (ETA)

The neutral temperature of atmosphere is a very important parameter which determines the emission rates of various airglow emissions by the means of reaction rate coefficients etc. Figures 5.11 and 5.12(b-d) shows the latitudinal variation of neutral temperature at different heights (150, 200 and 250 km). There are two important aspects worth noticing about this variation under the effect of geomagnetic storm.

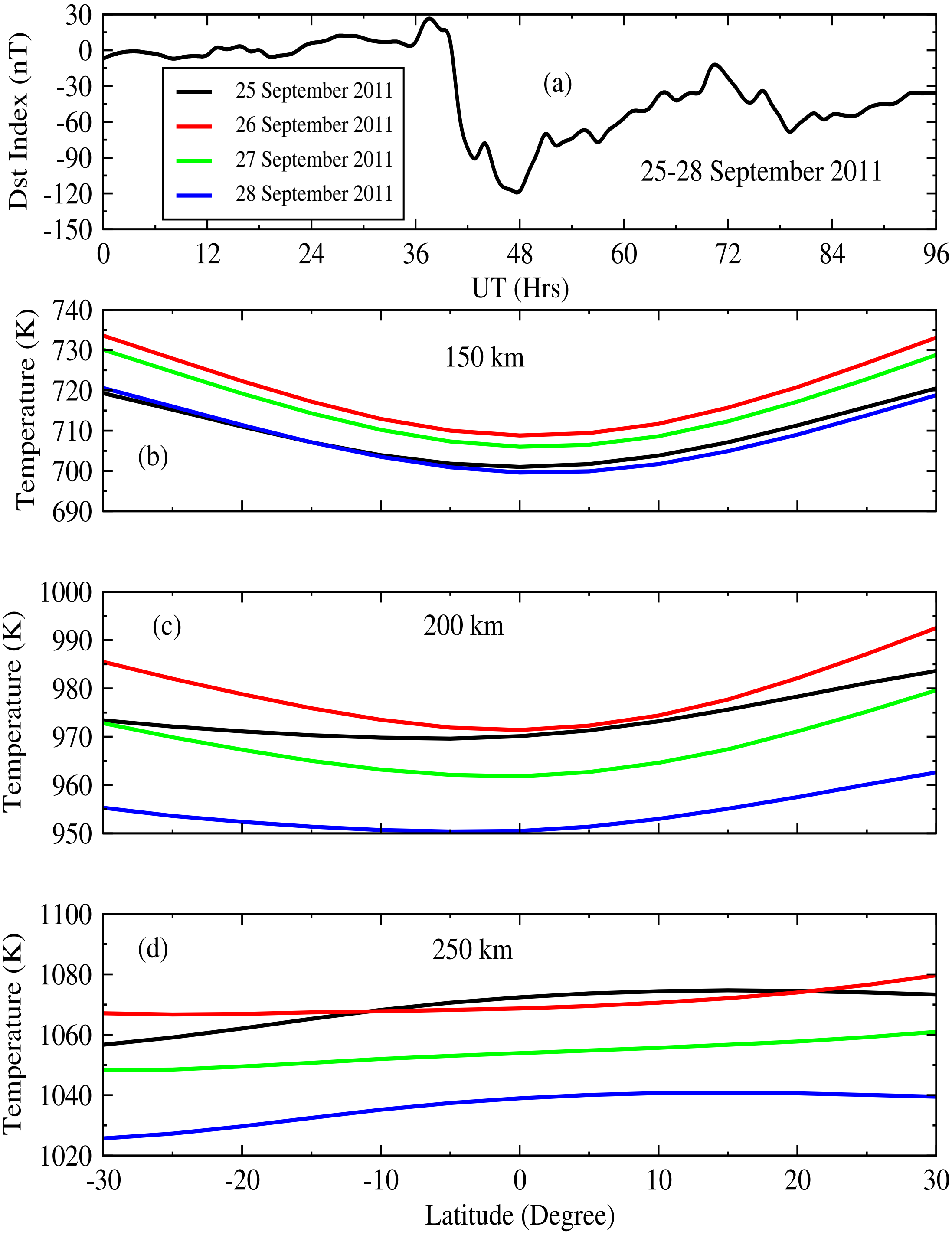

Figure 5.11: Variation of Dst Index (panel a), Neutral temperature at 150 km (panel b), 200 km (panel c), and 250 km (panel d) with latitude during storm1.

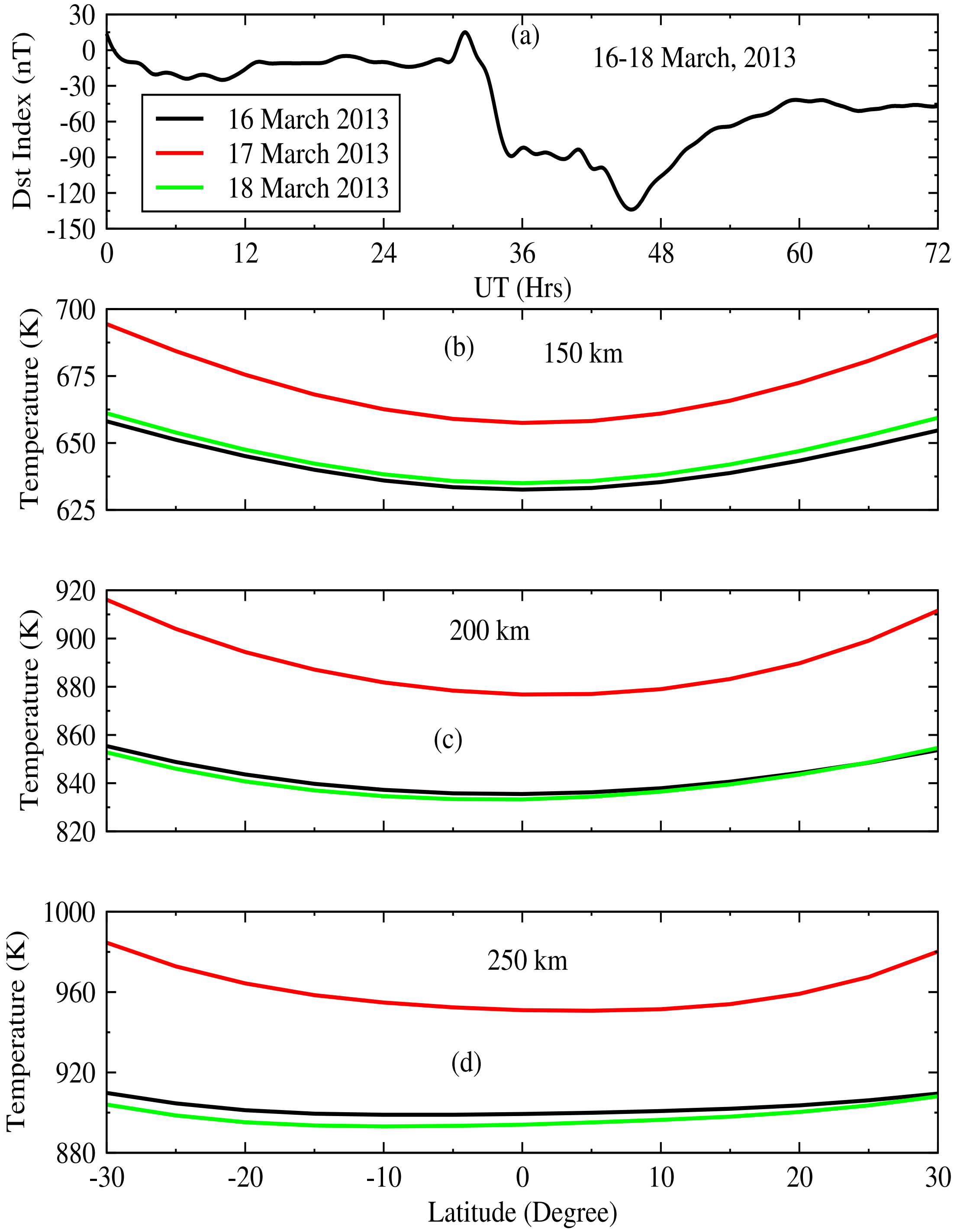

Figure 5.12: Variation of Dst Index (panel a), Neutral temperature at 150 km (panel b), 200 km (panel c), and 250 km (panel d) with latitude during storm2

First, there is an enhancement in neutral temperature at all heights during the main phase of the storm and Second, is the neutral temperature exhibits a bow shaped variation across latitudes with the maximum towards the mid-latitudes (±30° latitude). Similar temperature anomaly has also been reported earlier [243, 244]. This kind of anomaly in temperature has been attributed to adiabatic cooling [249]. During the storm period, the enhancement in the plasma density results in the enhancement in the field-aligned ion drag which subsequently increases the poleward meridional wind creating a temperature trough over the equator (Figure 5.11b & c). It is very important to note that the temperature anomaly is inconspicuous at the 250 km altitude although the response to the storm is common across all altitudes.

Figure 5.12 shows the Dst index (a), neutral temperature at different heights (b-d) during storm2. Although most of the features are common to what has been observed during storm1, one interesting feature is that with the progression of the storm, the temperature reaches a new low value as the storm recovers. The correlation of neutral temperature with the progression of the storm is clearly different at 250 km during both the storms. At the 250 km, the temperature shows almost no latitudinal variation during the main phase of the storm. However, a little latitudinal variation is found during the pre-onset and recovery phases.

The day-to-day variations in the latitudinal volume emission rate of 557.7 nm emission are anti-correlated to the variation in ETA during both the storms at 150 km, whereas we see that these variations are directly correlated to the variations in ETA at the lower thermospheric altitudes. The latitudinal variation in the VER of 732.0 nm emission are correlated directly to the variations induced in ETA during both the storm periods. The observed changes in the strength of ETA and the nature of fluctuations in ETA during the storm time closely match with the earlier reports.

To understand the day-to-day variation of EIA during the storm period, we have calculated the latitudinal profile of EIA using IRI-2012 model. Figure 5.13 shows the variation in the latitudinal profile of electron density at 250 km altitude obtained from IRI-2012 model. From the figure it can be seen that during the geomagnetic storm,

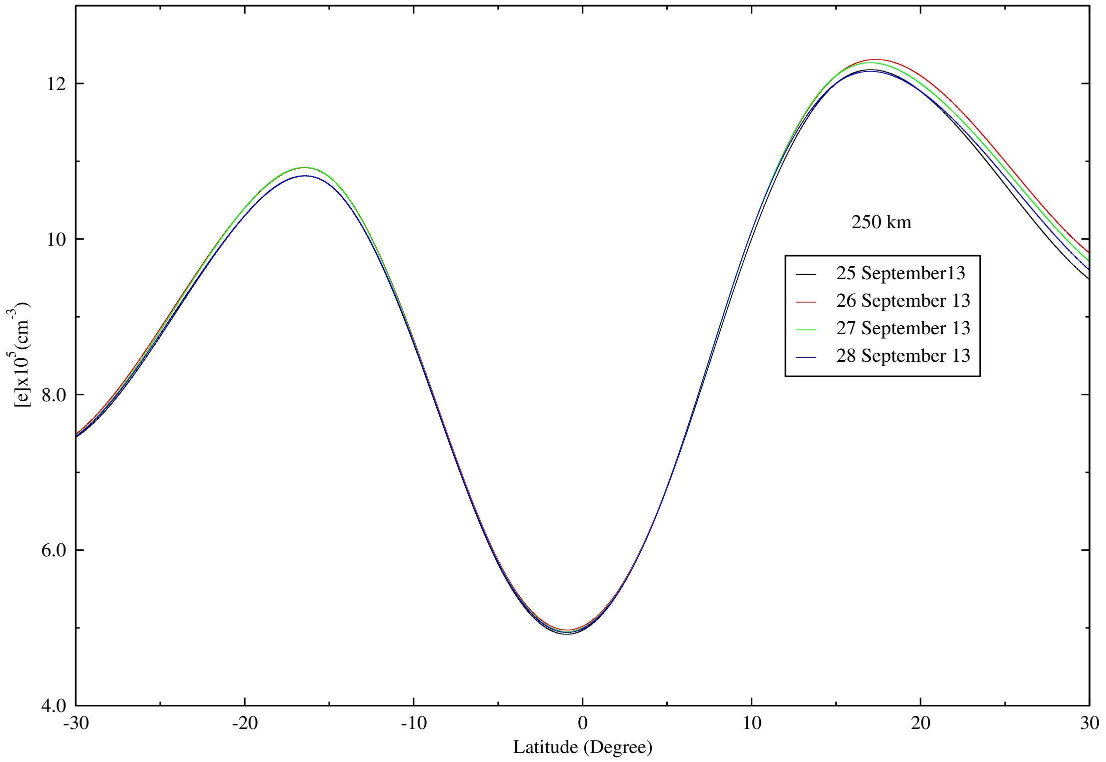

Figure 5.13: Latitudinal variation of electron density at 250 km during storm1.

electron density increases by nearly 5-8 percent and this increase is more pronounced at the anomaly crest. The increase in the electron flux results due to the excess energy that enters into the ionosphere during a geomagnetic storm.

5.4 Conclusions

The influence of the geomagnetic storms on the equatorial ionization anomaly (EIA) and equatorial temperature anomaly(ETA) has been studied using the photochemical models for atomic oxygen dayglow emissions for four intense geomagnetic storms during solar cycle 24. The modeled VER for atomic oxygen greenline shows different type of variations at different altitudes. The VER of greenline emission shows a positive correlation with the Dst index at 150 km and a negative correlation at the altitudes of 200 and 250 km. This altitudinal dependence of correlation is mainly due to day-to-day variations in dissociative recombination and photo-electron impact excitation processes during a geomagnetic storm. The percentage change in the greenline VER is found to be higher at 250 km in comparison to what is seen at 150 and 200 km. The EIA has a strong signature in the emission profiles over the latitudes and the hemispheric asymmetry in VER at the EIA crests is less pronounced at higher altitudes. The VER for 732.0 nm shows an enhancement during the storm period. The latitudinal variation of 732.0 nm volume emission rate is opposite to the trend of EIA. This is because of the strengthening of quenching due to the large availability of electron density at the EIA crests. The neutral temperature calculated from NRLMSISE-00 model shows a negative correlation with the Dst index. The model calculated neutral temperature also exhibits an equatorial anomaly with the trough centered at around the equator.The day-to-day latitudinal profile of 557.7 nm and 732.0 nm emission shows a similar correlation to ETA as seen with respect to Dst index.

BIBLIOGRAPHY

[1] Y. M. Cho, G. G. Shepherd, Y. I. Won, S. Sargoytchev, S. Brown, and B. Solheim, MLT cooling during stratospheric warming events. Geophysical Research Letters, **31**, 2004.

[2] Yvan Joseph Orsolini, I. T. Kindem, and N. G. Kvamsto, On the potential impact of the stratosphere upon seasonal dynamical hindcasts of the north atlantic oscillation: a pilot study. Climate Dynamics, **36**, 579–588, 2009.

[3] C. E. Randall, V. L. Harvey, G. L. Manney, Y. Orsolini, M. Codrescu, C. Sioris, S. Brohede, C. S. Haley, L. L. Gordley, J. M. Zawodny, and J. M. Russell, Stratospheric effects of energetic particle precipitation in 2003–2004. Geophysical Research Letters, **32**, 2005.

[4] A. Upadhayaya, G. Gupta, A statistical analysis of occurrence characteristics of spread-F irregularities over indian region. Journal of Atmospheric and Solar-Terrestrial Physics, **112**, 1–9, 2014.

[5] A. K. Upadhayaya, Sumedha Gupta, and P. S. Brahmanandam, F_2 region response to geomagnetic disturbances across Indian latitudes: $O(^1S)$ dayglow emission. Journal of Geophysical Research: Space Physics, **121**, 2595–2620, 2015.

[6] K. S. Paul, A. Das, S. Ray, and A. Paul, Characteristics of total electron content (TEC) observed from a chain of stations near the northern crest of the equatorial ionization anomaly (EIA) along 88.5° E meridian in india. Journal of Atmospheric and Solar-Terrestrial Physics, **137**, 17–28, 2016.

[7] A. Paul, T. Das, S. Ray, A. Das, D. Bhowmick, and A. Das Gupta, Response of the equatorial ionosphere to the total solar eclipse of 22 July 2009 and annular eclipse of 15 January 2010 as observed from a network of stations situated in the Indian longitude sector. Annales Geophysicae, **29**, 1955–1965, 2011.

[8] A. K. Upadhayaya, and K. K. Mahajan, Ionospheric F_2 region: Variability and sudden stratospheric warmings. Journal of Geophysical Research: Space Physics, **118**, 6736–6750, 2013.

[9] K. Ramesh, S. Sridharan, Large mesospheric inversion layer due to breaking of small-scale gravity waves: Evidence from rayleigh lidar observations over Gadanki (13.5° N,79.2° E). Journal of Atmospheric and Solar-Terrestrial Physics, **89**, 90 – 97, 2012.

[10] S. Sridharan, S. Sathishkumar, Seasonal and interannual variations of gravity wave activity in the low-latitude mesosphere and lower thermosphere over tirunelveli (8.7° N, 77.8° E). Annales Geophysicae, **26**, 3215–3223, 2008.

[11] Wagholikar, K. Nilesh, Sinha Ray, K. C., Sen, P. N., and Kumar, P. Pradeep, Trends in seasonal temperatures over the Indian region. Journal of Earth System Science, **123**, 673–687, 2014.

[12] P. Pradeep Kumar, G. K. Manohar, and S. S. Kandalgaonkar, Global distribution of nitric oxide produced by lightning and its seasonal variation. Journal of Geophysical Research: Atmospheres, **100**, 11203–11208, 1995.

[13] H. Chandra, H. S. S. Sinha, A. K. Patra, U. Das, D. Selvaraj, R. N. Misra, and J. Datta, Low-latitude mesospheric turbulence investigated using coordinated MST radar and rocket-borne observations from India. Journal of Geophysical Research: Atmospheres, **117**, 2011.

[14] M. A. Abdu H. Chandra, Som Sharma and I. S. Batista., Spread-F at anomaly crest regions in the Indian and American longitudes. Advances in Space Research, **31**, 717–727, 2003.

[15] B. T. Tsurutani, O. P. Verkhoglyadova, A. J. Mannucci, G. S. Lakhina, G. Li, and G. P. Zank, A brief review of “solar flare effects” on the ionosphere. Radio Science, **44**, 2009.

[16] S. Sathishkumar and S. Sridharan, Planetary and gravity waves in the mesosphere and lower thermosphere region over Tirunelveli (8.7° N, 77.8° E) during stratospheric warming events. Geophysical Research Letters, **36**, 2008.

[17] Marty Mlynczak, F. Javier Martin-Torres, James Russell, Ken Beaumont, Steven Jacobson, Janet Kozyra, Manuel Lopez-Puertas, Bernd Funke, Christopher Mertens, Larry Gordley, Richard Picard, Jeremy Winick, Peter Wintersteiner, and Larry Paxton, The natural thermostat of nitric oxide emission at 5.3 μm in the thermosphere observed during the solar storms of April 2002. Geophysical Research Letters, **30**, n/a–n/a, 2003.

[18] Martin G. Mlynczak, F. Javier Martin-Torres, B. Thomas Marshall, R. Earl Thompson, Joshua Williams, Timothy Turpin, David P. Kratz, James M. Russell, Tom Woods, and Larry L. Gordley, Evidence for a solar cycle influence on the infrared energy budget and radiative cooling of the thermosphere. Journal of Geophysical Research: Space Physics, **112**, 2007.

[19] C. A. Barth, K. D. Mankoff, S. M. Bailey, and S. C. Solomon, Global observations of nitric oxide in the thermosphere. Journal of Geophysical Research: Space Physics, **108**, n/a–n/a, 2003.

[20] Koen Hendrickx, Linda Megner, Daniel R. Marsh, Jörg Gumbel, Rickard Strandberg, and Felix Martinsson, Relative importance of nitric oxide physical drivers in the lower thermosphere. Geophysical Research Letters, **44**, 10,081–10,087, 2017.

[21] D. Knipp, L. Kilcommons, L. Hunt, M. Mlynczak, V. Pilipenko, B. Bowman, Y. Deng, and K. Drake, Thermospheric damping response to sheath-enhanced geospace storms. Geophysical Research Letters, **40**, 1263–1267, 2013.

[22] Martin G. Mlynczak, Linda A. Hunt, B. Thomas Marshall, James M. Russell, Christopher J. Mertens, R. Earl Thompson, and Larry L. Gordley, A combined solar and geomagnetic index for thermospheric climate. Geophysical Research Letters, **42**, 3677–3682, 2015.

[23] Y. Zhang, L. J. Paxton, D. Morrison, D. Marsh, and H. Kil, Storm-time behaviors of O/N_2 and NO variations. Journal of Atmospheric and Solar-Terrestrial Physics, **114**, 42–49, 2014.

[24] Gaurav Bharti, M. V. Sunil Krishna, T. Bag, and Puneet Jain, Storm time variation of radiative cooling by nitric oxide as observed by TIMED-SABER and GUVI. Journal of Geophysical Research: Space Physics, **123**, 1500–1514, 2018.

[25] T. Bag, M. V. Sunil Krishna, and V. Singh, Modeling of Na airglow emission and first results on the nocturnal variation at midlatitude. J. Geophys. Res. Space Phys., **120**, 10,945–10,958, 2015.

[26] J. M. C. Plane, W. Feng, and E. C. M. Dawkins, The mesosphere and metals: Chemistry and changes. Chem. Rev., **115**, 4497–4541, 2015.

[27] J. M. C. Plane, Atmospheric chemistry of meteoric metals. Chem. Rev., **103**, 4963–4984, 2003.

[28] M. M. Hossain, C. N. Vineeth, S. K. Sumod, and T. K. Pant, Highly varying daytime sodium airglow emissions over an equatorial station: a case study based on the measurements using a grating monochromator. Earth Planets Space, **66:56**, 2014.

[29] S. Sarkhel, R. Sekar, D. Chakrabarty, R. Narayanan and S. Sridharan, Simultaneous sodium airglow and lidar measurements over India: A case study. J. Geophys. Res., **114**, 189, 2009.

[30] S. Sarkhel, R. Sekar, D. Chakrabarty and S. Sridharan, A case study on the possible altitude-dependent effects of collisions on sodium airglow emission. J. Geophys. Res., **115**, 189, 2010.

[31] J. Plane, H. Oetjen, M. Miranda, A. Saiz-Lopez, M. Gausa, and B. Williams, On the sodium D line emission in the terrestrial nightglow. J. Atmos. Sol-Terr. Phys., **74**, 181–188, 2012.

[32] B. R. Clemesha, P. P. Batista, D. M. Simonich, Tide induced oscillation in atmosphere sodium layer. J. Atmos.Solar-Terr.Phys., **64**, 1321–1325, 2002.

[33] B. R. Clemesha, D. M. Simonich, P. P. Batista, H. Takahashi, Seasonal variation in solar diurnal tide and its possible influence on atmospheric sodium layer. Adv. Space Res., **35**, 1951–1956, 2005.

[34] S. Sridharan, P. Vishnu Prasanth, Y. Bhavani Kumar, Geetha Ramkumar, S. Sathishkumar, and K. Raghunath, Observations of peculiar sporadic sodium structures and their relation with wind variations. Journal of Atmospheric and Solar-Terrestrial Physics, **71**, 575–582, 2009.

[35] G. G. Shepherd, C. McLandress and B. H. Solheim., Tidal influence on O(^{1}S) airglow emission rate distributions at the geographic equator as observed by WINDII. Geophys. Res. Lett., **22**, 275–278, 1995.

[36] S. Peteherych, G. G. Shepherd and J. K. Walker., Observation of vertical E-region neutral winds in two intense auroral arcs. Planetary and Space Science., **33**, 869–873, 1985.

[37] S. P. Zhang and G. G. Shepher, The influenceof the diurnal tide on the O(^{1}S) and OH emission rates observed by WINDII on UARS. Geophys. Res. Lett., **26**, 529–532, 1999.

[38] B. T. Tsurutani, G. S. Lakhina, O. P. Verkhoglyadova, W. D. Gonzalez, E. Echer, and F. L. Guarnieri, A review of interplanetary discontinuities and their geomagnetic effects. Journal of Atmospheric and Solar-Terrestrial Physics, **73**, 5–19, 2011.

[39] S. Alex, S. Mukherjee, and G. S. Lakhina, Geomagnetic signatures during the intense geomagnetic storms of 29 October and 20 November 2003. Journal of Atmospheric and Solar-Terrestrial Physics, **68**, 769 – 780, 2006.

[40] Jan Lastovicka, Stanley C. Solomon, and Liying Qian, Trends in the neutral and ionized upper atmosphere. Space Science Reviews, **168**, 113–145, Jun 2012.

[41] Jan Lastovicka, Forcing of the ionosphere by waves from below. Journal of Atmospheric and Solar-Terrestrial Physics, **68**, 479–497, 2006.

[42] Liying Qian, Jan Lastovicka, Raymond G. Roble, and Stanley C. Solomon, Progress in observations and simulations of global change in the upper atmosphere. Journal of Geophysical Research: Space Physics, **116**, 2011.

[43] T. Takahashi, K. Hosokawa, S. Nozawa, T. T. Tsuda, Y. Ogawa, M. Tsutsumi, Y. Hiraki, H. Fujiwara, T. D. Kawahara, N. Saito, S. Wada, T. Kawabata, and C. Hall, Depletion of mesospheric sodium during extended period of pulsating aurora. Journal of Geophysical Research: Space Physics, **122**, 1212–1220, 2017.

[44] T. T. Tsuda, T. Nakamura, M. K. Ejiri, T. Nishiyama, K. Hosokawa, T. Takahashi, J. Gumbel, and J. Hedin, Statistical investigation of Na layer response to geomagnetic activity using resonance scattering measurements by Odin/OSIRIS. Geophysical Research Letters, **44**, 5943–5950, 2017.

[45] U. von Zahn, P. von der Gathen, and G. Hansen, Forced release of sodium from upper atmospheric dust particles. Geophysical Research Letters, **14**, 76–79, 1987.

[46] Y. Y. Gu, J. Qian, G. C. Papen, G. R. Swenson, and P. J. Espy, Concurrent observations of auroral activity and a large sporadic sodium layer event during ANLC-93,. Geophysical Research Letters, **22**, 2805–2808, 1995.

[47] P. Thirupathaiah, Seasonal variation of some important atomic oxygen dayglow emissions. Ph.D. Thesis, Indian Institute of Technology, Roorkee, 2014.

[48] Solar-Terrestrial Research for the 1980s, Washington, DC, National Research Council, National Academy Press(1981).

[49] J. K. Hargreaves, The solar-terrestrial environment. Cambridge University Press(1992).

[50] C. Y. Johnson, Ionospheric composition and density from 90 to 1200 kilometers at solar minimum. J. Geophys. Res., **71**, 330–332, 1966.

[51] H. E. Hinteregger, K. Fukui and B. R. Gilson, Observational reference and model data on solar EUV from measurements on AE-E. Geophys. Res. Lett., **8**, 1147–1150, 1981.

[52] E. V. P. Smith and D. M. Gottlieb, Solar flux and its variations. Space Sci. Rev., **16(5–6)**, 771–802, 1974.

[53] J. R. Holton, The influence of gravity wave breaking on the general circulation of the middle atmosphere. J. Atmos. Sci., **40**, 2497–2507, 1983.

[54] C. O. Hines, Internal atmospheric gravity waves at ionospheric heights. Can. J. Phys., **38**, 1441–1481, 1960.

[55] H. G. Mayr and K. K. Mahajan, Seasonal variation in the F_2 region. Journal of Geophysical Research, **76**, 1017–1027.

[56] K. K. Mahajan and V. K. Pandey, Models of electron temperature in the topside ionosphere for low and medium solar activity conditions. Journal of Geophysical Research: Space Physics, **85**, 213–216, 1980.

[57] R. Wahi, S. Dubey and A. K. Gwal., Ionospheric total electron content measurement in malaysian region during high solar activity using GPS receiver. Indian Journal of Radio and Space Physics, **34**, 399–401, 2005.

[58] S. Bhattacharya, P. K Purohit, A. K. Gwal, Ionospheric time delay variations in the equatorial anomaly region during low solar activity using GPS. Indian Journal of Radio and Space Physics, **38**, 262–274, 2009.

[59] H. Chandra and G. D. Vyas., Abnormally low F-layer ionization over Ahmedabad during the night of 26-27 November 1984. Indian Journal of Radio and Space Physics, **39**, 346–352, 2010.

[60] H. Chandra, S. Sharma and S. W. Aung, F-region variability over the anomaly crest region. Indian Journal of Radio and Space Physics, **39**, 302–307, 2010.

[61] S. Sharma, H. Chandra, H. O. Vats, N. Y. Pandya, and R. Jain, Ionospheric modulations due to solar flares over Ahmedabad. Indian Journal of Radio and Space Physics, **39**, 296–301, 2010.

[62] A. Jain, S. Tiwari, S. Jain and A.K. Gwal, TEC response during severe geomagnetic storms near the crest of equatorial ionization anomaly. Indian Journal of Radio and Space Physics, **39**, 11–241, 2010.

[63] G. P. Brasseur and S. Solomon., Aeronomy of the middle atmosphere. 3rd edition, Springer(2005).

[64] P. Banks and G. Kockarts, Aeronomay: Part b. Academic Press, New York(1973).

[65] M. C. Kelly, The Earth's Ionosphere: Plasma Physics and Electrodynamics. 2nd edition, Elsevier(2009).

[66] J. Lean, Solar ultraviolet irradiance variations:a review. J. Geophys. Res., **92**, 839–868, 1987.

[67] K. K. Mahajan, Pioneer venus orbiter measurements of solar EUV flux during solar cycles 21 and 22. Sol. Phys., **177**, 203–216, 1998.

[68] A. E. Covington, Solar noise observations on 10.7 centimeters. Proc. I.R.E., **36**, 454–457, 1948.

[69] L. Oster, Solar irradiance variations 2. analysis of the extreme ultraviolet measurements onboard the Atmospheric Explorer E satellite. J. Geophys. Res., **88**, 1983.

[70] A. E. Hedin, Correlations between thermospheric density and temperature, solar EUV flux, and 10.7-cm flux variations. J. Geophys. Res., **89(A11)**, 9828–9834, 1984.

[71] W. Livingston, M. J. Penn, and L. Svalgaard, Decreasing sunspot magnetic fields explain unique 10.7 cm radio flux. Astrophys. J. Lett., **757**, L8, 2012.

[72] T. N. Chatterjee and T. K. Das, Relation between UV flux and solar 10.7 cm emission. Mon. Not.R. Astron. Soc, **274**, 858–860, 1995.

[73] W. A. Baum, F. S. Johnson, J. J. Oberly, C. C. Rockwood, C. V. Strain and R. Tousey, Solar ultraviolet spectrum to 88 kilometers. Rev., **70**, 781, 1946.

[74] H. E. Hinteregger, Preliminary data on solar extreme ultraviolet radiation in the upper atmosphere. J. Geophys. Res., **55**, 2367–2380, 1961.

[75] H. E. Hinteregger, in space astrophysics (ed. by W. Liller). McGraw Hill Publ.(1961a), page 33.

[76] H. E. Hinteregger, Absorption spectrometric analysis of the upper atmosphere in EUV region. J. Atmos. Sci., **19**, 351–368, 1962.

[77] H. E. Hinteregger, L. A. Hall and W. Schweizer, Solar XUV spectrum from 310A° to 50A°. Astrophys. J., **140**, 319–327, 1964.

[78] R. D. Bourdeau, S. Chandra, and W. M. Neupert, Time correlation of extreme ultraviolet radiation and thermospheric temperature. J. Geophys. Res., **69**, 4531–4535, 1964.

[79] G. G. Fazio and E. M. Hafner, The OSO-1 high-energy gamma-ray experiment. J. Geophys. Res., **72**, 9, 1967.

[80] W. M. Neupert, Intensity variations in the solar extreme ultraviolet spectrum observed by OSO-1. Ann. d́Astr., **28**, 446, 1965.

[81] H. E. Hinteregger, D. E. Bedo and J. E. Manson, The EUV spectrophotometer on atmosphere Explorer. Radio. Sci., **8**, 349–359, 1973.

[82] J. E. Manson H. E. Hinteregger, D. E. Bedo and D. R. Skillman, EUV flux variations with solar rotation observed during 1974-1976 from AE satellites C, D, and E. COSPAR, Plenary Meeting, 19th, Philadelphia, Pa., **819**, 31, 1976.

[83] D. F. Heath, Space observations of the variability of solar irradiance in the near and far ultraviolet. J. Geophys. Res., **78**, 2779–2792, 1973.

[84] T. N. Woods and G. J. Rottman, Solar EUV irradiance derived from a sounding rocket experiment on November 10, 1988. J. Geophys. Res., **95**, 6227–6236, 1990.

[85] V. Doming, B. Fleck, and A. I. Poland, The SOHO mission: An overview. Sol. Phys., **162**, 1–37, 1995.

[86] T. N. Woods, G. J. Rottman, R. G. Roble, O. R. White, S. C. Solomon, G. M. Lawrence, J. Lean, and W. K. Tobiska, Thermosphere-Ionsphere-Mesosphere Energetics and Dynamics (TIMED) solar EUV experiment. Proc. SPIE 2266, pages 467–479, 1994.

[87] T. N. Woods, F. G. Eparvier, S. M. Bailey, P. C. Chamberlain, J. Lean, G. J. Rottman, S. C. Solomon, W. K. Tobiska and D. Woodraska, The Solar EUV Experiment (SEE): Mission overview and first results. J. Geophys. Res., **110**, 189, 2005.

[88] L. Heroux and J. E. Higgins, Summary of full-disk solar fluxes between 250 and 1940A°. J. Geophys. Res., **82**, 3307–3310, 1977.

[89] W. K. Tobiska and C. A. Barth, A solar EUV flux model. J. Geophys. Res., **90**, 8243–8251, 1990.

[90] P. G. Richards, D. G. Torr and J. A. Fennelly, EUVAC: A solar EUV flux model for aeronomic calculations. J. Geophys. Res., **99**, 8981–8992, 1994.

[91] W. K. Tobiska, T. Woods, F. Eparvier, R. Viereck, L. Floyd, D. Bouwer, G. Rottman, O. R. White, The SOLAR2000 empirical solar irradiance model and forecast tool. J. Atmos. Sol. Terr. Phys., **62**, 1233–1250, 2000.

[92] M. V. Sunil Krishna and V. Singh, Effect of solar activity on the morphology of 7320A° dayglow emission. Ann. Geophys., **27**, 4089–4096, 2009.

[93] M. V. Sunil Krishna and V. Singh, Morphology of OI 8446$\mathring{a}$ dayglow emission. Adv. Space. Res., **46**, 81–88, 2010.

[94] M. V. Sunil Krishna and V. Singh, Solar influence on the redline dayglow emission under equinox conditions. J. Atmo. Sol. Terr. Phys., **73**, 499–506, 2011.

[95] S. G. Kanekal D. N. Baker, J.H. Allen and G.D. Reeves, Disturbed space environment may have been related to pager satellite failure. EOS, **79**, 477, 1998.

[96] L. J. Lanzerotti, Space weather. Geophys. Monograph 125, Amer. Geophys. Union(2001), page 11.

[97] J. G. Kappenman, Space storms and space weather hazards. Kluwer Acad. Pub.(2001), page 335, 2001.

[98] I. A. Daglis, The storm-time ring current. Space Sci. Rev., **98**, 343–363, 2001.

[99] W. D. Gonzalez, J. A. Joselyn, Y. Kamide, H. W. Kroehl, G. Rostoker, B. T. Tsurutani and V. M. Vasyliunas, What is a geomagnetic storm? J. Geophys. Res., **99**, 5771–5792, 1994.

[100] J. W. Chamberlain, Physics of the aurora and airglow. Academic Press, New York(1961).

[101] M.H. Rees, Physics and chemistry of the upper atmosphere. Cambridge University Press(1989).

[102] L. Yntema, On the brightness of the sky and total amount starlight. Publ. Ast. Groningen, **22**, 1–55, 1909.

[103] H. Takahashi, M. J. Taylor, J. H. A. Sobral, A. F. Medeiros, and D. Gobbi, Fine structure of the ionospheric plasma bubbles observed by the OI 6300 and 5577 A° airglow imagers. Adv. Space. Res., **27**, 1189–1194, 2001.

[104] O. Witasse, J. Lilensten, C. Lathuilliere and P.L. Blelly, Modeling the OI 630.0 and 557.7 nm thermospheric dayglow during EISCAT-WINDII coordinated measurements. J. Geophys. Res., **104**, 24639–24655, 1999.

[105] D. W. Rusch, J C. Gerard, and W. E. Sharp, The reaction of $N(^2D)$ with O_2 as a source of $O(^1D)$ atoms in aurorae. Geophysical Research Letters, **5**, 1043–1046, 1978.

[106] J. C. Gerard and D. W. Rusch, The auroral ionosphere: Comparison of a time-dependent model with composition measurements. Journal of Geophysical Research: Space Physics, **84**, 4335–4340, 1979.

[107] S. P Zhang, R. N Peterson, R. H Wiens and G.G Shepherd, Gravity waves from O_2 nightglow during the AIDA '89 campaign I: emission rate/temperature observations. J. Atmos. terr. Phys., **55**, 355–375, 1993.

[108] V. Singh, I. C. McDade, G. G. Shepherd, B. H. Solheim and W.E. Ward, The $O(^1D)$ dayglow emission as observed by the WIND imaging interferometer on uars. Adv. Space. Res., **17**, 11–14, 1996.

[109] V. Singh, I. C. McDade, G. G. Shepherd, B. H. Solheim, and W. E. Ward, The $O(^1s)$ dayglow emission as observed by WIND Imaging Interferometer on UARS. Ann. Geophys., **14**, 637–646, 1996.

[110] M.V. Sunil Krishna P. Thirupathaiah and V. Singh, Effect of solar activity on the latitudinal variation of peak emission rate of 557.7 nm dayglow emission under equinox conditions. J. Atmo. Sol. Terr. Phys., **77**, 209–218, 2012.

[111] P. Thirupathaiah, V. Singh and M. V. Sunil Krishna, An analytical approach to estimate atomic oxygen density from greenline dayglow emission in thermosphere at 250 km. Ind. J. Radio. Space., **42**, 219–228, 2013.

[112] S. P. Zhang and G. G. Shepherd, Solar influence on the O(^{1}D) dayglow emission rate: Global-scale measurements by WINDII on UARS. Geophys. Res. Lett., **31**, L07804, 2004.

[113] G. Liu, G. G. Shepherd and R. G. Roble., Seasonal variations of the nighttime O(^{1}S) and OH airglow emission rates at mid-to-high latitudes in the context of the large-scale circulation. J. Geophys. Res., **113**, ann, 2008.

[114] G. G. Shepherd, R. G. Roble and Y. Cho, WINDII observations and TIME-GCM simulations of O(^{1}S) polar spirals during geomagnetic disturbances. J. Geophys. Res., **118**, 2721–2733, 2013.

[115] S. Sathishkumar, S. Sridharan, and Ch. Jacobi, Dynamical response of low-latitude middle atmosphere to major sudden stratospheric warming events. Journal of Atmospheric and Solar-Terrestrial Physics, **71**, 857–865, 2009.

[116] D. R. Marsh, M. J. Mills, D. E. Kinnison, J.-F. Lamarque, N. Calvo and L. M. Polvani, Climate change from 1850 to 2005 simulated in CESM1(WACCM). J. climate, **26**, 7372–7391, 2013.

[117] K. L. Smith, R. R. Neely, D. R. Marsh, and L. M. Polvani, The Specified Chemistry Whole Atmosphere Community Climate Model (SC-WACCM). Journal of Advances in Modeling Earth Systems, **6**, 883–901, 2014.

[118] C. O. Hines and D. W. Tarasick, On the detection and utilization of gravity waves in airglow studies. Planet. Space Sci., **35**, 851–866, 1987.

[119] D. W. Tarasick and C. O. Hines, The observable effects of gravity waves on airglow emissions. Planet. Space Sci., **38**, 1105–1119, 1990.

[120] M. J. Taylor, M. A. Hapgood, P. Rothwell, Observations of gravity wave propagation in the OI (557.7 nm), Na (589.2 nm) and the near infrared OH nightglow emissions. Planet. Space Sci., **35**, 413–427, 1987.

[121] S. Sarkhel, R. Sekar, D. Chakrabarty, and A. Guharay, Investigation on mesospheric gravity waves over Indian low latitudes stations using sodium airglow observations and few case studies based on thermal wind structure. J. Atmos. Sol. Terr. Phys., **86**, 41–50, 2012.

[122] Sumanta Sarkhel, John D. Mathews, Shikha Raizada, Ramanathan Sekar, Dibyendu Chakrabarty, Amitava Guharay, Geonhwa Jee, Jeong-Han Kim, Robert B. Kerr, Geetha Ramkumar, Sundararajan Sridharan, Qian Wu, Martin G. Mlynczak, and James M. Russell, A case study on occurrence of an unusual structure in the sodium layer over Gadanki, India. Earth, Planets and Space, **67**, 19, 2015.

[123] B. Clemesha, D. Simonich, and P. Batista, Mesopause region temperature structure observed by sodium resonance lidar. J.Atmos.Solar-Terr. Phys., **72**, 740–744, 2010.

[124] C. Y. She, B. P. Williams, P. Hoffmann, R. Latteck, G. Baumgarten, J. D. Vance, .Fiedler, P. Acott, D. C. Fritts, F.-J. Lubken, Simultaneous observation of sodium atoms, NCL,PMSE in summer mesopause above ALOMAR Norway (69°N,12°E). J. Atmos. Sol-Terr. Phys., **68**, 93–101, 2006.

[125] I. C. McDade, D. P. Murtagh, R .G. H. Greer, P. H. G. Dickinson, G. Witt, J. Stegman, E. J. Llewellyn, L. Thomas, and D. B. Jenkins., ETON 2: Quenching parameters for the proposed precursors of $O_2(b^1\sigma_g)$ and $O(^1S)$ in the terrestrial nightglow. Planet. Space. Sci., **34**, 789–799, 1986.

[126] H. Garrigue, Noveaux resultats sur la lumiere duciel nocturne. compt. rend. 202, **64**, 1807, 1936.

[127] S. Akasofu and S. Chapman, Solar-Terrestrial Physics.

[128] M. P. Langowski, C. von Savigny, J. P. Burrows, W. Feng, J. M. C. Plane, D. R. Marsh, D. Janches, M. Sinnhuber, A. C. Aikin, and P. Liebing, Global investigation of the Mg atom and ion layers using SCIAMACHY/Envisat observations between 70 and 150 km altitude and WACCM-Mg model results. Atmospheric Chemistry and Physics, **15**, 273–295, 2015.

[129] D Murtagh, U Frisk, F Merino, M Ridal, A Jonsson, J Stegman, G Witt, P Eriksson, C Jiménez, G Megie, J de la Noë, P Ricaud, P Baron, J R Pardo, A Hauchcorne, E J Llewellyn, D A Degenstein, R L Gattinger, N D Lloyd, W FJ Evans, I C McDade, C S Haley, C Sioris, C von Savigny, B H Solheim, J C McConnell, K Strong, E H Richardson, G W Leppelmeier, E Kyrölä, H Auvinen, and L Oikarinen, An overview of the Odin atmospheric mission. Canadian Journal of Physics, **80**, 309–319, 2002.

[130] A.C. Aikin, J.M. Grebowsky, and J. P. Burrows, Satellite measurements of the atmospheric content of metallic ion and neutral species. Advances in Space Research, **33**, 1481–1485, 2004.

[131] K. Bossert, D. C. Fritts, P. D. Pautet, M. J. Taylor, B. P. Williams, and W. R. Pendelton, Investigation of a mesospheric gravity wave ducting event using

coordinated sodium lidar and mesospheric temperature mapper measurements at ALOMAR, Norway (69° N). J. Geophys. Res. Atmos., **119**, 9765–9778, 2014.

[132] X. Cai, T. Yuan, Y. Zhao, P. D. Pautet, M. J. Taylor, and W. R. Pendleton Jr., A coordinated investigation of the gravity wave breaking and the associated dynamical instability by a Na lidar and an advanced mesosphere temperature mapper over Logan, UT (41.7° N, 111.8° W). J. Geophys. Res. Space Phys., **119**, 6852–6864, 2014.

[133] Charles A. Barth, Nitric oxide in the lower thermosphere. Planetary and Space Science, **40**, 315–336, 1992.

[134] G. Lu, M. G. Mlynczak, L. A. Hunt, T. N. Woods, and R. G. Roble, On the relationship of Joule heating and nitric oxide radiative cooling in the thermosphere. Journal of Geophysical Research: Space Physics, **115**, n/a–n/a, 2010.

[135] T. E. Cravens, The global distribution of nitric oxide at 200 km. Journal of Geophysical Research: Space Physics, **86**, 5710–5714, 1981.

[136] C. G. Fesen, D. W. Rusch, and J.-C. Gérard, The latitudinal gradient of the NO peak density. Journal of Geophysical Research: Space Physics, **95**, 19053–19059, 1990.

[137] D. E. Siskind, C. A. Barth, and R. G. Roble, The response of thermospheric nitric oxide to an auroral storm: 1. low and middle latitudes. Journal of Geophysical Research: Space Physics, **94**, 16885–16898, 1989.

[138] C. A. Barth, Reference models for thermospheric nitric oxide, 1994. Advances in Space Research, **18**, 179–208, 1996.

[139] C. A. Barth and S. M. Bailey, Comparison of a thermospheric photochemical model with Student Nitric Oxide Explorer (SNOE) observations of nitric oxide. Journal of Geophysical Research: Space Physics, **109**, n/a–n/a, 2004.

[140] D. E. Siskind, C. A. Barth, and D. D. Cleary, The possible effect of solar soft X rays on thermospheric nitric oxide. Journal of Geophysical Research: Space Physics, **95**, 4311–4317, 1990.

[141] Barth, Charles A., Bailey, Scott M., and Solomon, Stanley C., Solar-terrestrial coupling: Solar soft X-rays and thermospheric nitric oxide. Geophysical Research Letters, **26**, 1251–1254, 1999.

[142] G. W. Prölss, U. von Zahn, and W. J. Raitt, Neutral atmospheric composition, plasma density, and electron temperature at F region heights. Journal of Geophysical Research, **80**, 3715–3718, 1975.

[143] Martin G. Mlynczak, Linda A. Hunt, B. Thomas Marshall, F. Javier Martin-Torres, Christopher J. Mertens, James M. Russell, Ellis E. Remsberg, Manuel López-Puertas, Richard Picard, Jeremy Winick, Peter Wintersteiner, R. Earl Thompson, and Larry L. Gordley, Observations of infrared radiative cooling in the thermosphere on daily to multiyear timescales from the TIMED/SABER instrument. Journal of Geophysical Research: Space Physics, **115**, n/a–n/a, 2010.

[144] Linda A. Hunt, Martin G. Mlynczak, B. Thomas Marshall, Christopher J. Mertens, Jeffrey C. Mast, R. Earl Thompson, Larry L. Gordley, and James M. Russell, Infrared radiation in the thermosphere at the onset of solar cycle 24. Geophysical Research Letters, **38**, n/a–n/a, 2011.

[145] Jiuhou Lei, Alan G. Burns, Jeffrey P. Thayer, Wenbin Wang, Martin G. Mlynczak, Linda A. Hunt, Xiankang Dou, and Eric Sutton, Overcooling in the upper thermosphere during the recovery phase of the 2003 October storms. Journal of Geophysical Research: Space Physics, **117**, n/a–n/a, 2012.

[146] G. Kockarts, Nitric oxide cooling in the terrestrial thermosphere. Geophysical Research Letters, **7**, 137–140, 1980.

[147] D. W. Rusch, J. C. Gerard, and C. G. Fesen, The diurnal variation of NO, N(^{2}D), and ions in the thermosphere: A comparison of satellite measurements to a model. Journal of Geophysical Research: Space Physics, **96**, 11331–11339, 1991.

[148] R. D. Sharma, Hoang Dothe, and F. von Esse, On the rotational distribution of the 5.3 μm “thermal” emission from nitric oxide in the nighttime terrestrial thermosphere. Journal of Geophysical Research: Space Physics, **101**, 17129–17135, 1996.

[149] C. S. Gardner, J. M. C. Plane, W. Pan, T. Vondra, B. J. Murray, and X. Chu, Seasonal variations of the Na and Fe layers at the south pole and their implications for the chemistry and general circulation of the polar mesosphere. J. Geophys. Res., **110**, D10302, 2005.

[150] James W. Duff and Sharma, Ramesh D., Quasiclassical trajectory study of NO vibrational relaxation by collisions with atomic oxygen. J. Chem. Soc., Faraday Trans., **93**, 2645–2649, 1997.

[151] R. D. Sharma, H. Dothe, and J. W. Duff, Model of the 5.3 μm radiance from NO during the sunlit terrestrial thermosphere. Journal of Geophysical Research: Space Physics, **103**, 14753–14768, 1998.

[152] E. S. Hwang, Karen J. Castle, and James A. Dodd, Vibrational relaxation of NO(v = 1) by oxygen atoms between 295 and 825 K. Journal of Geophysical Research: Space Physics, **108**, n/a–n/a, 2003.

[153] D. R. Marsh, S. C. Solomon, and A. E. Reynolds, Empirical model of nitric oxide in the lower thermosphere. Journal of Geophysical Research: Space Physics, **109**, n/a–n/a, 2004.

[154] J. L. Gardner, B. Funke, M. G. Mlynczak, M. López-Puertas, F. J. Martin-Torres, J. M. Russell, S. M. Miller, R. D. Sharma, and J. R. Winick, Comparison of nighttime nitric oxide 5.3 μm emissions in the thermosphere measured by MIPAS and SABER. Journal of Geophysical Research: Space Physics, **112**, n/a–n/a, 2007.

[155] Francis M. Vitt, Thomas E. Cravens, and Charles H. Jackman, A two-dimensional model of thermospheric nitric oxide sources and their contributions to the middle atmospheric chemical balance. Journal of Atmospheric and Solar-Terrestrial Physics, **62**, 653–667, 2000.

[156] F. M. Martin-Torres G. Crowley D. P. Kratz B. Funke G. Lu M. Lopez-Puertas J. M. Russell III J. Kozyra C. Mertens R. Sharma L. Gordley R. Picard J. Winick M. G. Mlynczak, M. G. and L. Paxton, Energy transport in the thermosphere during the solar storms of April 2002. J. Geophys. Res., **110**, A12S25, 2005.

[157] Martin G. Mlynczak, F. Javier Martin-Torres, and James M. Russell, Correction to "Energy transport in the thermosphere during the solar storms of april 2002". Journal of Geophysical Research: Space Physics, **112**, 2007.

[158] A. B. Christensen-T. L. Killeen J. M. Russell III J. Yee, E. R. Talaat and T. N. Woods, TIMED instruments. Johns Hopkins APL Technical Digest, **24**, 2003.

[159] L. L. Gordley J. J. Tansock Jr. R. W. Esplin J. M. Russell III, M. G. Mlynczak, Overview of the SABER experiment and preliminary calibration results. Proc. SPIE 3756, 1999.

[160] Christopher J. Mertens, Francis J. Schmidlin, Richard A. Goldberg, Ellis E. Remsberg, W. Dean Pesnell, James M. Russell, Martin G. Mlynczak, Manuel López-Puertas, Peter P. Wintersteiner, Richard H. Picard, Jeremy R. Winick, and Larry L. Gordley, SABER observations of mesospheric temperatures and comparisons with falling sphere measurements taken during the 2002 summer MaCWAVE campaign. Geophysical Research Letters, **31**, n/a–n/a, 2004.

[161] A. B. Christensen, L. J. Paxton, S. Avery, J. Craven, G. Crowley, D. C. Humm, H. Kil, R. R. Meier, C.-I. Meng, D. Morrison, B. S. Ogorzalek, P. Straus, D. J. Strickland, R. M. Swenson, R. L. Walterscheid, B. Wolven, and Y. Zhang, Initial observations with the Global Ultraviolet Imager (GUVI) in the NASA TIMED satellite mission. Journal of Geophysical Research: Space Physics, **108**, n/a–n/a, 2003.

[162] D. J. Strickland, R. R. Meier, R. L. Walterscheid, J. D. Craven, A. B. Christensen, L. J. Paxton, D. Morrison, and G. Crowley, Quiet-time seasonal behavior of the thermosphere seen in the far ultraviolet dayglow. Journal of Geophysical Research: Space Physics, **109**, n/a–n/a, 2004.

[163] R. E. Murphy, E. T. P. Lee, and A. M. Hart, Quenching of vibrationally excited nitric oxide by molecular oxygen and nitrogen. The Journal of Chemical Physics, **63**, 2919–2925, 1975.

[164] Toshihiro Ogawa, Excitation processes of infrared atmospheric emissions. Planetary and Space Science, **24**, 749–756, 1976.

[165] D. P. Drob J. M. Picone, A. E. Hedin and D. P. Aikin, NRLMSISE-00 empirical model of atmosphere: Stastical comparisons and scientific issues. J. Geophys. Res., **107**, 1468, 2002.

[166] Y. Zhang C. Mertens V. Truhlik P. Richards L. Mckinnell D. Bilitza, D. Altadill and B. Reinisch, International reference ionosphere 2012: a model of international collaboration. J. Space Weather Space Clim., **4**, 2014.

[167] Toshihiro Ogawa and Yutaka Kondo, Diurnal variability of thermospheric n and no. Planetary and Space Science, **25**, 735–742, 1977.

[168] D. C. Cartwright, M. J. Brunger, L. Campbell, B. Mojarrabi, and P. J. O. Teubner, Nitric oxide excited under auroral conditions: Excited state densities and band emissions. Journal of Geophysical Research: Space Physics, **105**, 20857–20867, 2000.

[169] Yu. I . Yermolaev, L . M. Zelenyi, V. D. Kuznetsov, I. M. Chertok, M. I. Panasyuk, I. N. Myagkova, I. A. Zhitnik, S. V. Kuzin, V. G. Eselevich, V. M. Bogod, I. V. Arkhangelskaja, A. I. Arkhangelsky, and Yu. D. Kotov, Magnetic storm of november, 2004: Solar, interplanetary, and magnetospheric disturbances. Journal of Atmospheric and Solar-Terrestrial Physics, **70**, 334–341, 2008.

[170] T. Yuan, Y. Zhang, X. Cai, C. Y. She, and L. J. Paxton, Impacts of CME induced geomagnetic storms on the midlatitude mesosphere and lower thermosphere observed by a sodium lidar and TIMED/GUVI. Geophys. Res. Lett., **42**, 7295–7302, 2015.

[171] N. H. Balan, Y. Alleyne, Y. Otsuka, V. Lekshmi, B. G. Fejer and I. McCrea, Relative effect of electric field and neutral wind on positive ionospheric storm. Earth Planet. Sci., **60**, 1–7, 2009.

[172] B. G. Fejer, J. W. Jensen, T. Kikuchi, M. A. Abdu, and J. L. Chau, Equatorial ionospheric electric fields during the November 2004 magnetic storm. Journal of Geophysical Research: Space Physics, **112**, n/a–n/a, 2007.

[173] T. J. Fuller-Rowell, M. V. Codrescu, R. J. Moffett and S. Quegan, Response of the thermosphere and ionosphere to geomagnetic storms. J. Geophys. Res., **99(A3)**, 3893–3914, 1994.

[174] R. G. Roble H. C. Carlson Jr. G. Crowley, B. A. Emery and D. J. Knipp, Thermospheric dynamics during september 18-19, 1984, 1. model simulations. J. Geophys. Res., **94**, 16,925–16,944, 1989.

[175] S. Gahlot V. Singh T. Bag, M.V. Sunil Krishna, Effect of severe geomagnetic storm conditions on atomic oxygen greenline dayglow emission in mesosphere. Adv. Space Res, **53**, 1255–1264, 2014.

[176] A. W. Stephan, R. R. Meier, and L. J. Paxton, Comparison of global ultraviolet imager limb and disk observations of column O/N_2 during a geomagnetic storm. Journal of Geophysical Research: Space Physics, **113**, n/a–n/a, 2008.

[177] Jiuhou Lei, Jeffrey P. Thayer, Alan G. Burns, Gang Lu, and Yue Deng, Wind and temperature effects on thermosphere mass density response to the November 2004 geomagnetic storm. Journal of Geophysical Research: Space Physics, **115**, n/a–n/a, 2010.

[178] N. Balan K. Igarashi A. J. Ridley D. J. Knipp A. Saito K. Shiokawa, Y. Ogawa and Yumoto, A large-scale travelling disturbance during the magnetic storm of 15 September 1999. Journal of Geophysical Research: Space Physics, **107**, 1088.

[179] T. J. Fuller-Rowell, A. D. Richmond, and N. Maruyama. *Global Modeling of Storm-Time Thermospheric Dynamics and Electrodynamics*, pages 187–200. American Geophysical Union (AGU), 2013.

[180] Stanley C. Solomon, Charles A. Barth, and Scott M. Bailey, Auroral production of nitric oxide measured by the SNOE satellite. Geophysical Research Letters, **26**, 1259–1262, 1999.

[181] Martin G. Mlynczak, F. Javier Martin-Torres, Christopher J. Mertens, B. Thomas Marshall, R. Earl Thompson, Janet U. Kozyra, Ellis E. Remsberg, Larry L. Gordley, James M. Russell, and Thomas Woods, Solar-terrestrial coupling evidenced by periodic behavior in geomagnetic indexes and the infrared energy budget of the thermosphere. Geophysical Research Letters, **35**, 2008.

[182] Susan Solomon, Paul J. Crutzen, and Raymond G. Roble, Photochemical coupling between the thermosphere and the lower atmosphere: 1. odd nitrogen from 50 to 120 km. Journal of Geophysical Research: Oceans, **87**, 7206–7220.

[183] C. A. Barth Siskind, D. E. and R. G. Roble, The response of thermospheric nitric oxide to an auroral storm: 1. low and middle latitudes. Journal of Geophysical Research: Space Physics, **94**, 16885–16898.

[184] D. R. Weimer, M. G. Mlynczak, L. A. Hunt, and W. Kent Tobiska, High correlations between temperature and nitric oxide in the thermosphere. Journal of Geophysical Research: Space Physics, **120**, 5998–6009, 2015.

[185] Charles A. Barth, W. Kent Tobiska, David E. Siskind, and David D. Cleary, Solar-terrestrial coupling: Low-latitude thermospheric nitric oxide. Geophysical Research Letters, **15**, 92–94, 1988.

[186] C. A. Barth, D. S. Evans, Siskind, D. E. and R. G. Roble, The response of thermospheric nitric oxide to an auroral storm: 1. low and middle latitudes. Journal of Geophysical Research: Space Physics, **94**, 16885–16898, 1989.

[187] A. L. Dobbin and A. D. Aylward, A three-dimensional modelling study of the processes leading to mid latitude nitric oxide increases in the lower thermosphere following periods of high geomagnetic activity. Advances in Space Research, **42**, 1576–1585, 2008.

[188] C. A. Barth, G. Lu, and R. G. Roble, Joule heating and nitric oxide in the thermosphere. Journal of Geophysical Research: Space Physics, **114**, 2009.

[189] A. L. Dobbin, A. D. Aylward, and M. J. Harris, Three-dimensional GCM modeling of nitric oxide in the lower thermosphere. Journal of Geophysical Research: Space Physics, **111**, 2006.

[190] A. L. Dobbin, E. M. Griffin, A. D. Aylward, and G. H. Millward, 3-D GCM modelling of thermospheric nitric oxide during the 2003 Halloween storm. Annales Geophysicae, **24**, 2403–2412, 2006.

[191] B. Funke, M. Lopez-Puertas, S. Gil-Lopez, T. von Clarmann, G. P. Stiller, H. Fischer, and S. Kellmann, Downward transport of upper atmospheric NOx into the polar stratosphere and lower mesosphere during the Antarctic 2003 and Arctic 2002/2003 winters. Journal of Geophysical Research: Atmospheres, **110**, 2005.

[192] C. E. Randall, V. L. Harvey, C. S. Singleton, S. M. Bailey, P. F. Bernath, M. Codrescu, H. Nakajima, and J. M. Russell, Energetic particle precipitation effects on the southern hemisphere stratosphere in 1992–2005. Journal of Geophysical Research: Atmospheres, **112**, 2007.

[193] S. D. Bouwer W. Kent Tobiska and B. R. Bowman, The development of new solar indices for use in thermospheric density modeling. J. Atmos. Sol-Terr. Phys., **70**, 803–819, 2008.

[194] H. G. Mayr and H. Volland, Theoretical model for the latitude dependence of the thermospheric annual and semiannual variations. Journal of Geophysical Research, **77**, 6774–6790, 1972.

[195] H. G. Mayr, I. Harris, and N. W. Spencer, Some properties of upper atmosphere dynamics. Reviews of Geophysics, **16**, 539–565.

[196] G. W. Prolss, Magnetic storm associated perturbations of the upper atmosphere: Recent results obtained by satellite-borne gas analyzers. Reviews of Geophysics, **18**, 183–202, 1980.

[197] D. Bermejo-Pantaleón, B. Funke, M. López-Puertas, M. García-Comas, G. P. Stiller, T. von Clarmann, A. Linden, U. Grabowski, M. Höpfner, M. Kiefer, N. Glatthor, S. Kellmann, and G. Lu, Global observations of thermospheric temperature and nitric oxide from MIPAS spectra at 5.3 μm. Journal of Geophysical Research: Space Physics, **116**, n/a–n/a, 2011.

[198] M. G. Mlynczak, Energetics of the mesosphere and lower thermosphere and the SABER experiment. Adv. Space Res., **20**, 1177–1183, 1997.

[199] Sierra Flynn, Delores J. Knipp, Tomoko Matsuo, Martin Mlynczak, and Linda Hunt, Understanding the global variability in thermospheric nitric oxide flux Using Empirical Orthogonal Functions (EOFs). Journal of Geophysical Research: Space Physics, **123**, 4150–4170, 2018.

[200] Gaurav Bharti, T. Bag, and M.V. Sunil Krishna, Effect of geomagnetic storm conditions on the equatorial ionization anomaly and equatorial temperature anomaly. Journal of Atmospheric and Solar-Terrestrial Physics, **168**, 8–20, 2018.

[201] G. Crowley B. A. Emery Burns A. G., T. L. Killeen and R. G. Robel, On the mechanisms responsible for high-latitude thermospheric composition variations during the recovery phase of a geomagnetic storm. Journal of Geophysical Research: Space Physics, **94**, 16961–16968, 1989.

[202] Solomon, Stanley C., Barth, Charles A., and Bailey, Scott M., Auroral production of nitric oxide measured by the SNOE satellite. Geophysical Research Letters, **26**, 1259–1262.

[203] Charles H. Jackman, Eric L. Fleming, Sushil Chandra, David B. Considine, and Joan E. Rosenfield, Past, present, and future modeled ozone trends with comparisons to observed trends. Journal of Geophysical Research: Atmospheres, **101**, 28753–28767, 1996.

[204] A. Seppälä, P. T. Verronen, E. Kyrölä, S. Hassinen, L. Backman, A. Hauchecorne, J. L. Bertaux, and D. Fussen, Solar proton events of October–November 2003: Ozone depletion in the northern hemisphere polar winter as seen by GOMOS/Envisat. Geophysical Research Letters, **31**, 2004.

[205] G. Rohen, C. von Savigny, M. Sinnhuber, E. J. Llewellyn, J. W. Kaiser, C. H. Jackman, M.-B. Kallenrode, J. Schröter, K.-U. Eichmann, H. Bovensmann, and J. P. Burrows, Ozone depletion during the solar proton events of October/November 2003 as seen by SCIAMACHY. Journal of Geophysical Research: Space Physics, **110**, 2005.

[206] Pekka T. Verronen, Annika Seppälä, Erkki Kyrölä, Johanna Tamminen, Herbert M. Pickett, and Esa Turunen, Production of odd hydrogen in the mesosphere during the January 2005 solar proton event. Geophysical Research Letters, **33**, 2006.

[207] Charles H. Jackman, Richard D. McPeters, Gordon J. Labow, Eric L. Fleming, Cid J. Praderas, and James M. Russell, Northern hemisphere atmospheric effects due to the July 2000 solar proton event. Geophysical Research Letters, **28**, 2883–2886, 2001.

[208] Charles H. Jackman, Matthew T. DeLand, Gordon J. Labow, Eric L. Fleming, Debra K. Weisenstein, Malcolm K.W. Ko, Miriam Sinnhuber, John Anderson, and James M. Russell, The influence of the several very large solar proton events in years 2000–2003 on the neutral middle atmosphere. Advances in Space Research, **35**, 445–450, 2005.

[209] Charles H. Jackman, Raymond G. Roble, and Eric L. Fleming, Mesospheric dynamical changes induced by the solar proton events in October–November 2003. Geophysical Research Letters, **34**, 2007.

[210] Charles H. Jackman, Matthew T. DeLand, Gordon J. Labow, Eric L. Fleming, Debra K. Weisenstein, Malcolm K. W. Ko, Miriam Sinnhuber, and James M. Russell, Neutral atmospheric influences of the solar proton events in October–November 2003. Journal of Geophysical Research: Space Physics, **110**, 2005.

[211] O. P. Verkhoglyadova, S. Wang, M. G. Mlynczak, L. A. Hunt, and G. P. Zank, Effects of two large solar energetic particle events on middle atmosphere nighttime odd hydrogen and ozone content: Aura/MLS and TIMED/SABER measurements. Journal of Geophysical Research: Space Physics, **120**, 12–29, 2015.

[212] J. M. C. Plane, C. S. Gardner, J. Yu, C. Y. She, R. R. Garcia, and H. C. Pumphrey, Mesospheric Na layer at 40°N: Modeling and observations. J. Geophys. Res., **104**, 3773–3788, 1999.

[213] D. L. Huestis A. Saiz-Lopez B. J. Murray D. A. ÓSullivan J. M. C. Plane C. Allende Prieto F. J. Martin-Torres T. G. Slanger, P. C. Cosby and P. Jenniskens, Variability of the mesospheric nightglow sodium d2/d1 ratio. J. Geophys. Res., **110**, 2005.

[214] E. C. M. Dawkins, J. M. C. Plane, M. P. Chipperfield, W. Feng, D. R. Marsh, J. Höffner, and D. Janches, Solar cycle response and long-term trends in the mesospheric metal layers. Journal of Geophysical Research: Space Physics, **121**, 7153–7165, 2016.

[215] J. Gumbel J. Stegman Z. Y. Fan, J. M. C. Plane and E. J. Llewellyn, Satellite measurement of global mesospheric sodium layer. Atmos.Chem.Phys., **7**, 4107–4115, 2007.

[216] C. J. Rodger M. A. Clilverd & A. Seppälä M. E. Andersson, P. T. Verronen, Missing driver in the Sun–Earth connection from energetic electron precipitation impacts mesospheric ozone. Nature Communications, **5**, 5197, 2014.

[217] D. A. Degenstein, N. D. Lloyd, A. E. Bourassa, R. L. Gattinger, and E. J. Llewellyn, Observations of mesospheric ozone depletion during the October 28, 2003 solar proton event by OSIRIS. Geophysical Research Letters, **32**, 2005.

[218] A. A. Krivolutsky, A. V. Klyuchnikova, G. R. Zakharov, T. Yu. Vyushkova, and A. A. Kuminov, Dynamical response of the middle atmosphere to solar proton event of July 2000: Three-dimensional model simulations. Advances in Space Research, **37**, 1602–1613, 2006.

[219] F. Friederich, T. von Clarmann, B. Funke, H. Nieder, J. Orphal, M. Sinnhuber, G. P. Stiller, and J. M. Wissing, Lifetime and production rate of NOx in the upper stratosphere and lower mesosphere in the polar spring/summer after the solar proton event in October-November 2003. Atmos. Chem. Phys., **13**, 2531–2539, 2013.

[220] C. J. Heinselman, J. P. Thayer, and B. J. Watkins, A high-latitude observation of sporadic sodium and sporadic E-layer formation. Geophys. Res. Lett., **25**, 3059–3062, 1998.

[221] T. T. Tsuda, S. Nozawa, T. D. Kawahara, T. Kawabata, N. Saito, S. Wada, Y. Ogawa, S. Oyama, C. M. Hall, M. Tsutsumi, M. K. Ejiri, S. Suzuki, T. Takahashi, and T. Nakamura, Decrease in sodium density observed during auroral particle precipitation over Tromsø, Norway. Geophysical Research Letters, **40**, 4486–4490.

[222] H. Takahashi S. M. L. Melo B. R. Clemesha, D. M. Simonich and J. M. C. Plane, Experimental evidence for photochemical control of the atmospheric sodium layer. J. Geophys. Res., **100(D9)**, 18,909–18,916, 1995.

[223] C. Kruschwitz M. C. Kelly R. G. Roble J. H. Hecht, S. Collins and R. L. Walterscheid, The excitation of the Na airglow from Coqui Dos rocket and ground based observations. Geophys. Res. Lett., **27**, 453–456, 2000.

[224] Gomez Martin, J. C., Garraway, S. A., and J. M. C. Plane, Reaction kinetics of meteoric sodium reservoirs in the upper atmosphere. The Journal of Physical Chemistry A, **120**, 1330–1346, 2016.

[225] C. Y. She, Jim Sherman, Tao Yuan, B. P. Williams, Kam Arnold, T. D. Kawahara, Tao Li, Li Fang Xu, J. D. Vance, P. Acott, and David A. Krueger, The first 80-hour continuous lidar campaign for simultaneous observation of mesopause region temperature and wind,. Geophysical Research Letters, **30**, 2003.

[226] R. L. Collins T. Yuan B. P. Williams T. D. Kawahara J. D. Vance P. Acott C. Y. She, T. Li and D. A. Krueger, Tidal perturbations and variability in the mesopause region over Fort Collins, CO (41°N, 105°W): Continuous multi-day temperature and wind lidar observations. Geophys. Res. Lett., **31**, L24111, 2004.

[227] C. Y. She, Songsheng Chen, B. P. Williams, Zhilin Hu, David A. Krueger, and M. E. Hagan, Tides in the mesopause region over Fort Collins, Colorado (41°N, 105°W) based on lidar temperature observations covering full diurnal cycles,. Journal of Geophysical Research: Atmospheres, **107**, ACL 4–1–ACL 4–12, 2002.

[228] Craig J. Heinselman, Auroral effects on the gas phase chemistry of meteoric sodium. Journal of Geophysical Research: Atmospheres, **105**, 12181–12192.

[229] L. H. Weeks, R. S. Cuikay, and J. R. Corbin, Ozone measurements in the mesosphere during the solar proton event of 2 November 1969. Journal of the Atmospheric Sciences, **29**, 1138–1142, 1972.

[230] R. D. McPeters, C. H. Jackman, and E. G. Stassinopoulos, Observations of ozone depletion associated with solar proton events. Journal of Geophysical Research: Oceans, **86**, 12071–12081.

[231] G. C. Reid, S. Solomon, and R. R. Garcia, Response of the middle atmosphere to the solar proton events of August–December, 1989. Geophysical Research Letters, **18**, 1019–1022, 1991.

[232] Zicheng Zou, Xianghui Xue, Chenglong Shen, Wen Yi, Jianfei Wu, Tingdi Chen, and Xiankang Dou, Response of mesospheric HO_2 and $O_3$3 to large solar proton events. Journal of Geophysical Research: Space Physics, **123**, 5738–5746.

[233] B. G. Fejer, Low latitude electrodynamic plasma drift: A review. J. Atoms Sol-Terr. Phys., **53**, 677–693, 1991.

[234] N. Balan and K. N. Iyer, Equatorial anomaly in ionospheric electron content and its relation to dynamo currents. Journal of Geophysical Research: Space Physics, **88**, 10259–10262, 1983.

[235] B. G. Fejer, D. Hui, J. L. Chau, and E. Kudeki, Altitudinal dependence of evening equatorial F region vertical plasma drifts. Journal of Geophysical Research: Space Physics, **119**, 5877–5890, 2014.

[236] B. G. Fejer, J. R. Souza, A. S. Santos, and A. E. Costa Pereira, Climatology of F region zonal plasma drifts over Jicamarca. Journal of Geophysical Research: Space Physics, **110**, n/a–n/a, 2005.

[237] Debrup Hui and Bela G. Fejer, Daytime plasma drifts in the equatorial lower ionosphere. Journal of Geophysical Research: Space Physics, **120**, 9738–9747, 2015.

[238] B. G. Fejer, F region plasma drifts over arecibo: Solar cycle, seasonal, and magnetic activity effects. Journal of Geophysical Research: Space Physics, **98**, 13645–13652, 1993.

[239] B. G. Fejer and L. Scherliess, Time dependent response of equatorial ionospheric electric fields to magnetospheric disturbances. Geophys. Res. Lett., **22**, 851–854, 1995.

[240] G. W. Prolss, Common Origin of Positive Ionospheric Storms at Middle Latitudes and the Geomagnetic Activity Effect at Low Latitudes. J. Geophys. Res., **98**, 5981–5991, 1993.

[241] T. J. Fuller-Rowell, M. V. Codrescu, H. Rishbeth, R. J. Moffett, and S. Quegan, On the seasonal response of the thermosphere and ionosphere to geomagnetic storms. Journal of Geophysical Research: Space Physics, **101**, 2343–2353, 1996.

[242] M. A. Abdu, J. H. A. Sobral, E. R. de Paula, and I. S. Batista, Magnetospheric disturbance effects on the Equatorial Ionization Anomaly (EIA) : an overview. Journal of Atmospheric and Terrestrial Physics, **53**, 757–771, 1991.

[243] R. Raghavarao, L. E. Wharton, N. W. Spencer, H. G. Mayr, and L. H. Brace, An equatorial temperature and wind anomaly (ETWA). Geophysical Research Letters, **18**, 1193–1196, 1991.

[244] R. Raghavarao, W. R. Hoegy, N. W. Spencer, and L. E. Wharton, Neutral temperature anomaly in the equatorial thermosphere-a source of vertical winds. Geophysical Research Letters, **20**, 1023–1026, 1993.

[245] N. Balan and G. J. Bailey, Equatorial plasma fountain and its effects: Possibility of an additional layer. Journal of Geophysical Research: Space Physics, **100**, 21421–21432, 1995.

[246] M. A. Abdu, Major phenomena of the equatorial ionosphere-thermosphere system under disturbed conditions. Journal of Atmospheric and Solar-Terrestrial Physics, **59**, 1505–1519, 1997.

[247] C. R. Philbrick and J. P. McIsaac, Measurements of atmospheric composition near 400 km. Space Res., **12**, 743–750, 1972.

[248] Y. Miyoshi, H. Fujiwara, H. Jin, H. Shinagawa, H. Liu, and K. Terada, Model study on the formation of the equatorial mass density anomaly in the thermosphere. Journal of Geophysical Research: Space Physics, **116**, n/a–n/a, 2011.

[249] J. Lei, W. Wang, J. P. Thayer, X. Luan, X. Dou, A. G. Burns, and S. C. Solomon, Simulations of the equatorial thermosphere anomaly: geomagnetic activity modulation. J. Geophys. Res., **119**, 682–6832, 2014.

[250] M.V. Sunil krishna and V. Singh, Testing of Solar2000 EUV flux model between 900–1350 A° using greenline dayglow emission. Ind. J. Radio. Space, **38**, 37–41, 2009a.

[251] P. Thirupathaiah,, M. V. Sunil Krishna, and Vir Singh, Effect of solar activity on the latitudinal variation of peak emission rate of 557.7nm dayglow emission under equinox conditions. Journal of Atmospheric and Solar-Terrestrial Physics, **77**, 209–218, 2012.

[252] Maneesha Dharwan, P. Thirupathaiah, and Vir Singh, A study of 732.0 nm dayglow emission at the equator under varying atomic oxygen density conditions for equinox and solstice cases. Earth and Space Science, **1**, 18–31, 2014.

[253] S. Chapman, Some phenomenon in the upper atmosphere. Proc. R. Soc. London., A132, 353(1931).

[254] C.A. Barth, Threebody reactions. Ann. Phys., **5**, 329, 1964.

[255] F. L. Walls and G. H. Dunn, Measurement of total cross sections for electron recombination with NO^+ and O_2^+ using ion storage techniques. J. Geophys. Res., **79**, 1911–1915, 1974.

[256] D. D. Cleary S. M. Hill, S. C. Solomon and A. L. Broadfoot, Temperature dependence of the reaction $N_2(A^3\Sigma_u^+)$+O in the terrestrial atmosphere. J. Geophys. Res., **105**, 10615–10629, 2000.

[257] M. Melo, H. Takahashi, B. Clemesha, P. Natosta and D. Simonich, Atomic oxygen concentrations from rocket airglow observations in the equatorial region. J. Atoms Sol-Terr. Phys., **58**, 1935–1942, 1996.

[258] B. Clemesha D. Gobbi, H. Takahashi and P. Batista, Equatorial atomic oxygen profiles derived from rocket observations of OI 557.7 nm airglow emission. Planet. Space Sci., **40**, 775–781, 1992.

[259] O. Sinanoglu C. Nicolaides and P. Westhouse, Theory of atomic structure including electron correlation. IV. method for forbidden transition probabilities with results for [OI], [OII], [NI], [NII] and [CI]. Phys. Rev. A., **4**, 1400–1410, 1971.

[260] A. W. Stephan, R. R. Meier, K. F. Dymond, S. A. Budzien, and R. P. McCoy, Quenching rate coefficients for $O^+(^2P)$ derived from middle ultraviolet airglow. Journal of Geophysical Research: Space Physics, **108**, n/a–n/a, 2003.

[261] D. W. Rusch, D. G. Torr, P. B. Hays, and J. C. G. Walker, The OII (7319-7330 A°) dayglow. J. Geophys. Res., **82**, 719–722, 1977.

[262] T. Chang, D. G. Torr, P. G. Richards, and S. C. Solomon, Reevaluation of the $O^+(^2P)$ reaction rate coefficients derived from Atmosphere Explorer C observations. Journal of Geophysical Research: Space Physics, **98**, 15589–15597, 1993.

[263] Ronald J. W. Henry, P. G. Burke, and A. L. Sinfailam, Scattering of electrons by C, N, O, n^+, o^+, and o^{++}. Phys. Rev., **178**, 218–225, 1969.

[264] N. Balan, M. Yamamoto, J. Y. Liu, Y. Otsuka, H. Liu and H. L$\mathring{u}$hr, New aspects of thermospheric and ionospheric torms revealed by CHAMP. J. Geophys. Res., **116**, A07305, 2011.